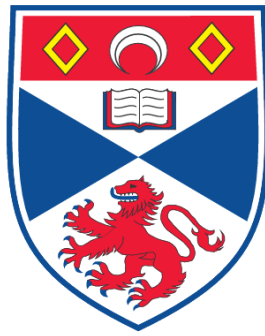


**WARPING, DUST SETTLING AND DYNAMICS OF  
PROTOPLANETARY DISKS**

**Mark George O'Sullivan**

**A Thesis Submitted for the Degree of PhD  
at the  
University of St. Andrews**



**2008**

**Full metadata for this item is available in the St Andrews  
Digital Research Repository  
at:**

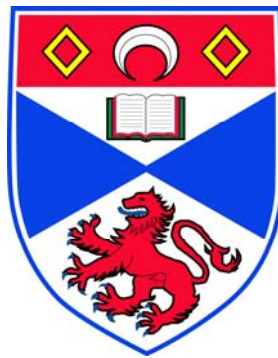
**<https://research-repository.st-andrews.ac.uk/>**

**Please use this identifier to cite or link to this item:**

**<http://hdl.handle.net/10023/782>**

**This item is protected by original copyright**

# **Warping, Dust Settling and Dynamics of Protoplanetary Disks**



**Thesis presented for the degree of  
Doctor of Philosophy  
to the University of St Andrews**

**by  
Mark George O'Sullivan, MSci**

The J. F. Allen Physics Research Laboratories  
School of Physics and Astronomy  
University of St. Andrews  
North Haugh  
St. Andrews  
Scotland KY16 9SS

November, 2008

## **Declarations**

I, Mark George O'Sullivan, hereby certify that this thesis, which is approximately thirty four thousand words in length, has been written by me, that it is a record of the work carried out by me and that it has not been submitted in any previous application for a higher degree.

Signature of candidate:

Date:

I was admitted as a research student and as a candidate for the degree of Doctor of Philosophy in April, 2003; the higher study for which this is a record was carried out at the University of St Andrews between 2003 and 2006.

Signature of candidate:

Date:

I hereby certify that the candidate has fulfilled the conditions of the Resolution and Regulations appropriate for the degree of Doctor of Philosophy in the University of St Andrews and that the candidate is qualified to submit this thesis in application for that degree.

Signature of supervisor:

Date:

In submitting this thesis to the University of St Andrews I understand that I am giving permission for it to be made available for use in accordance with the regulations of the University Library for the time being in force, subject to any copyright vested in the work not being affected thereby. I also understand that the title and abstract will be published, and that a copy of the work may be made and supplied to any bona fide library or research worker, that my thesis will be electronically accessible for personal or research use, and that the library has the right to migrate my thesis into new electronic forms as required to ensure continued access to the thesis. I have obtained any third-party copyright permissions that may be required in order to allow such access and migration.

Signature of candidate:

Date:

*for*  
*Mum, Dad*  
*& Sean*

## **Acknowledgements**

I would like to take this opportunity to thank the people who have made the work contained in this thesis possible, helped and supported me through the last three years and made that time as rewarding and fun as it has been.

Firstly I'd like to thank my supervisor, Kenny Wood. Without his support, encouragement, enthusiasm and endless stream of ideas there wouldn't be a thesis here at all. I should also thank my office mate Christina (and for a few months, bump), who was always willing and able to help.

I'd also like to thank the many friends who have provided advice (some good, some not so good) and support and who have filled the last 3 years with innumerable good memories. A few of the most notable are Matt, Al, Chrispy, Mikey, Goose, Steve, Beccy, Nick, Lara, Laura, Chris, Gump, Tommy, Chief and the Monkeys.

Finally I would like to thank my parents, Paddy and Cherry, for supporting me, mentally and financially, and encouraging me at every stage of my academic life. Without their help I wouldn't have got to where I am today.

Thank you.

## Abstract

The research presented in this thesis investigates several aspects of the evolutionary processes of T Tauri stars and their accompanying circumstellar disks. The versatile Monte Carlo radiation transfer technique, with several modifications and extensions, is used throughout to study the structure and constitution of both the circumstellar disk at large and the changeable and dynamic inner disk regions.

The photopolarimetric variability of AA Tau in the Taurus star forming region is modelled in a fully 3D manner. I find that a magnetospherically induced warp in the accretion disk at roughly the stellar co-rotation radius occults the star and reproduces both the observed period and duration and the required brightness and polarisation variations. The model SEDs allow estimates of the disk mass, radial extent and large-scale density structure. Using a modified SPH code we find the interaction of a 5.2kG stellar magnetic field inclined at  $30^\circ$  to the rotation axis with the disk, is capable of generating a warp of the size and shape needed to reproduce the observed variations.

Modified Monte Carlo models capable of incorporating any number of dust particle grain sizes distributed throughout the disk in vertical and radial distributions, in a fully 3D manner are presented. This versatile tool allows the investigation of evolutionary processes such as dust settling and grain growth predicted to occur in T Tauri sources as they age. A Mie Scattering code was also adapted and incorporated into the models allowing us to determine optical properties for dust grains and distributions of any size.

I present model SEDs fitting the latest publicly available IR data for a number of T Tauri sources and reproduce the observational effects of dust grain growth and settling with a high degree of success. The fits are by no means unique and the structural parameters required to produce them are quite uncertain but it is possible to determine useful information on the larger scale structure and bulk constituents of these disks.

A fully 3D non-LTE radiative transfer code using CO line emissions as a tracer of the disk dynamics and able to simulate any disk structure or geometry, either analytical or imported from a hydrodynamic simulation, is presented. Signatures attributed to the disk dynamics and spiral density structure derived from hydrodynamic simulations of massive disks are investigated and resolved. Line profiles and contour maps of the velocity of the emitting material are generated and compared with observations.

## Contents

Declaration	ii
Acknowledgements	iv
Abstract	v
<b>1. Introduction &amp; Background</b>	<b>1</b>
1.1. Overview	1
1.2. Star Formation & YSOs	1
1.3. T Tauri Stars	8
1.3.1. Classical T Tauri Stars	10
1.3.2. Weak Line T Tauri Stars	12
1.3.3. Early T Tauri Stars	13
1.3.4. Jets & Outflows	13
1.4. Radiation Transfer	15
1.5. Monte Carlo Method	20
1.6. Dust Settling & Grain Growth	25
1.6.1. Review of Recent Studies	27
1.7. Outline of Thesis	38
<b>2. Modelling the photopolarimetric variability of AA Tau</b>	<b>40</b>
2.1. Introduction	40
2.2. AA Tau's Photopolarimetry	41
2.3. Radiation Transfer Models	43
2.3.1. Disk Structure from SED Modelling	43
2.3.2. Photopolarimetry Models & Analytical Disk Warping	45
2.3.3. Time Sequence Scattered Light Images	50
2.4. Hydrodynamic Simulation	53
2.5. Conclusion	56
<b>3. Dust settling &amp; grain growth</b>	<b>58</b>
3.1. Introduction	58
3.2. Fully 3D, Multiple Dust Species Code development	58
3.2.1. Dust Grains	60

3.3. Exploring the Effects of Multiple Dust Species	61
3.4. Investigation of dust settling & grain growth in a sample of CTTS	66
3.4.1. AA Tau	69
3.4.2. CoKu Tau/4	72
3.4.3. DM Tau	74
3.4.4. GM Aurigae	77
3.4.5. GO Tau	80
3.4.6. LkCa15	82
3.4.7. TW Hydra	84
3.5. Conclusion	87
 <b>4. Non – LTE molecular line transitions</b>	 <b>91</b>
4.1. Introduction	91
4.2. The Bernes Model and its Expansion to 3D	91
4.3. Comparison with Bernes Non – LTE Radiative Transfer Program	95
4.3.1. 1D Comparison	95
4.3.2. 3D Comparison	97
4.4. Conclusion	100
 <b>5. Application of non – LTE line transition code to circumstellar disks</b>	 <b>101</b>
5.1. Introduction	101
5.2. CO Emission from LkCa15	101
5.3. Investigating dynamical models of a compact massive disk	106
5.4. Conclusion & future applications of the code	113
 <b>6. Future Investigations</b>	 <b>115</b>
 <b>Bibliography</b>	 <b>117</b>



## **1. Introduction & Background**

### **1.1 Overview**

In recent decades high spectral and spatial resolution imaging and spectroscopy have begun to shed light on the processes and causes of stellar and planetary formation. Much of this formation takes place deeply embedded in dusty molecular clouds through which light in the visible part of the spectrum is heavily absorbed and has required the development of detectors and space missions in order to observe in the infrared portion of the spectrum. This region of the spectrum is relatively unaffected by the obscuring gas and dust of molecular clouds and the spiral arms of our galaxy and is enabling astronomers to observe, in detail, processes and objects that were previously hidden.

Throughout this chapter I will review the processes and conditions that lead to the formation of Young Stellar Objects (YSOs) from molecular gas clouds, the different classes of object that are formed in this process and discuss in more detail the T Tauri class which is of particular relevance for investigating the early stages of solar-type systems.

Being able to observe and detect these objects is all well and good but without the ability to model the processes and mechanisms that might be responsible for producing the observational signatures very little can truly be understood or determined about their significance and meaning. Throughout this thesis I have used the Monte Carlo technique to construct Radiation Transfer models of different aspects of these sources and I will briefly review the basic principles of Monte Carlo Radiation Transfer simulations. The chapter concludes with an outline of the motivation, aims and overall themes of the research I have carried out in this thesis.

### **1.2 Star Formation & YSOs**

As the research and discussions throughout this thesis are primarily concerned with the T Tauri, protoplanetary disk system stage in the star formation process it is appropriate to review what is known of the conditions, environment and processes that form stars and discuss how this leads to the development of this stage in the evolutionary development of a star.

Stars form in regions where gas has become dense enough for its own self-gravity to overcome the galactic tidal forces, for example in spiral arms. Here there are substantial amounts of molecular material from which stars can form in structures known as giant

molecular clouds (GMCs). GMCs are formed by the passing pressure wave of the spiral arm and have sizes up to 100 parsecs and masses of up to  $10^6 M_{\odot}$  (Larson 2003). As these clouds have lifetimes governed by the transition of the spiral arm they exist for between  $10^7$  yr (e.g. Bash & Peters 1976) and  $10^8$  yr (Lada & Kyfalidis 1999) before being dispersed by intense winds from embedded O and B stars (Stahler & Palla 2005, SP05 from here). Very few GMCs are known that are not forming stars and the most massive and dense clouds all contain newly formed stars indicating that there is very little time between the formation of these clouds and the onset of star formation (Larson 2003). In the Taurus clouds, for example, the majority of stars have formed within the last few million years (Hartmann et al. 2001; Palla & Stahler 2002 and Hartmann 2003).

As a rough estimate we can assume that the cloud is a homogenous sphere and if it was to collapse under its own self gravity with no internal pressure it would collapse to a point on the free-fall timescale,

$$t_{ff} = \left( \frac{3\pi}{32G\rho} \right)^{-1/2}$$

where  $G$  is the gravitational constant and  $\rho$  is the cloud density. A collapse of this nature would occur in around  $10^6$  yr and produce much higher star formation rates than those observed so there must be some mechanism that provides support (SP05 & Ward-Thompson et al. 2007). In the early stages of large scale collapse in the cloud as a whole turbulence and magnetic fields may inhibit the free-fall collapse but these effects become less important in the collapse of higher density, pre-stellar cloud cores. Here the turbulence is subsonic and magnetic fields decouple from the gas by ambipolar diffusion and so thermal pressure is the most important force mechanism for resisting gravitational collapse (Larson 2003).

GMCs do not have smooth uniform density distributions however, and due to their constant motion (their own rotation and orbital movement round the galaxy) they form dense clumps throughout the cloud. These clumps have masses  $10^3 - 10^4 M_{\odot}$  and radii of a few parsecs. The gravitational attraction of the more dense material in these clumps produces sub-regions within the larger cloud. The sub-regions are known as cloud cores and have masses of around  $1 M_{\odot}$ , radii of around  $10^1$  pc and are embedded in massive dusty envelopes of several hundred  $M_{\odot}$  (Larson 2003). The collapse progresses in free-fall for approx.  $10^5$  yrs until the optical depth is  $>1$ , at which point the core is opaque to its own radiation and the thermal pressure halts the collapse. At this stage they are

called protostars, see Figure 1.1, and can be identified by their characteristic infrared Spectral Energy Distribution (SED) (Adams et al. 1987). The protostar continues to accrete material from the surrounding cloud, increasing the gravitational force until it overcomes the thermal pressure and the protostar collapses on the thermal or Kelvin-Helmholtz timescale,

$$t_{KH} = \frac{GM^2}{RL}$$

where  $G$  is the gravitational constant and  $M$ ,  $R$  and  $L$  are the mass, radius and luminosity respectively of the object. The luminosity of the object is the rate at which the thermal energy generated by the increasing pressure of the collapsing core is radiated away.

$$L = 4\pi R^2 \sigma T^4$$

Where  $R$  is the radius,  $\sigma$  is the Stephan-Boltzmann constant and  $T$  the temperature. This is related the surface area of the object, which if we were to think of as a series of spherical shells, increases as we move outwards from the centre. Therefore the local rate of energy loss is zero at the centre and increases monotonically outward and so the surface radiation is a net drain on the energy of the system and allows the constant contraction to progress.

When the central region of the protostar reaches a temperature of around 2000K  $H_2$  dissociates and this absorbs some of the thermal energy and removes pressure support allowing the protostar to slip back into free-fall contraction until pressure increases and returns the protostar to slower thermal contraction. The central protostar, now consisting of dissociated hydrogen, continues to contract until temperatures and densities are in excess of  $10^5$ K and  $10^{-2}$ g cm<sup>-3</sup> (Zelik, Gregory & Smith 1997) and the circumstellar material has been depleted, with disk lifetimes thought to be in the region of  $10^6$  yrs (Lada et al. 2002).

The material in the surrounding cloud that is falling in towards the protostar must conserve its angular momentum from its rotation as part of the cloud as a whole. As the cloud collapses the particles move closer to the axis of rotation and the cloud must rotate faster. At some point the centripetal acceleration,  $v^2/r$ , balances the gravitational force and the collapse stops. As it's the distance a particle is from the axis of rotation and not the centre of the cloud that determines the angular momentum a particle near the rotation axis can fall a long way toward the centre before its rotational velocity is

large enough to stop it. Those parts of the cloud originally near the rotation axis will collapse more than those near the equator and so the cloud flattens into a disk (Myers et al. 1987).

The system then comprises a central protostar with a massive envelope surrounding and rotating with it (e.g. Lynden-Bell & Pringle 1974, SP05, White et al. 2007). The accreting protostar's mass continues to increase and once it reaches the temperatures and densities in its interior where hydrogen fusion is sustainable ( $T \sim 10^7 \text{K}$ ) and depletes its circumstellar disk the protostar becomes a main sequence star. Figure 1.1 shows a series of diagrams marking the different stages of evolution undergone by the protostar on its way to becoming a main sequence star, possibly with a solar system like our own.

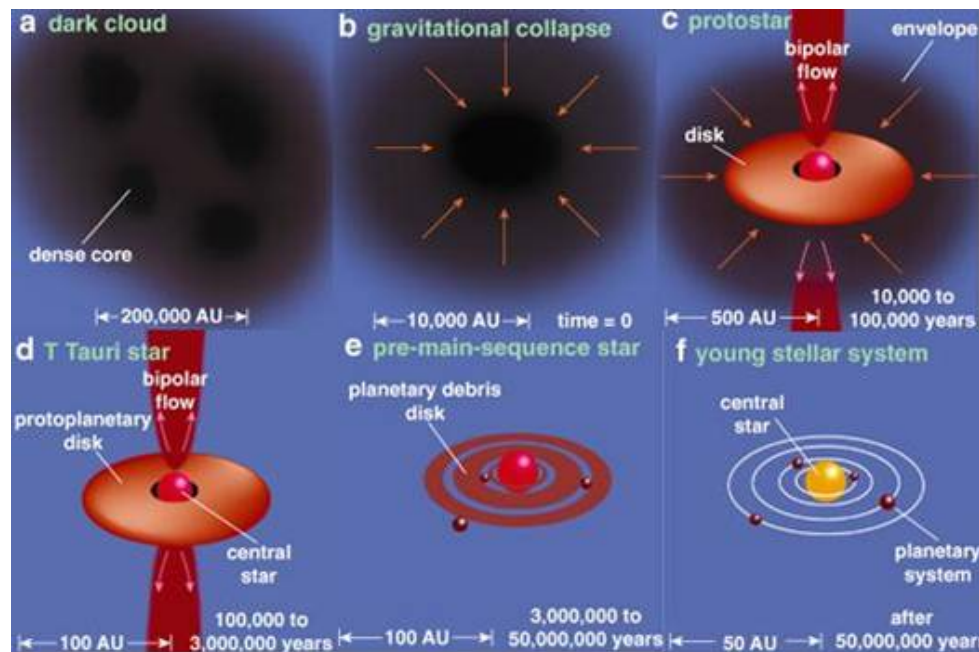


**Figure 1.1** Series of diagrams following the stages of evolution a forming star passes through before reaching a mature, planetary system stage like our own solar system. Image taken from Greene (2001).

An extremely important and useful tool in understanding and visualising a stars evolution from heavily embedded protostar, through its life on the main sequence as a hydrogen burning star, to the later stages of its life as a giant and eventually its end state (dependant on its mass) is the Hertzsprung-Russell (H-R) diagram. First developed in the early years of the twentieth century it is a plot of luminosity versus surface temperature but can also show absolute magnitude versus colour index (often called the colour magnitude diagram). Figure 1.2 is an example of a colour magnitude diagram

and plots stars from the Hipparcos and Gliese catalogues and shows the different stages of a stars evolution from the main sequence to its end state.

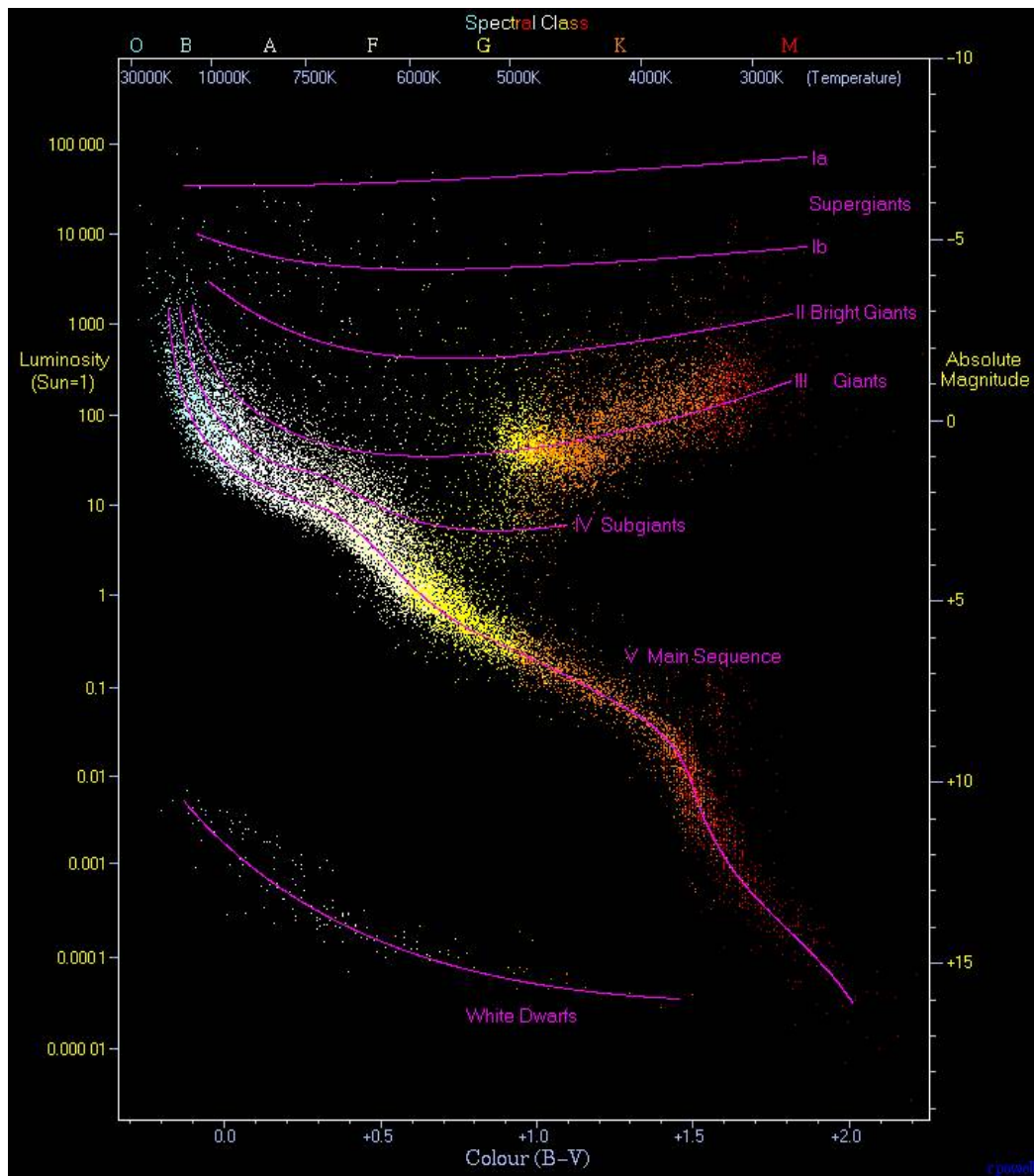


**Figure 1.2** Colour magnitude diagram plotting 22000 stars from the Hipparcos catalogue and 1000 from the Gliese catalogue of nearby stars. Stars tend to fall only into certain regions on the diagram. The most predominant is the diagonal, going from the upper-left (hot and bright) to the lower-right (cooler and less bright), called the main sequence. The lower-left is where white dwarfs (the end state of stars less massive than  $\sim 7M_{\odot}$ ) are found, and above the main sequence are the subgiants, giants and supergiants. The Sun is found on the main sequence at luminosity 1 (absolute magnitude 4.8) and temperature 5780K (spectral type G2). Image taken from <http://www.atlasoftheuniverse.com>

Several classes of YSO represent the first, post-infall, stage of stellar evolution. These are separated, primarily, by the shapes of their optical-infrared spectral energy

distributions and these will be covered later in this section. There are also several types of YSO and these are separated by their mass. T Tauri stars have masses of  $< 2M_{\odot}$ , Herbig Ae stars  $2M_{\odot} - 5M_{\odot}$  and Herbig Be stars  $5M_{\odot} - 10M_{\odot}$ . I will be concentrating on T Tauri stars throughout the thesis but many of the processes they undergo are thought to be similar to those of the Herbig stars as they evolve to the main sequence (see Mannings & Sargent 1997; 2000 for discussion of Herbig systems). It is as one of these types of YSO that a protostar first appears on the H-R diagram and between this stage and the ignition of fusion reactions the protostar is often called a pre-main sequence (PMS) star. The evolutionary track that protostars take on their way to the main sequence, depend on their masses and are often called Hayashi tracks.

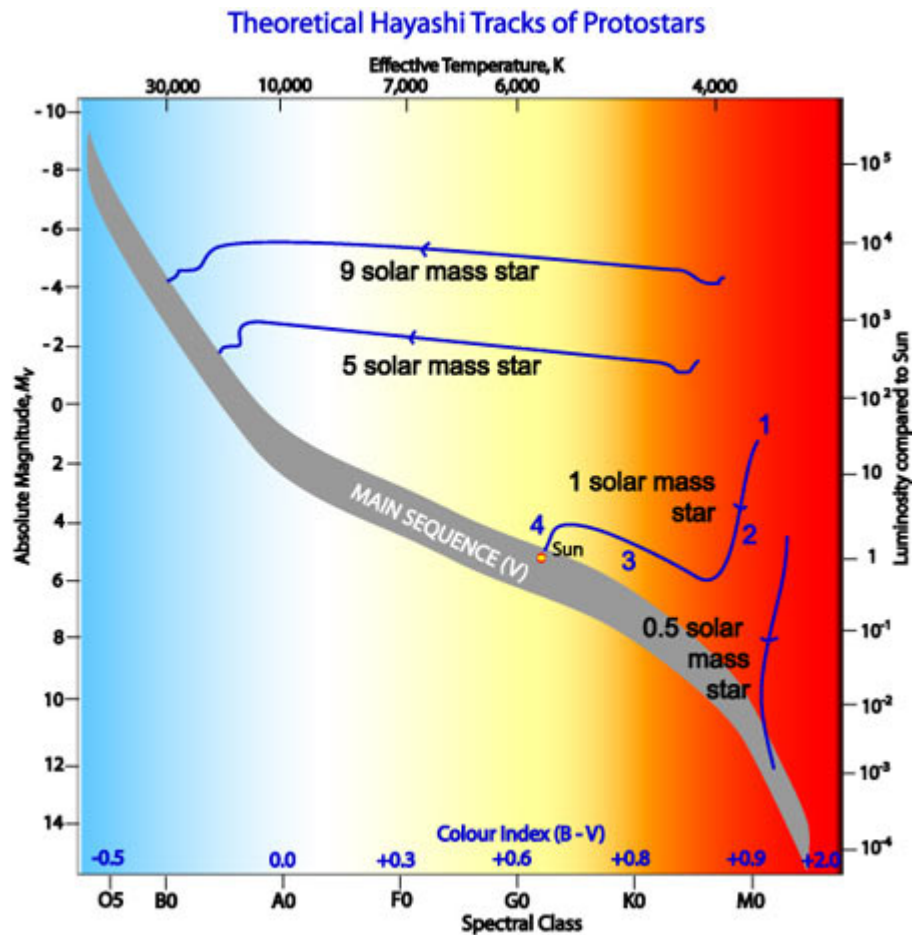


**Figure 1.3** shows the predicted evolutionary paths on the H-R diagram for 9, 5, 1 and 0.5 solar mass stars during their protostar stages. The four stages labelled for a  $1M_{\odot}$  star such as our Sun are explained in the text. Image taken from Australia Telescope educational material.

Protostars first appear on the right hand side of the H-R diagram, above the main sequence. When the contracting cores become protostars they emit radiation at the

cooler IR end of the spectrum and due to their large sizes (Radii of several  $R_{\odot}$ , SP05) they are more luminous than main sequence stars of similar temperatures. Figure 1.3 shows evolutionary tracks for protostars with masses of 0.5, 1, 5 and  $9M_{\odot}$  and while they are all slightly different shapes they all undergo essentially the same pattern. I will describe the path followed by a  $1M_{\odot}$  star and relate it to the numbered stages shown in the figure.

Point 1 is the point the core becomes a protostar as mentioned above. As the protostar radiates energy, gravity contracts it further and increases its temperature. The increase in temperature moves the protostar towards the left of the H-R diagram but a more striking effect is the drop in luminosity associated with the reduction in size of the protostar, stage 2. For more massive protostars the reduction in size and luminosity is less pronounced as their higher mass means that the interior of the protostar generates much more heat and supports the collapsing outer layers more rapidly than in low mass stars.

Over the next  $10^6$  yrs or so (SP05) the protostar continues to contract and its temperature continues to rise but now the rise in temperature dominates the luminosity so the protostar moves left and up across the H-R diagram, stage 3. Eventually the core reaches around  $10^7$  K and ignites a self sustaining nuclear fusion reaction and the radiation pressure produced by this steadily halts the contraction of the star. The temperature continues to rise slightly while the contraction continues but once again the contraction is the dominant force in determining the protostars luminosity and so it moves left and down on the H-R diagram and onto the main sequence, stage 4. This stage may take around  $10^7$  yrs (SP05) with the protostar becoming a main sequence star once radiation pressure balances the gravitational contraction and the star settles into a state of hydrostatic equilibrium.

As mentioned above there are unique observational signatures indicative of the different stages of YSO and these are found in the near to far - IR and mm region of the protostar's spectrum. Until a protostar is formed in the heart of a collapsing cloud core the dust is cool (10sK) and gives off very little IR emission. Once a young star is formed the spectrum takes on the appearance of that of a star but with a vast IR and sub-millimetre excess caused by the orbiting dusty material reprocessing the starlight to longer wavelengths. As the disk settles out to a much less vertically thick structure and steadily accretes onto the star or forms young planets the amount of IR excess detected drops and disk life times are thought to be in the region of 10Myrs (Jayawardhana

2006). These stages are shown in figure 1.4 with the class names the broad stages are generally associated with.

Class 0 is a deeply embedded protostar and its Spectral Energy Distribution (SED) is dominated by emission from cold dust. Class I is an embedded protostar still emitting in the far IR and sub-millimetre portions of the spectrum. Class II is a classical T Tauri star (the central star becomes visible at inclinations where the settling disk material no longer obscures it at this stage) and class III is a weak line T Tauri (these are covered in the next section) with a more evolved and depleted protoplanetary disk. These later classes show SEDs dominated by optical and near IR emission with the IR emission lessening as the objects evolve. The inclination of the system can confuse the classification of these objects when considering their SEDs as an inclined disk that obscures the central star will have a SED that is faint in the optical but bright at far – IR like a class I source so care must be taken (Chiang & Goldreich 1997).

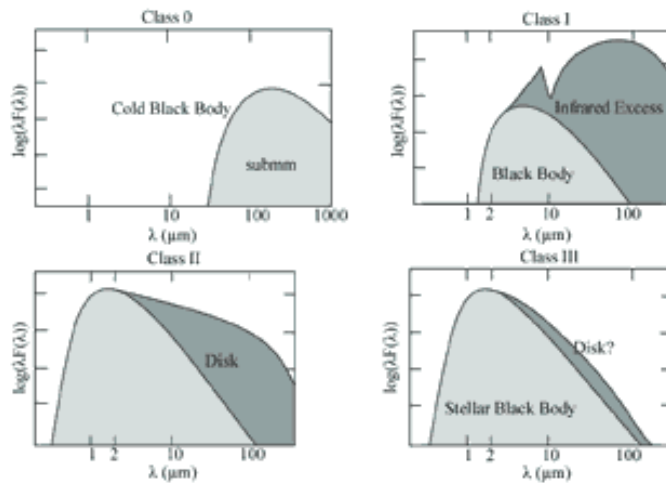


**Figure 1.4** Diagram showing the spectral energy distributions of YSOs at different stages of evolution. Class 0 is a deeply embedded protostar, Class I is an embedded protostar, Class II a classical T Tauri Star and Class III a weak line T Tauri Star. Image taken from Burton (2005).

### 1.3 T Tauri Stars

T Tauri Stars (TTS) are young ( $<10^7$  yr), low mass ( $< 2M_{\odot}$ ), pre-main-sequence stars (Furlan et al. 2006). They are best known for the distinctive infrared and ultraviolet excess found in their spectral energy distributions and their photopolarimetric variability. They were first defined by Joy (1945) on the basis of their photometric and spectroscopic properties. They were of spectral types F5 to G5 and had emission lines resembling the solar chromosphere. He identified eleven stars in his initial study that



displayed similar characteristics and selected the star T Tau as the typical star in the group due to it being the best known, among the brightest and having all the features in emission and absorption he had seen in his study. His observations weren't sufficient to determine a definite series of variations that were uniquely characteristic of the group but he was able to note that the variations were quite different from other known variable stars. Their youth was inferred by their association with bright nebulae in which they were thought to have formed and also the presence of lithium absorption lines in their spectra. Lithium absorption is weak or absent in evolved late-type stars as it is depleted during the main-sequence stage by proton capture reactions.

Herbig (1977) found a match between the radial velocities of fifty TTS in the Taurus Auriga star formation region and their associated molecular cloud. This result was confirmed with a proper motion study by Jones & Herbig (1979). Earlier, Herbig (1962) had defined the optical spectroscopic criteria for TTS as; a) hydrogen Balmer lines and Ca II (H & K) lines in emission, b) anomalous Fe I  $\lambda 4063$  &  $4132$  often observed, c) forbidden emission of O I and S II and d) Li I  $\lambda 6707$  being conspicuously strong. These simplify to TTS being associated with a region of obscuration, having H $\alpha$  and Ca II (H & K) emission and being of spectral type F or later. Similarly, Bastian et al. (1983) found that "T Tauri Stars are stellar objects associated with a region of obscuration; in their spectrum they exhibit Balmer lines of Hydrogen and the Ca II (H & K) lines in emission, the equivalent width of H $\alpha$  being at least  $5\text{\AA}$ . There is no supergiant or early-type (earlier than late F) photospheric absorption spectrum."

In molecular clouds such as  $\rho$  Ophiuchi several different populations of low-mass stars have been found in different regions of the cloud. These different populations are observable in quite different spectral domains and this has led researchers to theorise that they represent different stages in the evolution of low-mass stars, from protostars to pre-main-sequence. Adams et al. (1987) defines class I sources as sources that are only seen in the IR with flat or rising spectra towards longer wavelengths while Lada and Kylafis (1999) note that class I sources have SEDs that are broader than single blackbody functions and peak at far-IR or sub-millimetre wavelengths. These sources are deeply embedded and are thought to be the youngest of the stages. Class II sources have SEDs typical of TTS and class III sources have reddened blackbody-like SEDs and are found on the periphery of the clouds so presumably correspond to a more evolved state. These "older" class III sources show x-ray emission that is thought to be related to solar-type coronal magnetic activity also hinting at the evolved state. There is strong

observational evidence for magnetic fields playing a large part in the many of the observed features of TTS from x-ray emission mentioned above through accretion of material along magnetic field lines to the pronounced variability observed in some sources (Bouvier et al. 2007). TTS have features of each evolutionary stage from protostellar outflows to large star spots (shown in figure 1.5) making these objects very complicated to study but also making them a very important phase in stellar evolution.

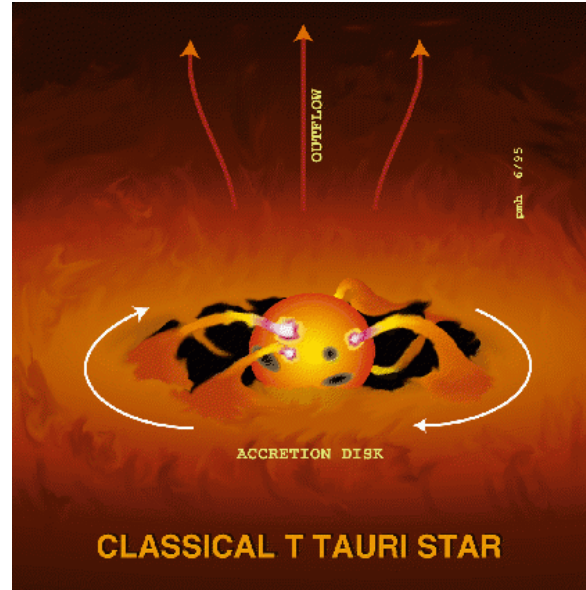


**Figure 1.5** Diagram showing the range of features exhibited by T Tauri stars. The circumstellar accretion disk can be seen depositing material on the stellar surface and producing hot spots and the strong wind/outflow is also shown. Image taken from Hartigan et al. (1995)

T Tauri stars are separated into three main classes that have their own spectral signatures and individual variability. These are reviewed in the following sections.

### 1.3.1 Classical T Tauri Stars

A feature of TTS is their strong  $H\alpha$  emission and the infrared and blue-ultraviolet excess in their spectra, stars with these features and matching the other criteria are known as Classical TTS (CTTS). Their optical spectra consists of a stellar continuum, a stellar absorption spectrum, a superimposed non-photospheric continuum and an emission-line spectrum and their absorption resembles a late-type (K-M) dwarf or sub-giant star. The IR excess is due to reprocessing of stellar photons in the dusty disks that orbit these young stars. In some CTTS the photospheric absorption lines are not detectable without high resolution spectroscopy as they are obscured by the brighter,

superimposed emission and the non-photospheric continuum. This is thought to be from bright, high temperature accretion shocks with temperatures of around 8000K compared to temperatures at the stellar surface of around 4000K (D'Alessio et al. 2003). This phenomenon is known as veiling and it makes the determination of rotation velocities very difficult and means available data is biased towards stars with low activity.

A study by Vogel & Kuhi (1981) discovered that most low-mass stars actually rotate far slower than had been previously thought. It was assumed that such newly formed stars would have high specific angular momentum and would be rotating at close to break-up velocity. This being the case it was then assumed that the high activity levels seen in these objects would merely be solar-type activity exaggerated by the high rotation (Mestel 1968). This result implied that the angular momentum must somehow be lost from the system (Lynden-Bell & Pringle 1974) prior to the CTTS stage and another mechanism for the activity would need to be found. The activity spoken of here is the periodic and irregular variation of the photometry caused by stochastic accretion on to the stellar surface (Vrba et al. 1989, 1993 & Bouvier et al. 2007). The excess continuum mentioned above that is responsible for the veiling is believed to arise in the boundary layer of an accretion disk (Greene 2001) where magnetic braking caused by the stellar dipole magnetic field passing through the disk slows material in the disk (shown in figure 1.6) and causes collision shocks as it “piles up”.

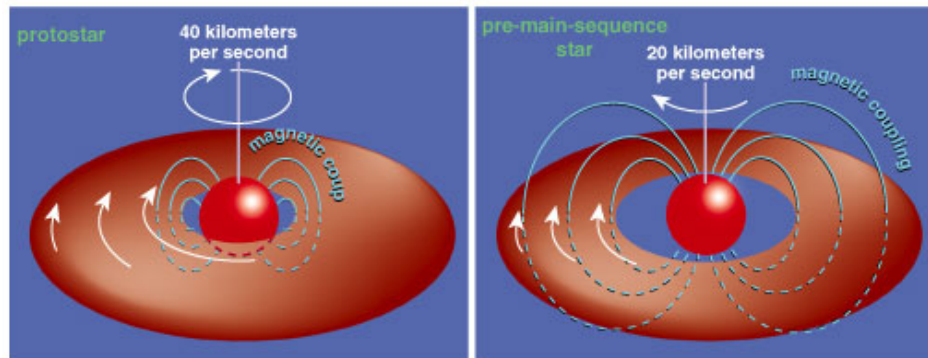


**Figure 1.6** Diagram depicting the stellar magnetic field threading the circumstellar disk and slowing the young stars rotation while truncating the inner radius of the disk. Taken from Greene (2001).

The radius that this occurs at is known as the disc truncation or co-rotation radius (Kenyon et al. 1994) and is given by

$$R_c = \left( \frac{GM_*}{\Omega_*^2} \right)^{1/3}$$

where  $G$  is the gravitational constant,  $M_*$  is the stellar mass and  $\Omega_*$  is the stellar angular rotation velocity. The disk material slowed in the process described above is then channelled by the magnetic field along an accretion column or funnel flow (Romanova et al. 2002) where matter impacts the stellar surface producing further shocks and excess UV continuum. Herbst et al. (1994) argue that the principle cause of the large amplitude variations seen in CTTS is the variable veiling continuum arising in transient regions of higher temperature where accretion energy is dissipated at the disk inner boundary or truncation radius, described above, where the disk material's steady journey towards the central star is suddenly halted and the material 'piles up', this they refer to as type II variability. They also define a type IIp variability which is slightly more stable and has periods corresponding to a few stellar rotations. This is believed to be caused by hot spots on the stellar surface at the base of magnetically channelled accretion columns (Bertout et al. 1988).

### **1.3.2 Weak Line T Tauri Stars**

TTS fitting every other requirement of the definition but lacking in  $H\alpha$  are known as Weak TTS (WTTS) or 'naked' T Tauris as, in general, they also tend to lack the striking infrared excess and therefore the photon reprocessing disk found around CTTS. This absence of an accretion disk is believed to be the principal difference between WTTS and CTTS (Bertout 1989). Some WTTS systems have been observed to have virtually no near-IR as normal but excess in the mid and far-IR regions (Strom et al. 1989), this may be due to WTTSs having disks with large inner regions devoid of matter indicating that it has been accreted onto the central star or is condensing in the disk itself to form planetary bodies (Appenzeller & Mundt 1989).

A mechanism for accelerating the clearing of the inner regions of the disk has been proposed by Chiang and Murray-Clay (2007). Here coronal X-rays ionize the inner disk material allowing a magneto-rotational instability to form. The ionized material then flows from disk to star along the field lines more rapidly than before. WTTS show variations like those of CTTS but these variations are more stable and can be observed over hundreds to thousands of rotations (Herbst et al. 1994), they are classed as type I variations by Herbst et al. (1994). The variations are seen in the V, R & I bands and can be wholly attributed to large cool spots. The variation amplitudes decrease as we move to redder colours as there is less contrast between the cool spot and the hotter photosphere at longer wavelengths.

The cool spots are the footpoints of large magnetic loops on a scale of several stellar radii and are found at high latitudes on both hemispheres of the star (Andre et al. 1992). Hatzes (1995) uses Doppler imaging to derive the surface distribution of these spots and shows that they endure for periods of many years (nearly a decade) at high latitude.

### **1.3.3 Early T Tauri Stars**

Type III variations in the Herbst et al. (1994) scheme are variations that cannot be accounted for by either a rotating spotted surface (type I) or by changes in the veiling continuum (type II). In these stars there is no observed veiling continuum but the variations are irregular and of a similar scale as those of type II. These variations are only seen in stars of type K1 and earlier, up to A0, and have therefore been given the name Early T Tauri Stars (ETTS). Their variation is believed to be accretion driven as well but it is not understood as well as for the later type stars. Stars any earlier than A0 show no variation at all (Herbst et al. 1983).

### **1.3.4 Jets & Outflows**

Perhaps the most striking feature of YSOs are the spectacular collimated bipolar jets and strong winds observed in a number of sources. The occurrence of these mass flows helps explain the inefficiency of star formation in terms of the amount of the collapsing core's mass that is retained by the resulting star after the formation process. These outflows are typically found in embedded young stellar objects where the central star is still obscured in the optical by a massive envelope (Mundt et al. 1987).

An example of this is IRS5 (shown in figure 1.7) in the L1551 region of the Taurus-Aurigae star forming region which is a deeply embedded class I source. A more visually stunning example is the edge on class II T Tauri star HH 30 where there has been a lot of recent work and some spectacular high resolution images taken showing the collimated outflows and the dark dusty lane of the disk (Cotera et al. 2001; Burrows et al. 1996), shown in figure 1.8.

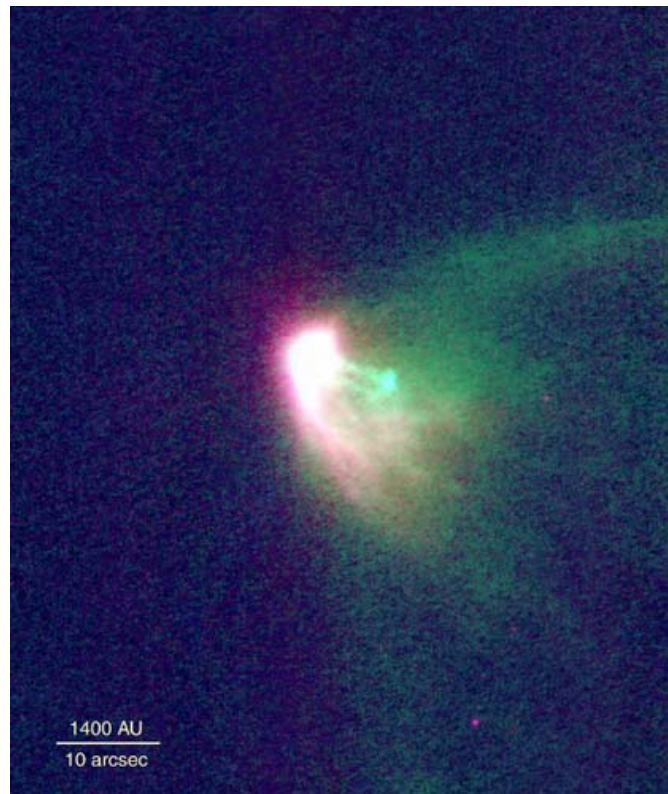


**Figure 1.7** Image of the cavity and jet from L1551 – IRS5 taken from the Subaru Telescope, National Astronomical Observatory of Japan library.

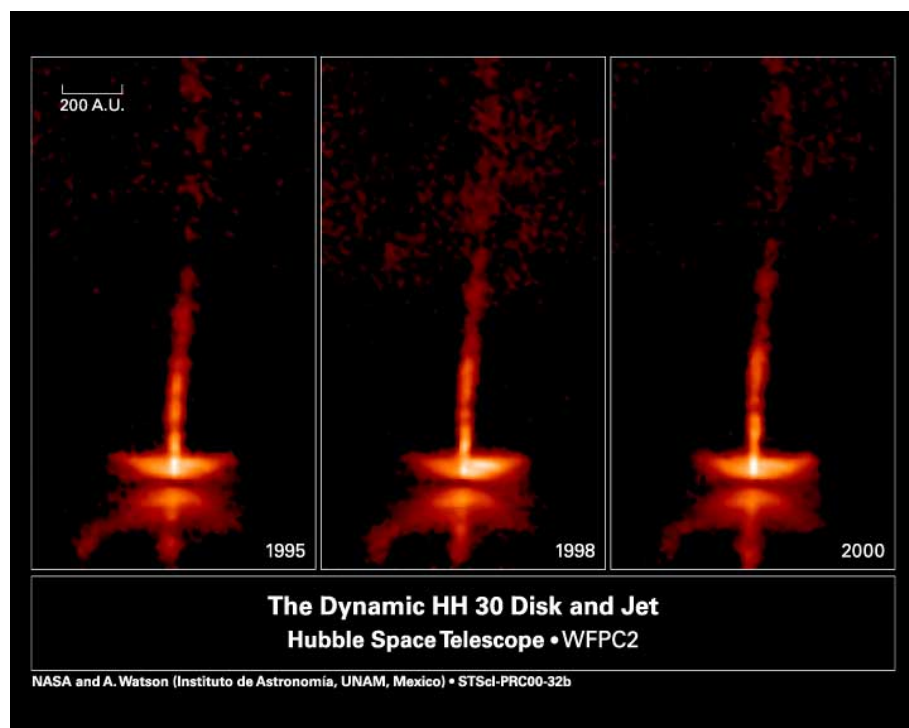


**Figure 1.8** These images of HH 30 show changes over a five-year period in the disk and jets of this young star. The pictures were taken with the Wide Field and Planetary Camera 2 aboard NASA's Hubble Space Telescope.

The jets and outflows are at their most energetic in the class 0 phase when the forming protostar is heavily embedded in its collapsing envelope. In the T Tauri phase the jet becomes less energetic and optically visible and in WTTS where the disk has been depleted the jets are no longer present (Pudritz et al. 2007). This leads to the conclusion that these very energetic mass and radiation loss mechanisms are driven by the accretion disks themselves. If the disk then dissipates through accretion on a timescale of the duration of the CTTS phase (or slightly less) then a gradual transition from T Tauri to main-sequence can be expected.

There is more evidence to support the fact that objects like HH 30 are a precursor to the ‘ordinary’ CTTS stage in the effect that jets and outflows have on the envelopes that the young stars are embedded in. Not only do the jets carry away mass (as much as  $10^{-6}M_{\odot} \text{ yr}^{-1}$  in comparison to accretion onto the star at rates of around  $10^{-9}M_{\odot} \text{ yr}^{-1}$ ) and angular momentum allowing the star to maintain a stable rotation and accretion but they also open up cavities in the envelope above the poles of the star. This process speeds up the clearing of the envelope as the wind steadily widens out the cavities while mass continues to accrete onto the disk and opens up sight lines to the central star so that it becomes visible in the optical and reaches the CTTS stage of its evolution.

#### **1.4 Radiation Transfer**

To investigate the observational signatures of protoplanetary disk accretion, dust settling and dynamics I have adapted and extended a suite of 3D Radiation Transfer codes. With these codes I have the ability to set up any geometry and illumination that may be required to study a particular environment on a 3D grid. I then use the Monte Carlo Radiation Transfer method to track photon/energy packets on random walks through the simulated environment, e.g. a protoplanetary disk. The Monte Carlo method of solving the equation of radiation transfer is adopted due to its efficiency in simulating the radiation transfer in complex 3D systems. The various codes developed here output the photopolarimetry, Spectral Energy Distribution, scattered light images, molecular line profiles and channel maps which can then be compared with observations.

In the next section I will give a brief overview of the Monte Carlo method itself and its application to the environments I have investigated. The code developments and extensions that have been made for specific investigations are described in detail in the relevant chapters. Throughout the rest of this section I will briefly describe the equation of radiation transfer and important solutions here.

The transfer equation is often quoted as:

$$\frac{dI_\nu}{ds} = -\alpha_\nu I_\nu + j_\nu \quad (1.1)$$

where  $\frac{dI_\nu}{ds}$  is the rate of change of radiation intensity,  $I_\nu$ , with distance,  $s$ . The subscript  $\nu$  indicates the frequency dependency of the quantity. The rate at which this changes depends on the absorption coefficient  $\alpha_\nu$  and the emission coefficient,  $j_\nu$ . The specific intensity,  $I_\nu$ , is the amount of energy per unit volume emitted in a given solid angle,  $d\Omega$ , in a given frequency range,  $d\nu$ , per unit time and is often expressed as:

$$dI_\nu = \frac{dE_\nu}{dV d\Omega d\nu dt \cos \theta}$$

The absorption coefficient,  $\alpha_\nu$ , is also known as the extinction coefficient and is a measure of the average distance over which a photon can travel before being absorbed (its mean free path length). The emission coefficient,  $j_\nu$ , gives the energy added to the radiation field through emission or re-emission from the intervening dusty material and has the same units as the specific intensity. The optical depth,  $\tau_\nu$ , of a region is often quoted when discussing radiative transfer and it is simply the number of mean free path lengths along the observer's line of sight and is expressed as:

$$d\tau_\nu = \alpha_\nu ds$$

The source function,  $S_\nu$ , is the ratio of total emissivity to total opacity or absorption and is expressed as:

$$S_\nu = \frac{j_\nu}{\alpha_\nu} \quad (1.2)$$

Using equation 1.2, equation 1.1 can be written as:

$$\frac{dI_\nu}{d\tau_\nu} = -I_\nu + S_\nu \quad (1.3)$$

This expression is a first order differential equation and can be solved by multiplying by

an integrating factor; here the factor is  $e^{\int_0^{\tau_\nu} d\tau_\nu} = e^{\tau_\nu}$ , giving:

$$\begin{aligned} \frac{dI_\nu}{d\tau_\nu} e^{\tau_\nu} + I_\nu e^{\tau_\nu} &= S_\nu e^{\tau_\nu} \\ \frac{d}{d\tau_\nu} (I_\nu e^{\tau_\nu}) &= S_\nu e^{\tau_\nu} \end{aligned} \quad (1.4)$$



Integrating equation 1.4 along the observer's line of sight (effectively over the optical depth) from 0 to some optical depth  $\tau_\nu$  gives:

$$\int_0^{\tau_\nu} \frac{d}{d\tau_\nu} (I_\nu e^{\tau_\nu}) d\tau_\nu = \int_0^{\tau_\nu} S_\nu e^{\tau_\nu} d\tau_\nu$$

If we consider a slab of material in a gaseous nebulae or the dusty environment of a T Tauri star and make  $S_\nu$  constant with  $\tau$  then this has the solution:

$$I_\nu e^{\tau_\nu} - I_0 = S_\nu (e^{\tau_\nu} - 1)$$

when  $I_0$ , the background intensity, is zero this becomes:

$$I_\nu = S_\nu (1 - e^{-\tau_\nu})$$

This solution has of course assumed that the source function does not vary across the YSO under study and is not a function of  $\tau$ , which is a very restrictive assumption. To model a realistic stellar environment the radiative transfer equation must be solved for a variable  $S_\nu$ . There are several different methods of achieving this but the one I have used throughout the research in this thesis is the Monte Carlo method which I will discuss in section 1.5.

To solve the source function it must first be expressed in a form more suitable for simulation and to do this we have to first express the emission and absorption coefficients in terms directly relating to the energy level transitions that electrons in the absorbing and emitting materials undergo. These transitions are governed by the Einstein coefficients and their relations to one another and I will briefly discuss these here.

Kirchoff's law,  $j_\nu = \alpha_\nu B_\nu(T)$ , states that for a material whose emission is only dependant on its temperature the radiation emitted must equal the radiation absorbed if the system is in thermodynamic equilibrium. Einstein realised that this implied a statistical relationship between the number of absorptions and emissions of individual energy levels of the atoms/molecules in the material under study. He considered two levels separated by an energy  $h\nu$ , in a radiation field  $\bar{J} = \int_0^\infty J_\nu \phi(\nu) d\nu$  where  $J_\nu$  is the radiation at a particular frequency and  $\phi(\nu)$ , the line profile function where  $\int_0^\infty \phi(\nu) d\nu = 1$ . The electrons moving between the energy levels that are responsible for absorbing and emitting radiation can move in one of three different ways each with its own coefficient describing this movement, spontaneous emission, stimulated emission

and absorption. There is another way in which transitions can be induced in materials, this is collisional excitation or de-excitation and is important in higher density environments and must be considered when investigating molecular line emission like that of the CO molecule discussed in chapter 4.

Spontaneous emission is the random emission of radiation by the transition of an electron in some excited state to a lower energy level. This transition has a probability of occurring represented by the Einstein A coefficient,  $A_{ul}$ , and expressed in units of probability per second. The subscript denotes the direction of the transition, in this case from some upper level,  $u$ , to some lower level,  $l$ . This form of emission takes place in the absence of a radiation field whereas stimulated emission is the emission of radiation by a transition from an excited energy state to a lower energy level triggered by the presence of a radiation field. Stimulated emission is denoted by  $B_{ul}$  and is one of the two Einstein B coefficients. Absorption is the second of the Einstein B coefficients and is similar to the first as it also requires the presence of a radiation field. In this case however the radiation stimulates an electron to move up from a lower energy level to a higher one, absorbing energy from the radiation field as it does this. It is in effect the reverse of stimulated emission and so is denoted by  $B_{lu}$  with the subscripts marking the opposite direction of the electron transition.

If the system is in equilibrium then the number of emissions will equal the number of absorptions so the three coefficients can be related by

$$n_l B_{lu} \bar{J} = n_u A_{ul} + n_u B_{ul} \bar{J}$$

where  $n_l$  and  $n_u$  are the number of molecules in the lower and upper energy states respectively. The above expression can be rearranged to give

$$\bar{J} = \frac{\frac{A_{ul}}{B_{ul}}}{\frac{n_l}{n_u} \frac{B_{lu}}{B_{ul}} - 1}$$

the ratio of the level populations can be replaced by  $\frac{n_l}{n_u} = \frac{g_l}{g_u} e^{\frac{h\nu}{kT}}$ , which represents the ratio of the level populations in thermodynamic equilibrium, giving

$$\bar{J} = \frac{\frac{A_{ul}}{B_{ul}}}{\frac{g_l B_{lu}}{g_u B_{ul}} e^{\frac{h\nu}{kT}} - 1}$$

In thermodynamic equilibrium the radiation field is equal to the Plank function (i.e.

$$\bar{J} = \frac{2h\nu^3/c^2}{e^{h\nu/kT} - 1}) \text{ so the above expression can be simplified to give}$$

$$g_l B_{lu} = g_u B_{ul} \quad (1.5)$$

and

$$A_{ul} = \frac{2h\nu^3}{c^2} B_{ul} \quad (1.6)$$

where  $g_l$  and  $g_u$  are the degeneracies (the number of ways the angular momentum,  $J$ , may be orientated in space – equal to  $2J+1$ ) for the lower and upper energy levels respectively.

The Einstein coefficients are properties of individual molecules and as equations 1.5 and 1.6 only contain the coefficients and some physical constants they are independent of the environmental conditions of the molecules and hold even outside thermodynamic equilibrium. There are two possible definitions for the Einstein B coefficients depending on whether the emission is being considered in terms of the local radiation intensity (as above) or the local energy density. The equivalent of equation 1.6 in terms of energy density is

$$A_{ul} = \frac{8\pi h \nu^3}{c^3} B_{ul}$$

and one must be careful in making sure the correct definition is used to avoid any problems that the factor of  $\frac{4\pi}{c}$  difference will cause.

Having defined the transition coefficients I can now return to the emission and absorption coefficients from the radiation transfer equation. The emission coefficient can now be seen as the energy per transition ( $h\nu$ ) multiplied by a function measuring the rate of change of the upper level population with frequency  $\left(\frac{dn_u}{d\nu}\right)$  multiplied by the probability of a molecule undergoing a spontaneous level transition over  $4\pi$  steradians, giving

$$j_\nu = \frac{h\nu}{4\pi} \frac{dn_u}{d\nu} A_{ul} \quad (1.7)$$

which is the energy density emitted at a particular frequency,  $\nu$ , in all directions per unit volume per second. Expressing the absorption coefficient in this manner gives

$$\alpha_\nu = \frac{h\nu}{c} \left( \frac{dn_l}{d\nu} B_{lu} - \frac{dn_u}{d\nu} B_{ul} \right) \quad (1.8)$$

the amount of energy absorbed per unit volume per second. Using the definition of the source function (equation 1.2) and the expressions for  $\alpha_\nu$  and  $j_\nu$  given above in equations 1.7 and 1.8 the source function becomes

$$S_\nu = \frac{\frac{h\nu}{4\pi} \frac{dn_u}{d\nu} A_{ul}}{\frac{h\nu}{c} \left( \frac{dn_l}{d\nu} B_{lu} - \frac{dn_u}{d\nu} B_{ul} \right)}$$

This can be simplified using the relationships between the Einstein coefficients given in equations 1.5 and 1.6 to

$$S_\nu = \frac{2h\nu^3}{c^2} \left[ \frac{1}{\frac{g_u}{g_l} \frac{dn_l}{d\nu} \frac{d\nu}{dn_u} - 1} \right] \quad (1.9)$$

the  $\frac{dn_l}{d\nu} \frac{d\nu}{dn_u}$  term can be expressed as  $\frac{dn_l}{dn_u}$ . Differentiating the expression for the ratio of level populations shows that

$$\frac{dn_u}{dn_l} = \frac{g_u}{g_l} e^{\frac{h\nu}{kT}} = \frac{n_u}{n_l}$$

and substituting this into 1.9 finally, gives an expression for the source function

$$S_\nu = \frac{2h\nu^3}{c^2} \left[ \frac{1}{\frac{g_u}{g_l} \frac{n_l}{n_u} - 1} \right]$$

### 1.5 Monte Carlo Method

The Monte Carlo method of solving the radiation transfer equation is perhaps the most versatile of the available methods (although it can be inefficient for high optical depth systems) and can readily be adapted to operate in any geometry or environmental simulation. The method gets its name from the statistical approach to solving the transfer equations that relies on the generation and tracking of photon packets travelling on random paths through the simulation.

Monte Carlo Radiation Transfer (MCRT) techniques have been developed for astronomy simulations by a number of groups including Bernes (1978), detailed in

chapter 4, Ménard (1989) – modified by Pinte et al. (2006), Wolf, Henning & Stecklum (1999), Lucy (1987, 1999a&b and most recently 2005), Dullemond & Dominik (2004a). The earlier development of the code used in this research is detailed in a number of papers (Code & Whitney 1995; Whitney & Hartmann 1992, 1993; Wood et al 1996; Bjorkman & Wood 2001) and this method has been modified to include a three dimensional spherical polar grid (Whitney & Wolff 2002), accretion and diffusion in the inner regions of the disk (Wood et al. 2002b; Bjorkman, Whitney & Wood 2003) and solve for the density structure for a disk in vertical hydrostatic equilibrium (Walker et al. 2004).

The MCRT codes reproduce the observational characteristics of a region of dust and gas by generating a representative number of ‘photon packets’ and then tracing the random walks these packets take through the region as they interact with the material present. The interactions include the absorption, re-emission and scattering of photons of different wavelengths or energies in directions chosen from the scattering phase functions. The more photon packets simulated in the system the more precise the results will be due to the increase in signal to noise, like a longer exposure for an observation. The versatility and range of this type of simulation’s applications are only limited by high optical depth which can increase inefficiencies. As computers get more powerful ever more complicated and accurate simulations can be performed with this method, making it a very powerful tool.

The luminosity of the radiation source (generally the central star in the star/disk system) is divided equally into monochromatic ‘energy packets’ or ‘photon packets’, see Bjorkman & Wood (2001).

$$E_{\gamma} = \frac{L}{N} \Delta t$$

These packets represent a number of photons that will undergo interactions as they travel through the circumstellar material and I will refer to them as photons from now on.

The photons are emitted outwards from the surface of the central source (throughout the work in this thesis a spherical central star with no limb darkening is used) and followed to random interaction locations. The region the photons are emitted into is a 3D spherical polar grid onto which the density is discretised, this allows for the straightforward integration of optical depth through the grid. Since the density in each cell is computed only once at the beginning of the processing, a range of analytic

density structures or tabular densities derived from hydrodynamical simulations can be incorporated. The more cells, in the grid, the more accurate the simulation will be but, again, the longer the simulation will take to run due to integrating through a finer grid in order to determine the optical depth.

The photon interaction locations are determined by the optical depth encountered over the path length and the type of interactions undergone by the photon (absorption or scatter) are determined from a probability given by the albedo, defined as

$$a = \frac{n_s \sigma_s}{n_s \sigma_s + n_a \sigma_a}$$

where the subscripts refer to the number densities and cross sections of the scatterers and absorbers respectively. The cross section,  $\sigma$ , is the energy per second per frequency per solid angle (number of photons) that is removed from the direction of travel by scattering or absorption and has units of area ( $cm^2$ ).

The key to the Monte Carlo technique is its ability to sample a probability distribution function,  $P(x)$ , using a cumulative distribution function,  $\Psi(x_1)$ . Mathematically this is,

$$\xi = \int_{x_0}^{x_1} P(x) dx = \Psi(x_1)$$

where  $\xi$  is a random number sampled uniformly from the range 0 to 1,  $x_0$  is the lower limit of the range over which  $x$  is defined. Here we wish to find how far the photon travels before being absorbed or scattered and to do this we use the fact that the probability a photon travels an optical depth  $\tau$  without an interaction is given by  $e^{-\tau}$ . The probability of scattering before  $\tau$  is  $1 - e^{-\tau} = \Psi(\tau)$  and we can therefore sample the cumulative probability using  $\xi = 1 - e^{-\tau}$ , giving

$$\tau = -\log(1 - \xi)$$

The physical distance,  $L$ , travelled by the photon can then be calculated using the sampled random optical depth,

$$\tau = \int_0^L n \sigma dl$$

When a photon enters the simulation the distance from the photon's position to the nearest cell boundary along the photon's direction of travel is calculated and the optical depth the photon encounters over this distance is simply that of the cell (discretised radial optical depths having been calculated for each cell). If the optical depth encountered by the photon over this path is less than  $\tau$  the photon is moved to the next cell and the optical depth it has encountered thus far is recorded. This process is

repeated until the total optical depth encountered by the photon is greater than  $\tau$ . When this occurs the photon undergoes an interaction at this location and the nature of the interaction is determined by the albedo of the material. A further random number,  $\xi$ , is generated and if  $\xi > a$ , the photon is absorbed and if  $\xi < a$ , the photon is scattered.

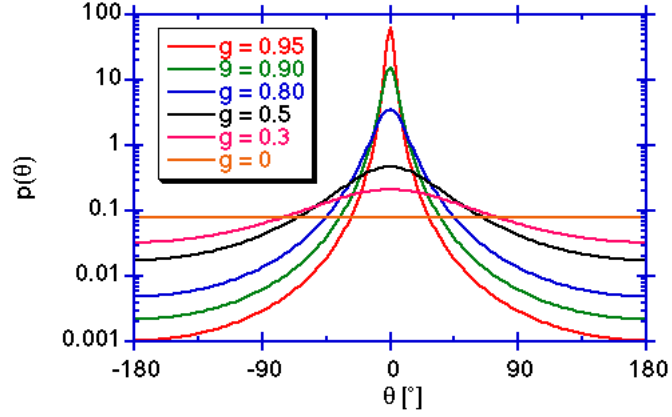


**Figure 1.9** Shows a series of Henyey-Greenstein functions with the forward direction of the photons original trajectory at  $0^\circ$  and backwards scattering at  $180^\circ$ . The curve for  $g=0$  has a constant value of  $1/4\pi$ .

If the photon scatters, a random scattering angle is obtained from the scattering phase function which is approximated using the Henyey-Greenstein function (equation 1.10), with forward-scattering parameter  $g$  computed at each wavelength from the optical properties of the scattering material (generally the small grains of Mathis, Rumpl & Nordsieck 1977, MRN grains, or the larger grains of Wood et al. 2002a, W02 grains, developed for their investigation of the T Tauri star HH30 IRS). Figure 1.9 shows the functions variation in scattering angle  $\theta$  for a range of  $g$  values.

$$P_{hg} = \frac{1}{2} \frac{1 - g^2}{(1 - 2g \cos \theta + g^2)^{3/2}} \quad (1.10)$$

If the photon is absorbed in a cell however, its energy is added to the cell, raising the cell's temperature (Bjorkman & Wood 2001) so that the total energy absorbed in each cell is

$$E_\gamma^{abs} = N_i E_\gamma \quad (1.11)$$

As we assume the simulation is in radiative equilibrium and that dust opacity is independent of temperature any radiation that is absorbed is re-radiated immediately

and as the thermal emissivity of the dust particles is  $j_\nu = \kappa_\nu \rho_\nu B_\nu(T)$ , where  $B_\nu(T)$  is the Plank function at temperature  $T$ , the emitted energy is

$$\begin{aligned} E_i^{em} &= 4\pi\Delta t \int dV_i \int \rho \kappa_\nu B_\nu(T) d\nu \\ &= 4\pi\Delta t \int \kappa_p(T) B(T) \rho dV_i \end{aligned}$$

where  $\kappa_p = \int \kappa_\nu B_\nu d\nu / B$  is the Plank mean opacity and  $B = \sigma T^4 / \pi$  is the frequency integrated Plank function. For a constant temperature in the cell then

$$E_i^{em} = 4\pi\Delta t \kappa_p(T_i) B(T_i) m_i \quad (1.12)$$

where  $m_i$  is the cell mass.

The dust temperature after absorbing  $N_i$  packets for each cell is then found by equating the absorbed (equation 1.11) and emitted (equation 1.12) energies and is given by

$$\sigma T_i^4 = \frac{N_i L}{4N_\gamma \kappa_p(T_i) m_i} \quad (1.13)$$

As the Plank mean opacity  $\kappa_p$  is a function of temperature equation (1.13) must be solved every time a photon packet is absorbed. Fortunately the Plank mean opacity is a slowly varying function so equation (1.13) can be solved with a simple iterative algorithm. In the code described here, pre-tabulated opacity values for each dust type and calculated for a range of frequencies are used.

The new cell temperature is then used to calculate the energy of the re-radiated photon packet so that the heating and cooling are balanced correctly. The packets emitted before the absorption of the latest packet will have carried away an energy corresponding to the cells previous emissivity  $j'_\nu = \kappa_\nu B_\nu(T_i - \Delta T)$ , where  $\Delta T$  is the temperature increase caused by the packet absorption. The previous packets were then emitted with an incorrect frequency distribution due to the previous temperature and this must be corrected for with the additional energy that will be radiated with the new emissivity at the new temperature. The additional energy to be emitted is then given by

$$\Delta j_\nu = j_\nu - j'_\nu = \kappa_\nu [B_\nu(T_i) - B_\nu(T_i - \Delta T)] \quad (1.14)$$

Therefore, to correct previous emission spectra the packet is immediately re-emitted with a frequency chosen from the shape of  $\Delta j_\nu$ . If the temperature change  $\Delta T$  is small equation (1.14) can be simplified to

$$\Delta j_\nu \approx \kappa_\nu \Delta T (dB_\nu / dT) \quad (1.15)$$

Normalising equation (1.15) gives the temperature correction probability distribution



$$\frac{dP_i}{d\nu} = \frac{\kappa_\nu}{K} \left( \frac{dB_\nu}{dT} \right)_{T=T_i}$$

where  $dP_i/d\nu$  is the probability of re-emitting the packet between the frequencies  $\nu$  and  $\nu + d\nu$ , and the normalisation constant is  $K = \int_0^\infty \kappa_\nu (dB_\nu/dT) d\nu$ .

After interacting the photon travels on, on its new path with the scattering and opacity parameters updated accordingly, until the randomly sampled optical depth triggers another interaction and the whole process of absorption, emission and temperature correction is repeated. Once all the photons have been emitted and tracked until they escape the simulation they are placed into frequency and direction-of-travel bins that provide the emergent SED and multi-wavelength images of the object under study.

## 1.6 Dust Settling & Grain Growth

The circumstellar disks that are characteristic of T Tauri class objects are the sites of planet formation and this process must occur between the CTTS stage and the main sequence as by this point there is no longer any trace of circumstellar disks (Appenzeller & Mundt 1989, Brandner et al. 2000). The mixture of dust and gas that initially makes up the protoplanetary disk is usually assumed to be that of the Interstellar Medium (ISM) as it is from this low density material that molecular clouds and protostellar cores form (Duchêne 2003). The disks initially consist of submicron particles and typically the MRN distribution described above with a size range of 0.005 to 0.25 $\mu$ m is used to represent these small particles. Dust and gas in these disks must migrate to the mid plane of the disk where growth and coagulation processes produce particles large enough to become what we would recognise as planetary bodies. The dust grains will experience a gravitational attraction towards the parent star and left to their own devices would orbit in the usual Keplerian fashion. The presence of the gas however causes the dust grains to experience a strong drag effect due to their large surface-to-mass ratio (Dullemond & Dominik 2004b). Viewed in a co-rotating frame the dust would oscillate about the midplane as it orbited but the drag effects of passing back and forth through the gas steadily reduces this oscillation and the particles ‘settle’ towards the midplane. This process of settling causes the mass of material in the midplane to increase and so the gravitational attraction of particles towards the midplane increases. Eventually even the lightest particles will settle in this scenario.

Due to the much higher densities found in this environment than those in the ISM and to processes such as Brownian motion, turbulence and settling, dust particles in disks are always on the move and as such undergo collisions with each other. Number densities of particles are thought to vary from  $\sim 1\text{cm}^{-3}$  in the ISM to a few  $1000\text{cm}^{-3}$  in molecular clouds and from 10 to  $10^{3-5}\text{cm}^{-3}$  in the circumstellar disk environment. The colliding particles coagulate to form larger aggregates of the smaller particles in a variety of processes (e.g. Brownian coagulation, differential settling and turbulent coagulation) depending on the size of particles involved (Dullemond & Dominik 2005).

This process is remarkably efficient and has been shown to totally deplete the gas and small particles in the disk on the order of  $10^6$  years which is too fast to explain observations of the Spectral Energy Distributions (SEDs) of protoplanetary disks of around this age and older (Dullemond & Dominik 2005, Boekel et al. 2003). There are a number of processes that slow the coagulation and may allow a sufficient quantity of smaller grains and gas to remain over the timescales observed in T Tauri stars, i.e. grain growth then shattering to replenish the small grain population. The most common of these is collisional fragmentation which depends on the mass, velocity and binding strength. This process, along with turbulence, mixes grains vertically through the disk to some extent. While different grain sizes have different scale heights there are no sharp layered areas of different particle size but a gradual increase in the number and size of larger particles towards the midplane (Dullemond & Dominik 2005). As the grains and aggregates increase in size they become massive enough to gravitationally attract one another and so form planetesimals which coalesce to form the cores of planets (Nagasawa 2006). These cores will then accrete the gaseous material in the disks to form planetary atmospheres and if they are massive enough, and there is enough gas left in the disk, gas giant planets (Lissauer 1993) and so form planetary systems.

Another observed feature that requires dust settling and grain growth as an explanation is the 10 and  $20\mu\text{m}$  emission bands caused by silicate dust grains of sizes of the order of ISM material. This feature occurs alongside the increased millimetre emission mentioned above that is caused by grains up to 1 mm in size. This is only possible if there is grain growth to produce the millimetre emission and settling of larger grains towards the midplane leaving small dust grains in an optically thin upper layer that can produce the silicate features (Furlan et al. 2005).

What follows is a brief discussion of the processes by which dust settling and grain growth are believed to progress and a description of some of the observational evidence that disks are not in HSEQ and that grain growth has occurred.

### 1.6.1 Review of Recent Studies

Over recent years there have been a number of investigations into the observable effects of dust settling and grain growth on the SEDs of T Tauri disks. These investigations have taken a variety of forms and have progressed in complexity and accuracy as better data and a more complete understanding of the processes involved have become available.

Interestingly it has been shown that ‘flat’ disks without the flaring and thick outer regions associated with HSEQ models can also fit many of the observed SEDs (Adams et al. 1987, 1990; Miyake & Nakagawa 1995; Lada et al. 2006). The results of Miyake & Nakagawa (1995) suggest a progression of the disk structure from an early, well mixed, flared disk to a much flatter disk at later stages with a transition timescale of around  $10^6 - 10^7$  years (comparable to T Tauri lifetimes), shown in figure 1.10.

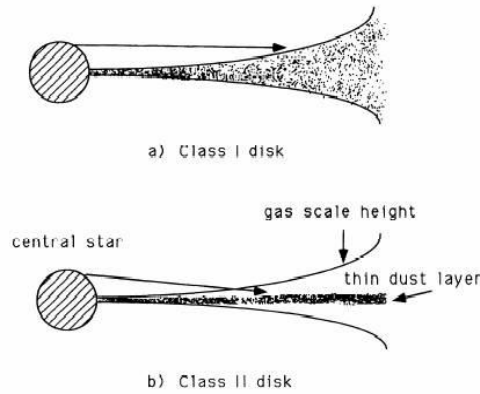


**Figure 1.10** Schematic cartoons which represent the two classes of passive disk investigated: (a) class I disk, which absorbs stellar radiation at the flared surface of the optically thick gas-dust disk and (b) class II disk, where stellar radiation is absorbed at the lowered surface of the dust layer rather than the flared gas layer. Taken from Miyake & Nakagawa (1995).

The disk they use for their theoretical models is optically thick and vertically isothermal with a density profile of:-

$$\rho(r, z) = \frac{\Sigma(r)}{\sqrt{\pi}H} e^{-(z/H)^2} \quad (1.16)$$

$\Sigma(r)$  = Surface Density

$$H = \sqrt{2Cs/\Omega_k}$$

and a radial density distribution dependent on surface density which goes as  $\Sigma(r) \propto r^{-P}$ , where  $P = 1.5$ . They note that the value of  $P$  may be less but this has no effect on the temperature distribution and emergent spectrum as their disks are optically thick and only the disk surface is responsible for the absorption and scattering. They compared observed IRAS fluxes in the mid- to far-IR of 62 T Tauri stars with theoretical SEDs generated using a simple passive, reprocessing disk model. The observed wavelength region corresponds to re-emission from regions with temperature ranging from 30 – 300K, roughly equating to a radii of 0.1 – 100 AU (the region where planet formation must occur to produce planetary systems like our own). They show that they are able to fit a number of the 62 T Tauri stars SEDs with each class of disk and so infer the presence of dust settling at different stages of progression in T Tauri stars. Figure 1.11 shows the difference in the SEDs generated for flat and flared disks compared with observations of UZ Tau which was fit with a flat disk model.

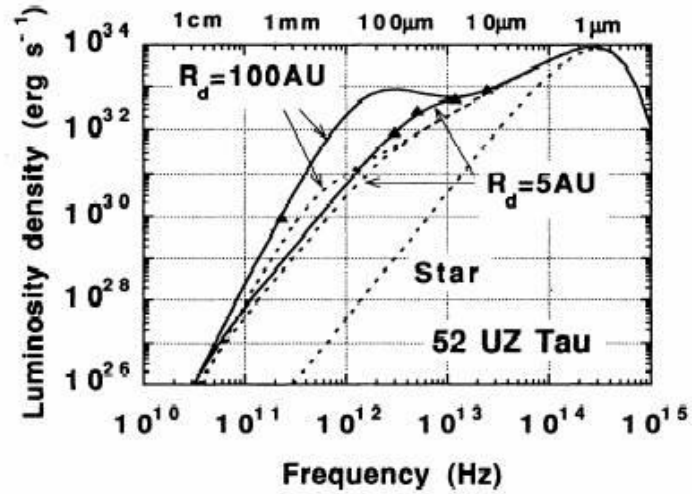


**Figure 1.11** Model SEDs for a flared disk of radius 5 and 100AU are shown by the solid lines while the dotted lines represent flat, thin disks of 5 and 100AU in radius and the emission from the central star. Taken from Miyake & Nakagawa (1995).

The above investigation does not simulate any grain growth and uses a very simple treatment of the disks structure.

Wood et al. (2002a) investigated grain growth in the T Tauri star HH 30 IRS suggested by millimetre and IR data but neglect settling due to a lack of available IRAS data. A further investigation by Cotera et al. (2001) found the apparent width of the dust lane

decreased with increasing wavelength, possibly indicating the settling out of larger particles that scatter longer wavelength radiation. They use a flared disk density structure to represent the disk,

$$\rho = \rho_0 \left( \frac{R_*}{\omega} \right)^{-\alpha} \exp - \frac{1}{2} \left[ \frac{z}{h(\omega)} \right]^2 \quad (1.17)$$

where  $\omega$  is the radial coordinate in the disk midplane,  $\rho_0$  is the density at the stellar surface, and the scale height increases with radius,  $h = h_0 (\omega / R_*)^\beta$ . This disk is then populated with a distribution of grain sizes extending to larger sizes than the standard  $0.005 - 0.25 \mu\text{m}$  ISM distribution derived by Kim, Martin & Hendry (1994, hereafter KMH). An exponential cut-off to the power law is also introduced,

$$n(a)da = C_i a^{-p} \exp \left[ - \left( \frac{a}{a_c} \right)^q \right] da \quad (1.18)$$

The parameters  $p$ ,  $a_c$  and  $q$ , which control the distribution shape, are adjusted to fit the observations.  $C_i$  is set by requiring the grains to completely deplete a solar abundance of carbon and silicon (see Wood et al. 2002a). They find a grain size range of  $0.005 \mu\text{m} - 1\text{mm}$  with  $a_c = 50 \mu\text{m}$  fits the millimetre emission. Figure 1.12 shows the fits obtained with the exponential cut-off, ISM and Coteria grain size distributions.

While this is not a unique fit as a number of parameters could reproduce the observed emission it does demonstrate that grain growth is required and is an observable feature of T Tauri evolution. As no consideration is given to the settling of these larger grains it is difficult to infer much about the time scale of this growth. In this scenario there may be larger than ISM grains in all parts of the disk suggesting that it is an evolved disk.

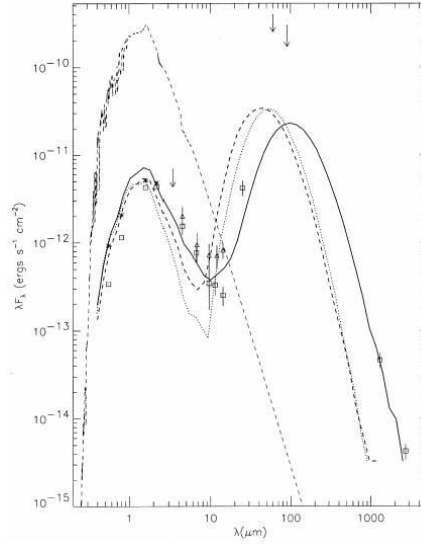


**Figure 1.12** De-reddened data and passive disk models of HH30 at an inclination of  $83^\circ$ . Shows the SEDs generated for three grain size distribution, exponential cut-off (solid line), ISM grains (dotted line) and the Cotera distribution (dashed line). Taken from Wood et al. (2002a).

There have been a number of investigations into the SEDs produced by passive disks in hydrostatic equilibrium (Chiang & Goldreich 1997 & 1999, D'Alessio et al. 1998 & 1999). The passive disk model is adopted for simplicity and only considers heating from the central star, no accretion (although the D'Alessio models include an accretion luminosity term) and assumes that the gas and dust are coupled. These studies self consistently solve the detailed vertical hydrostatic disk structure and determine the vertical height or thickness of circumstellar disks. There is, however, evidence that the models using well mixed, small grain dust distributed throughout the disk are not able to reproduce many of the observed SEDs.

Models by D'Alessio (1999b) using ISM grains in HSEQ with gas produce SEDs with larger far-IR emission than is normally observed in T Tauri sources due to the overly vertically thick outer regions that they derive in the disks. These large disks also have an added problem in that they would obscure the central star in around half of observed T Tauri systems if they were randomly oriented on the sky (D'Alessio et al. 1999b), this does not match observations (see figure 1.13). The combination of these results suggests that some form of dust settling is ongoing in these systems and that we must move away from the simple cases of complete dust and gas mixing in hydrodynamically stable disks.

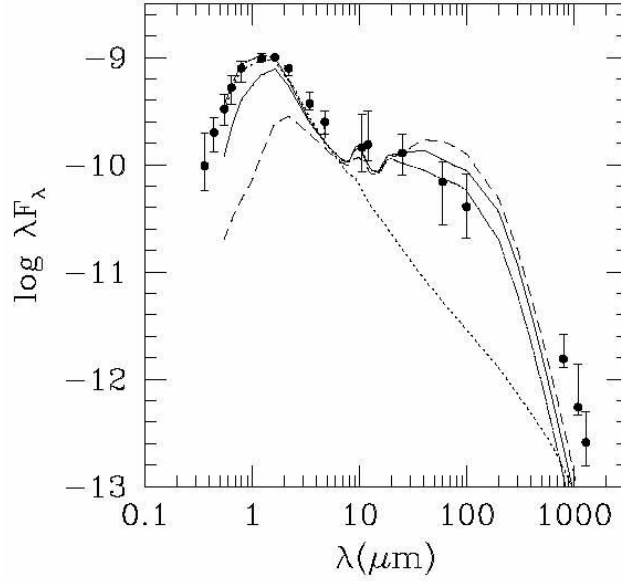


**Figure 1.13** SEDs of three disks all inclined at  $60^\circ$  with radii of 30AU (dot-dashed line), 100AU (solid line) and 300AU (dashed line). The dotted line shows a flat disk. Taken from D'Alessio 1999.

The D'Alessio models using ISM dust also exhibit too little millimetre and submillimetre emission in comparison to observations and it is generally thought that there is some form of grain growth along with the settling of grains to the midplane (Beckwith & Sargent 1991; Manning & Emerson 1994; Pollack et al. 1994) in order to account for this. Larger grains have a larger opacity at millimetre wavelengths and as a result will re-radiate more flux at these wavelengths than smaller grains. In fact the growth of grains has a significant effect on the SEDs of these systems and can to a certain extent negate the need for settling as the larger grains increase the long wavelength opacity while also reducing the optical and near-IR opacity. This in effect reduces the apparent vertical thickness of the disk at short wavelengths and can even reduce the actual thickness by reducing the supporting effect of stellar heating within the disk (D'Alessio, Calvet & Hartmann 2001). A combination of settling and growth is the most likely scenario but as the growth of grains can mimic the effects of settling it is hard to distinguish between the two on observed SEDs.

Simulations of this sort have been conducted by, amongst others, Chiang et al. (2001). Expanding on their HSEQ models (Chiang & Goldreich 1997 & 1999) described above and using a range of particle sizes in a two – layer disk. They divide their passive disk into an upper surface region consisting of hot, small grains with a maximum radius of  $1\mu\text{m}$  and a cool inner region with larger grains, up to a radius of  $1\text{mm}$  (figure 1.14). They find that the overall level of IR excess,  $\lambda \leq 100\mu\text{m}$ , is constrained by the height of

the disk photosphere (the surface at which the disk becomes optically thick),  $H/h$ , in units of the gas scale height. For a well-mixed dust and gas disk, as would be expected in the initial HSEQ phase, this value is around 5. Here values of 1 to 4 were required to fit the observed IR excess levels and this is interpreted as an indication that the material constituting the disk surface layers has settled towards the midplane (figure 1.15). The dust grains are a mixture of metallic iron, amorphous olivine ( $\text{MgFeSiO}_4$ ) and water ice, the absorption efficiency and emissivity of which are calculated using Mie theory (Bohren & Huffman 1983).

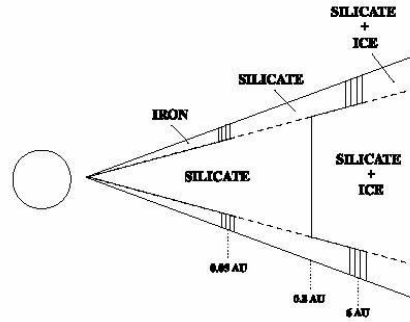


**Figure 1.14** Schematic showing the disk zones and grain composition for the surface and interior regions. Taken from Chiang et al. (2001).

Another result of this approach is that the inclusion of a surface layer of smaller grains allows the model not only to match the reduced submillimetre emission but also the observed mid-IR features around 10, 45 and  $62\mu\text{m}$ , attributed to silicates and water ice (figure 1.15).

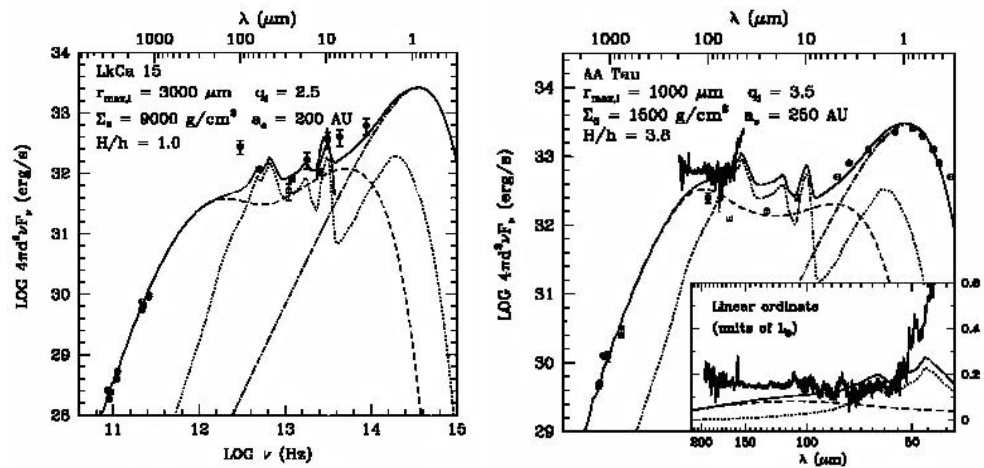


**Figure 1.15** CHIANG model fits to LkCa15 (left) and AA Tau (right) data show disks with  $H/h$  of 1 and 3.8 respectively. Solid lines denote the two layer model fit to the data, the dotted lines denote the contribution from the surface layers and the dashed lines the disk interior. Inset in AA Tau plot shows an enhancement of the region covered by the ISO LWS. Taken from Chiang et al. (2001).



D'Alessio et al. (2001) expand their earlier investigation (D'Alessio et al. 1999b), described above, using a power law size distribution to describe the range of dust present in the disk,

$$n(a) = n_0 a^{-p}$$

where  $a$  is the grain radius,  $n_0$  is a normalisation constant and the exponent  $p$  is a free parameter which was varied between 2.5 and 3.5. The minimum grain size in the distribution was set at  $0.005\mu\text{m}$  and the maximum was varied from  $0.1\mu\text{m}$  to  $1\text{m}$ .

By keeping the disk mass constant and increasing the maximum grain size they are able to simulate the growth of dust grains from a predominantly ISM size distribution to one which favours larger grains. For each increase in dust size they determine the vertical disk structure and calculate the vertical height at which the disk becomes optically thick (the disk photosphere). They find that increasing the particle size alleviates deficiencies in the models described in their earlier paper (D'Alessio et al. 1999b). The larger particle distribution decreases the vertical thickness of the disk and increases millimetre and submillimetre emission, more accurately reproducing observed SEDs and the fraction of stars that aren't extincted by their disks. They note that in order to explain some aspects of observed SEDs, particularly the presence of the silicate emission feature which they are unable to reproduce, some form of size differentiated distribution is required. Limiting larger grains to lower heights within the disk would achieve this and perhaps give a more accurate description of the evolving structure in these sources.

A similar investigation was undertaken by Wood et al. (2002b) and uses the disk structure and parameters determined in their earlier investigation into HH 30 IRS (Wood et al. 2002a) described above. They find that observations across the spectrum reveal a variety of parameters and signatures of disk evolution. Observations in the near-IR can be used to detect disks as they remain optically thick over a wide range of masses in the K – L bands. Observations in the mid-IR ( $20\mu\text{m} \leq \lambda \leq 100\mu\text{m}$ ) are sensitive to the flaring of the disk and can reveal the degree of settling the disk has undergone. While the far-IR emission decreases rapidly with disk mass so could be used to determine a timescale for the mass-loss and evolution of disks.

A detailed investigation into the process and mechanisms involved in dust settling was carried out by Dullemond and Dominik (2004b). Here they started from a well mixed, flared disk in HSEQ like those described earlier and split the disk into a series of radial

annuli but with a steeply varying surface density,  $\Sigma \propto R^{-3/2}$ . For each of these annuli they solved the settling equations in the presence of vertical stirring until equilibrium was reached and the structure of the settled disk was determined. They find that the turbulence mixing the grains is not effective in the low density surface regions of the disk and the material here settles to the midplane unhindered until the density reaches a point where turbulence can counteract the settling. This density varies for grains of different size meaning that over time the upper layers are depleted of larger grains and the disk takes on a more layered structure (although the boundaries between these regions are not sharp). Interestingly they find that as the outer disk is cooler and so falls further before turbulence is able to support the optical surface where most of the reprocessing occurs, it falls into the shadow of the inner disk (figure 1.16).

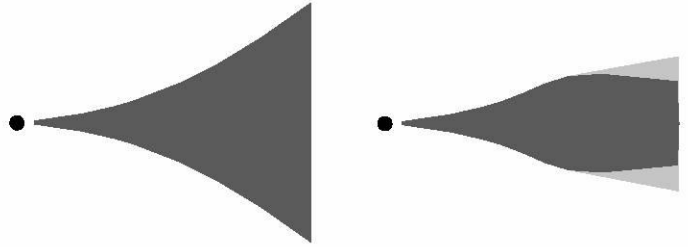


**Figure 1.16** Schematic showing the initial flared disk on the left and the settled, self-shadowed disk on the right. Taken from Dullemond & Dominik (2004b).

They argue that this shadowing effect is more important for the reduction in observed millimetre emission than the effect of a thinner disk absorbing and emitting less radiation as found by Chiang et al. (2001) as the surface area of the disk intercepting direct starlight is vastly reduced. The altitude above the midplane that the surface settles to depends on the dust grain size as does the radius at which the disk becomes self-shadowed. The effects of this settling and shadowing on the model SED are shown in figure 1.17 for a range of epochs. This study neglects viscous heating of the disk for simplicity but the authors state that the inclusion of viscous heating will increase the shadowing effect. They predict that self-shadowed disks will be virtually undetectable in scattered light images for radii greater than about 7AU in the later stages of their evolution ( $\sim 10^6$  years).

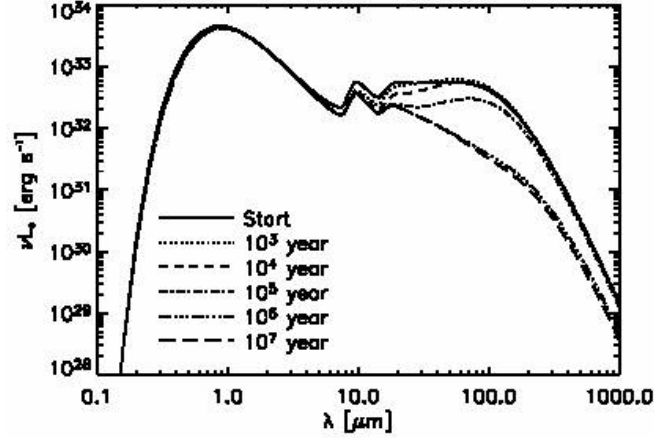


**Figure 1.17** Shows how the model SED changes with time as the settling progresses throughout the disk. Taken from Dullemond & Dominik (2004b).

Furlan et al. (2005) use a flared disk with a self consistently solved vertical structure (D'Alessio et al. 2001) and two layers. The upper layer is populated with ISM grains (Draine & Lee 1984) in the size range  $0.005\mu\text{m} - 0.25\mu\text{m}$ ; the lower disk layer is populated with a distribution of grains from  $0.005\mu\text{m} - 1\text{mm}$ . They then use a grid of models incorporating a range of mass accretion rates, inclination angles and dust-gas ratios (described in D'Alessio et al. 2006) to get the best fit to observations. They find that most of the sources in their sample exhibit some degree of dust settling and growth and that there was evidence for clearing of the inner part of some sources. The reduction in emission from  $5 - 8\mu\text{m}$  and the steeply rising continuum from about  $13\mu\text{m}$  observed in these sources is deemed to be caused by a cleared inner region with an illuminated inner disk wall.

The time evolution of the disk optical thickness was carried out by Tanaka et al. (2005) using a laminar disk for this initial study. The studies described above have concentrated only on dust settling and used some distribution of grain sizes throughout the vertical disk height. This investigation examines settling along with grain growth to determine the combined effect of these two processes on observed SEDs and looks more closely at the sparsely populated upper layers of the disk where previous studies have focused on the larger grains found towards the midplane of the disk. They use the grain compositions of Pollack et al. (1994) and calculate the grain emissivity for each radius using Mie theory (Bohren & Huffman 1983). A vertical density distribution in hydrostatic equilibrium

$$\rho_g(z) = \frac{\Sigma_g}{\sqrt{2\pi}h_p} \exp\left(-\frac{z^2}{2h_p^2}\right) \quad (1.19)$$

and a power-law surface density distribution

$$\Sigma_g(R) = \Sigma_{g1} \left(\frac{R}{1AU}\right)^{-s} \quad (1.20)$$

$h_p$  is the pressure scale height of the disk given by  $c_s/\Omega_k$ .  $\Omega_k$  is the Keplerian angular velocity ( $\Omega_k = (GM_\odot/R^3)^{1/2}$ ) and  $c_s$  is the isothermal sound speed ( $c_s = [k_B T / (\mu m_u)]^{1/2}$ ), where  $G$ ,  $k_B$  and  $m_u$  are the gravitational constant, Boltzmann's constant and the atomic mass unit respectively. The disk temperature and mean molecular weight are  $T$  and  $\mu$  respectively with  $\mu = 2.34$ . The growth and settling of the dust is then numerically simulated using the basic method of Nakagawa et al. (1981). Here the statistical coagulation equation describing growth through collisions is solved along with an added vertical advection term to describe settling. The grain distribution for the velocity and height above the midplane that each sized grain can attain is calculated for a number of radial rings across the disk. The calculations are carried out over time steps to simulate the time evolution of the disk.

They find that from an initial grain size of  $0.1\mu\text{m}$  the dust grows rapidly so that the largest grains reach sizes of several hundred microns in a few thousand years. The larger grains settle to the midplane of the disk and form a layer with a layer of smaller grains above. After  $\sim 10^6$  yr only grains up to  $1\mu\text{m}$  remain in the upper layer. The larger grains of the midplane have considerably lower optical thickness than the smaller floating grains and so the small grains dominate. They find that the disk geometry responsible for self-shadowing described by Dullemond & Dominik (2004b) does not occur as the surface layer of the disk undergoing direct stellar irradiation descends more quickly due to added grain growth caused by Brownian motion depleting the micron-sized grains so keeping the flared geometry of the disk. They also find that the decrease in observed fluxes at millimetre and submillimetre wavelengths can be explained by grain growth and settling without depleting the disk in agreement with some of the above studies (figure 1.18). The rapid decrease in the optical depth of the inner disk region may also account for the inner holes or cleared regions reported in studies such as Calvet et al. (2002).

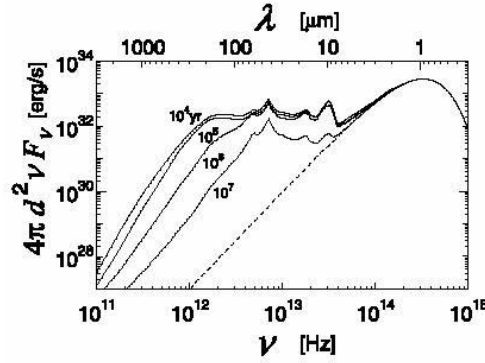


**Figure 1.18** Evolution of the SED of the standard disk. The dashed line represents the blackbody radiation from the central star. Grain growth and settling causes the energy fluxes from the disk to decrease with time, especially at long wavelengths of  $\lambda \geq 100\mu\text{m}$ . Taken from Tanaka et al. (2005).

A thorough investigation combining much of the above work has been carried out by D'Alessio et al (2006). In this study they adopt the two layered disk structure of Chiang et al. (2001) with a population of smaller, ISM like grains in the disk upper layer and larger grains in the midplane. They use the power law distribution of grain sizes from their earlier paper (D'Alessio et al. 2001) with grains from  $0.005\mu\text{m} - 0.025\mu\text{m}$  in the upper layer and  $0.005\mu\text{m} - 1\text{mm}$  in the midplane. They simulate the depletion of larger grains due to settling from the upper layer to the midplane by decreasing the dust to gas mass ratio in the upper layer and increasing it in the midplane. They find that dust settling impacts on the disk structure and SED in several different ways. The degree of dust settling effects the height of the disk photosphere and the degree of flaring present in the disk as discussed previously. This leads to a reduction in the fraction of stellar radiation being intercepted by the disk and so a reduction in the far – IR emission detected in SEDs and a reduction in the disk midplane temperature (impacting mm wavelengths) while that of the surface is independent of settling and varies with grain composition and size. They find that with even a very high degree of settling the disk maintains its flared structure and produces an SED with larger IR emission than a perfectly flat disk. Also, the observed silicate emission feature is present in all models with  $a_{\text{max}} < 10\mu\text{m}$  in the upper layer of the disk and its intensity increases as particle radius decreases as the smaller particles are hotter.

A review detailing much of the above by Dullemond et al. (2007) concludes that due to the ever increasing amount of spectral and spatial observational data available models will have to include much more detailed treatments of the physics of protostellar disk regions. Modifications to the dust distributions, grain types and growth mechanisms and

the geometry of the disk (to take account of nonaxial symmetric disks discussed by Fukagawa et al. 2004) will all need to be included. I have begun to explore some of these features in the studies detailed throughout this thesis and the models I have developed are well suited to further expansion over the coming years.

### **1.7 Outline of Thesis**

The aim and motivation of the research undertaken throughout this thesis has been the investigation of the observational signatures of various aspects of the evolutionary processes present in the Young Stellar Objects known as T Tauri stars and their accompanying protoplanetary circumstellar disks. Rather than confining my investigation to an individual aspect of these processes I have taken the versatility of the Monte Carlo technique described in the previous sections and through several modifications and extensions, described in the relevant chapters throughout this thesis, undertaken a study of the disk structure and constitution of both the disk at large and the changeable and dynamic inner disk regions.

In chapter 2 I describe how our code was modified to investigate, in a fully three dimensional manner, the effect of magnetically induced warped disk structure on the observed photopolarimetric variability of T Tauri disks, specifically AA Tau in the Taurus star forming region. A tilted stellar magnetic dipole of field strength similar in magnitude to other quoted values is shown to induce a warp in the inner regions of the circumstellar disk whose vertical and radial extent is capable of reproducing the observed variability of the source.

Throughout chapter 3 I investigate the effects of dust settling and grain segregation on the optical depth - structure and SED of the evolving protoplanetary disk system at large. This required modifying the Monte Carlo models so that any number of dust particle grain sizes can be incorporated. These grains can then be distributed throughout the disk in whatever vertical and radial distribution necessary to reproduce the observed SEDs of a number of sources observed with the SPITZER space telescope. These investigations have yielded information on the extent of settling and grain growth in the systems investigated and there are indications of ongoing clearing of the inner disk regions expected to occur during the formation of protoplanetary bodies in a number of sources investigated. This is an exciting and intriguing prediction and one which warrants future investigation through high resolution imaging.

Dynamical signatures of circumstellar disks are studied in chapter 4 with the development of a non-LTE radiation transfer code to investigate low mass and high mass disks using the CO molecules line emissions as a tracer for the dynamics of the disks. The non-LTE radiation transfer code used is based on that of Bernes (1979) but expanded to be fully three dimensional and adapted so that any disk structure or geometry, either analytical or imported from a hydrodynamic simulation, can be investigated. The applications of these developments are discussed in chapter 5 and allow us to investigate signatures of disk dynamics and spiral arm structure predicted by hydrodynamic simulations of massive disks studied by Qi et al. (2006), Rodríguez et al. (2005) and Raman et al. (2006). The ability to vary the disk structure and spatial resolution used in the simulations makes it possible to investigate in great detail the dynamics of circumstellar disks at different stages in their evolution which can be compared with observations to determine the physics behind the observational signatures. Dynamical models like those of Bonnell, Bate, Rice etc. that reproduce the observed structure can be incorporated. Properties of the dust distributions and grain types within those structures can then be investigated and compared with observed SEDs and spectral signatures in order to better understand the processes ongoing in these objects.

Throughout this thesis I have developed and extended 3D Monte Carlo Radiation Transfer techniques to investigate a broad range of processes that the evolving protoplanetary disks of T Tauri stars undergo throughout their life times. The versatility of the Monte Carlo technique and the way it has been applied in the fully three dimensional models described here mean that with only minor modifications it is possible to investigate the effects of any geometry, structure and constitution of the circumstellar environment on the spectral energy distributions, images, CO line profiles and channel maps that are of interest.

Some of the possible avenues of research and progression of the work described within this thesis are briefly discussed in chapter 6. The investigations and research carried out thus far are also summarised and reviewed in this chapter.

## **2. Modelling the Photopolarimetric Variability of AA Tau\***

### **2.1 Introduction**

A great many T Tauri stars are seen to exhibit varying degrees of photometric variability (Appenzeller & Mundt 1989; Bertout 1989). This is attributed, primarily, to the presence of hot and cool spots on the stellar surface of these young stars. Long lived cool spots are believed to be dominant in WTTS (Hatzes 1995) and short lived hot spots caused by the infall of accreting material from the surrounding circumstellar disk dominant in CTTS (Kenyon et al. 1994; Bouvier et al. 1993; Eaton, Herbst & Hillenbrand 1995; Choi & Herbst 1996; Herbst et al. 1994). Current theories predict that the stellar dipole magnetic field draws material up out of the circumstellar disk plane along the field lines and it is accreted onto the stellar surface near the poles in hot spots or rings (Mahdavi & Kenyon 1998), shown in figure 2.1 In this model the stellar dipole threads, truncates and possibly warps the inner region of the circumstellar disk.

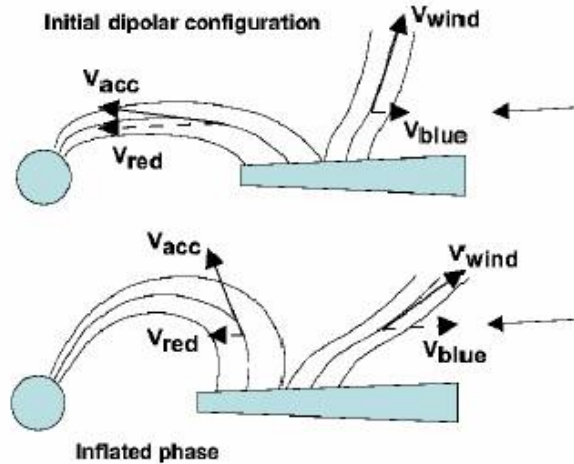


**Figure 2.1** Schematic diagram illustrating how the inner disk material is lifted out of the system's orbital plane by the stellar dipole magnetic field during the accretion process. Taken from Bouvier et al. (2003)

The magnetospheric accretion model has been applied to a number of sources to explain the observed photometric variability. These include the CTTS systems DR Tau (Kenyon et al. 1994) and the edge-on disk around HH30 IRS. In this latter system variability has been observed in both HST images (Burrows et al. 1996; Stapelfeldt et al. 1999; Cotera et al. 2001) and ground based VRI photometry (Wood et al. 2000). The variability of HH30 has been modelled as being due to hot spots on the stellar surface (Wood &

\*Paper Published: O'Sullivan, M., Truss, M., Walker, C., Wood, K., Matthews, O., Whitney, B. & Bjorkman, J.E., 2005, MNRAS, 358, 632



Whitney 1998; Wood et al, 2000) and as a warp in the inner regions of the disk (Stapelfeldt et al. 1999), no period has been determined so the true cause of these variations is still open to debate.

Photometric variability has recently been observed in the CTTS AA Tau (Bouvier et al. 1999, 2003) and has been shown to have a quasi-stable period of 8.2 days. This suggests that the variability is due to an object passing over the face of the central star and partially occulting it every 8.2 days rather than the more random variations in brightness produced by flaring events and hot spots formed by in-falling material. The prime candidate proposed for causing this variation is a warp in the inner disk material caused by optically thick material flowing up, out of the plane along magnetic field lines and occulting the star with a regular period. Every so often the variations seem to disappear completely and this is most probably due to non-steady accretion onto the star, either from fluctuations in the magnetic field or the material in the inner part of the disk being clumpy rather than uniformly distributed around the star.

In the rest of this chapter I will describe the observed photopolarimetric variations (section 2.2) and how existing Monte Carlo Radiation Transfer techniques simulate a warped disk that reproduces the observed photopolarimetric variability of the AA Tau system, constrain the large scale disk structure and the warping of the inner disk (section 2.3). In section 2.4 I will discuss the hydrodynamic simulations, carried out using a modified SPH code, used to probe the plausibility of our magnetically induced warped inner disk structure. Finally a summary of my results and conclusions is presented in section 2.5.

## 2.2 AA Tau's Photopolarimetry

The photopolarimetry of AA Tau has been reported in a number of studies. The young star at the heart of the system has been classified as a K7 dwarf (Kenyon & Hartmann 1995), with a mass of  $0.8M_{\odot}$ , radius of  $1.85R_{\odot}$  and an effective temperature  $4030 \pm 30\text{K}$  (Bouvier et al. 1999). From analysis of the photometric variability the system's disk, inferred from the IR excess emission (e.g., D'Alessio et al. 1999a), is estimated to be at an inclination of  $70^{\circ}$  or greater (Bouvier et al. 1999). The observed photometric variability is achromatic and is attributed to occultation of the star by a warp of the inner disk (Terquem & Papaloizou 2000; Bouvier et al. 2003). The occultation results in  $\Delta V \sim 1$  mag, has a duration of around 3 – 4 days and recurs every 8.2 days, but occasionally an occultation event is missing. Observations, shown in figure 2.2, show the overall

brightness level and depth of eclipse to be variable (Bouvier et al. 2003), suggestive of stochastic magnetospheric accretion in the AA Tau system. Assuming a Keplerian disk, the warp responsible for the periodic occultation must be located at 0.07AU.

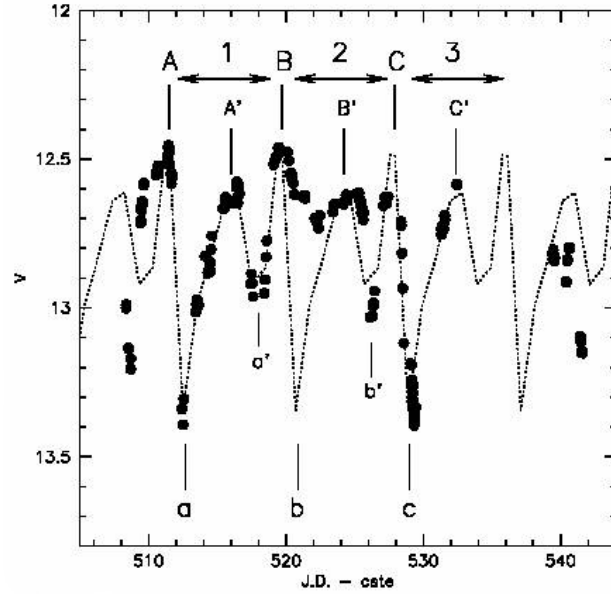


**Figure 2.2** The variable light curve of AA Tau (K – band) reproduced by a curve with a period of 8.2 days (dotted line). Taken from Bouvier et al. (2003), the letters refer to variations in flux levels discussed in that paper.

Polarimetry studies show that the linear polarization increases as the observed flux decreases and that the polarization has a range of 0.6% - 1.3% (Ménard et al. 2003), shown in figure 2.3. The polarization position angle is shown to vary from  $0^\circ$  to almost  $30^\circ$  (Bouvier et al. 1999) and studies of nearby stars exhibit similar large position angle variations. These large position angle variations are attributed to interstellar polarisation of around 0.5%, so the intrinsic polarisation is variable in the range  $\sim 0.1\%$  -  $0.8\%$  (Ménard et al. 2003).

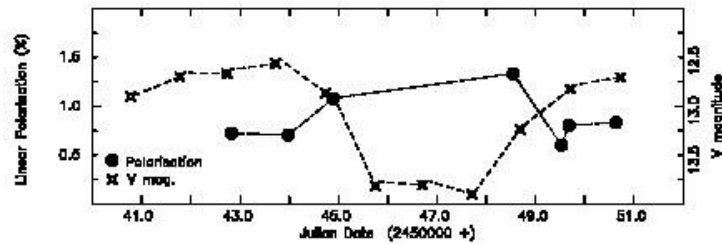


**Figure 2.3** Polarimetric and photometric variations of AA Tau as a function of time. The full circles and dotted line show the V - band linear polarisation of AA Tau as a function of Julian date. The open stars and dashed line show the V - band photometry as a function of Julian date. Taken from Ménard et al. (2003).

### 2.3 Radiation Transfer Models

In order to model the photopolarimetric variability of AA Tau I have used a suite of Monte Carlo scattered light and radiative equilibrium codes. For the SED models I use an axisymmetric disk to determine the disk shape and mass. The photometric modelling uses a non-axisymmetric warped inner disk described below.

As I model the time-dependant photopolarimetry with a warped disk, a fully self-consistent model should calculate the 3D time-dependant disk temperature, density structure and time-dependant SED. Such a calculation is beyond the scope of this investigation and so instead I present three separate models. The first models the SED of AA Tau with an axisymmetric disk. The disk structure is calculated by enforcing vertical hydrostatic equilibrium in the disk as described in Walker et al. (2004). In the second model, I model the photopolarimetry using an analytic description for warping of the inner disk and for the outer disk I use the HSEQ disk structure derived from the SED modelling. The height and shape of the warp derived in these analytical models is then used as a guide for the dynamical models of the interaction of a disk with a dipole stellar magnetic field. I present the resulting photopolarimetry from this model, again using the disk structure derived from the SED models of the outer disk.

#### 2.3.1 Disk Structure from SED Modelling

AA Tau's spectral energy distribution exhibits the large IR excess emission characteristic of a dusty protoplanetary disk. I have modelled the SED of this source with the Monte Carlo radiative equilibrium techniques developed by Bjorkman & Wood (2001), Wood et al. (2002b), Whitney et al. (2003) and updated to include an iterative loop to calculate the disk structure for an irradiated steady accretion disk in vertical hydrostatic equilibrium (HSEQ) by Walker et al. (2004). The model adopts the Shakura & Sunyaev (1973)  $\alpha$  – disk theory, similar to the approach described by D'Alessio et al. (1999a) to describe CTTS accretion disks. In this simulation I have used the dust opacity model that was successfully used to model the SEDs of the HH30 IRS and GM Aurigae disks by Wood et al. (2002a), Schneider et al. (2003) and Rice et al. (2003a). The wavelength dependence of this dust is shown in figure 2.4.

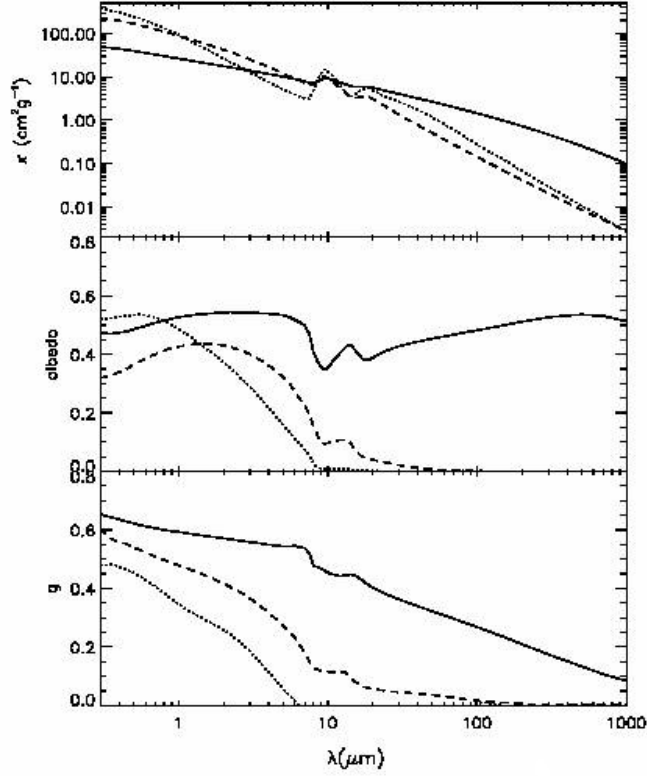


**Figure 2.4** Dust parameters for ISM grains (dotted lines), size distribution used by Cotera et al. (2001) (dashed lines), and the size distribution (model 1) used for – fitting the HH 30 SED (solid lines) by Wood et al. (2002a). Taken from Wood et al. (2002a).

The optical dust scattering properties (opacity,  $\kappa$ , albedo,  $a$ , phase function asymmetry parameter,  $g$ , and the maximum polarisation,  $P$ ) are shown in table 1. These parameters are incorporated into the scattered light models as described in Code & Whitney (1995).

	$K \text{ (cm}^2\text{g}^{-1}\text{)}$	$a$	$g$	$P \text{ (\%)}$
U	46.2	0.47	0.64	39.3
B	42.3	0.48	0.63	41.1
V	37.5	0.49	0.62	40.6
I	28.9	0.52	0.60	38.1

**Table 1.** Dust Properties

The iterative Monte Carlo HSEQ and radiative equilibrium code self-consistently calculates the disk density and temperature structure and emergent spectrum at a range of viewing angles. As mentioned in section 2.2 AA Tau’s inclination has been estimated at  $\sim 70^\circ$  and my simulations reproduced the AA Tau SED at this inclination with the following parameters  $T_* = 4000\text{K}$ ,  $R_\odot = 1.9R_\odot$ ,  $R_d = 150\text{AU}$  and with an accretion rate of  $7.5 \times 10^{-9} M_\odot\text{yr}^{-1}$ , corresponding to a total disk mass of  $M_d = 0.02M_\odot$ . The code

calculates an inner radius for the disk of  $7R_*$ , corresponding to the adopted dust destruction temperature of 1600K. The SED model and the observations of the AA Tau system are shown in figure 2.5, at viewing angles of  $i = 65^\circ$ ,  $68^\circ$  and  $71^\circ$ . The observational data is taken from the Kenyon & Hartmann (1995) compilation (squares) and ISO fluxes (triangles) from Chiang et al. (2001).

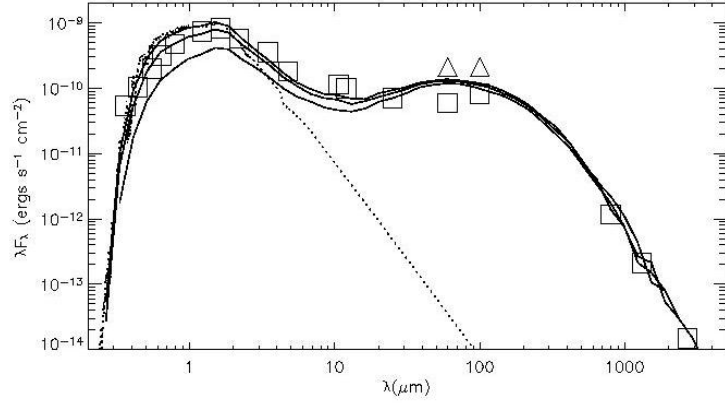


**Figure 2.5** SED data and model for AA Tau. The dotted line is the adopted stellar spectrum (from Kurucz 1994) and the three solid lines are the model SEDs for inclinations of (from top to bottom)  $65^\circ$ ,  $68^\circ$  and  $71^\circ$ . The different data points at 60 and  $100\mu\text{m}$  represent IRAS (squares) and ISO (triangles) observations.

For inclinations greater than  $i \sim 70^\circ$  the direct optical starlight becomes obscured by the flared disk. If the system inclination is indeed greater than  $70^\circ$  this could point to potential shortcomings in the models and that there is some form of dust settling in the outer parts of the disk that could reduce the disk scale height and allow the central star to be viewed at inclinations  $i > 75^\circ$  (e.g., Dullemond & Dominik 2004b). This situation will be investigated in more detail in chapter 3 (section 3.4.1) and will not be covered here as the point of this SED model is to obtain estimates of the disk mass and density structure based on a physically plausible disk model. This outer disk structure is then used in the scattered light models incorporating a warped inner disk to investigate the system's observed photopolarimetric variability.

### 2.3.2 Photopolarimetry Models & Analytical Disk Warping

The observed photopolarimetric variability of AA Tau has been interpreted as eclipses of the central star by a warp in the inner part of the circumstellar disk. To investigate this interpretation, I have constructed scattered light simulations where I introduce a

warp into the axisymmetric disk geometry derived from fitting the SED. The disk warp is created by introducing an azimuthal,  $\phi$ , dependence of the disk midplane,

$$z_0 = z_w \exp\left[-\frac{1}{2}\left[(\phi - \phi_0)/\Delta\phi\right]^2\right] \exp\left[-\frac{1}{2}\left[(\omega - \omega_0)/\Delta\omega\right]^2\right] \quad (2.1)$$

with  $Z_w$  the amplitude of the warp,  $\phi_0$  the azimuth of the warp and  $\Delta\phi$  the azimuthal extent of the warp. The warp is further constrained in radius with the second Gaussian function so that it peaks at  $\omega_0$  and extends over a radius  $\Delta\omega$ . A warp is created in both the positive and negative  $Z$  directions, with the peaks having a  $\pi$  phase separation. A second warp in the negative  $Z$  direction does not alter the simulated light curves for this viewing angle. Figure 2.6 shows the warp in the inner regions of the disk on the positive  $Z$  surface responsible for the photopolarimetric variability.

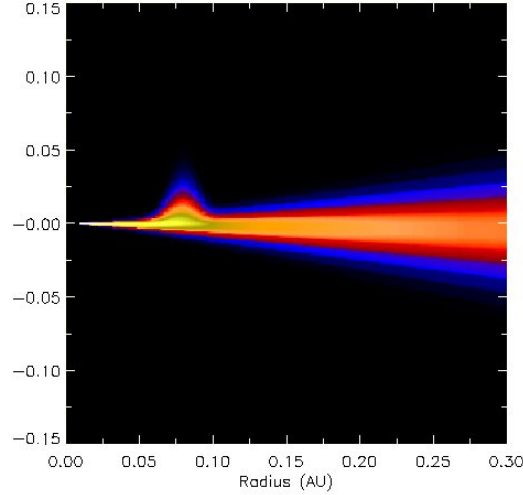


**Figure 2.6** Analytically induced warp used to fit the photopolarimetric variability of AA Tau. The figure shows a slice through the disk density at azimuthal angle  $\phi = 0^\circ$ , showing the peak amplitude of the inner disk warp.

The parameterised inner disk warp simulation that best reproduces the observed photopolarimetry has  $i = 75^\circ$ ,  $Z_w = 0.016$ ,  $\Delta\phi = 75^\circ$ ,  $\omega_0 = 0.072\text{AU}$ ,  $\Delta\omega = 0.0084\text{AU}$ . Figure 2.7 shows the photopolarimetric light curves for this model. Note that the photopolarimetric variability for a warped disk is achromatic, as observed. Even though there is a wavelength dependency on the circumstellar dust opacity, the disk warp is optically thick enough that colour variations in the photometry are not observable. Slight wavelength dependent variations are present in the level of polarisation. In the observed polarimetry of AA Tau (Bouvier et al. 1999), there is a substantial position

angle variation of around  $0^\circ$  to  $30^\circ$ . By comparison with other stars in the vicinity, a study by Ménard et al. (2003) attributed the variation to the interstellar medium (ISM). After ISM polarisation is removed, we find the change in position angle,  $\Delta PA$ , drops to  $0^\circ$ . In my simulations, I find  $\Delta PA \sim 4^\circ$  indicating that there is in fact some intrinsic  $\Delta PA$ . If this is the case then it is not unreasonable to assume that the interstellar polarisation is  $< 0.5\%$ . The removal of a smaller interstellar polarisation component would in turn produce a slightly higher linear polarisation value for AA Tau, somewhere between the value stated by Bouvier et al. (1999) and Ménard et al. (2003) mentioned earlier.

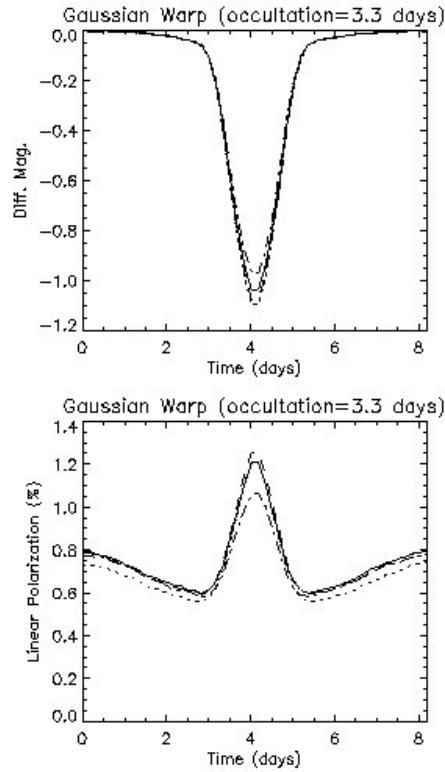


**Figure 2.7** Photopolarimetric simulations of a Gaussian shaped warp with an occultation duration of 3.3 days. The upper panel shows the variation in observed flux with  $\Delta m \sim 1$ , for U (dotted), B (dashed), V (solid) and I (dot-dashed) bands. The lower panel shows the corresponding linear polarisation with  $P = 0.4 - 1.05\%$  in the V band.

Clearly many different warped disk models could match the observations and so the parameters have been constrained as follows. The direct stellar flux and polarisation from a flared disk are sensitive to the inclination angle (e.g. Whitney & Hartmann 1992). For viewing angles  $i > 78^\circ$ , the radiation from the central star becomes blocked by the flared disk and the polarisation increases dramatically (e.g. see Stassun & Wood 1999; Figure 5) because the relative fraction of scattered to direct starlight increases.

For viewing angles  $i < 70^\circ$ , we obtain very low polarisation values and would require very large warps,  $Z_w$ , to obtain the observed photometric variability. We do not allow warps to exceed  $Z_w / \omega_0 = 0.3$  in accordance with theoretical models of disk warping (Bouvier et al. 1999). The warp must be constrained to a fairly narrow range in disk radius to obtain the observed variability. Warps extending over large radial distances would not survive due to differential rotation in the disk. The shape of the photopolarimetry light curve allows us to place constraints on the azimuthal extent of the warp. As the occultation itself is reported to last from 3 – 4 days, it implies a warp with an azimuthal extent of  $130^\circ - 175^\circ$ . The warp shown in figure 2.8 matches the observed brightness variation and polarisation of AA Tau. We find that as we increase the extent of the warp around the disk there is very little change in the brightness variation but there is a reduction in the level of polarisation reached during the occultation. Values of  $\Delta\Phi$  much larger or smaller than those used here result in light curves that show too broad or too narrow an eclipse feature.

For comparison, modelling was carried out using a sinusoidal shaped warp. The duration of the warp was 3.3 days and there was very little change in the photopolarimetry compared to our previous model. For the sinusoidal warp,  $\Delta V = 1.08$  showing good agreement with the Gaussian model ( $\Delta V = 1.05$ ) and the polarisation varied from 0.4 – 1.15% also in good agreement with the Gaussian model where polarisation varied from 0.6 – 1.2%.

Finally I modelled the photopolarimetry of the magnetically induced warp of the dynamical models. After the original interpretation that the variability of AA Tau was the result of a warped inner disk (Bouvier et al. 1999), a study by Terquem & Papaloizou (2000) examined the conditions under which an inclined stellar magnetic dipole could reproduce the required warp. They found that a dipole inclined at  $30^\circ$  is easily capable of inducing a warp of the size proposed by Bouvier et al. (1999). They also discovered that depending on the viscosity of the disk, the vertical displacement varied rapidly (low viscosity) and was likely to cause break-up or caused a smoothly varying warp of the kind expected (high viscosity). Both cases would produce variations in light curves that could possibly be distinguished from one another.

A stellar magnetic dipole of 5.2kG inclined at  $30^\circ$  to the stellar rotation axis produced a warp of approximately the same dimensions as the analytical model but has a larger radial extent. The radial extent of the warp makes little difference once it is large enough to fully obscure the central source, so this makes no difference to the



photopolarimetry of the model. Figure 2.8 shows the dynamically induced warp in the inner regions of the disk patched on to the flared outer regions of the analytical disk model.

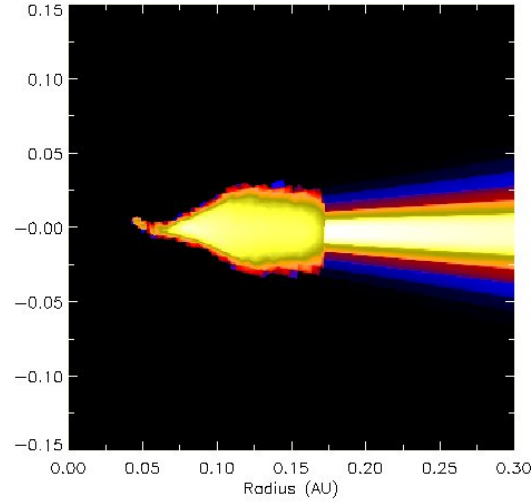


**Figure 2.8** Dynamically induced warp used to fit the photopolarimetric variability of AA Tau. The figure shows a slice through the disk density, showing the peak amplitude of the disk warp.

The duration of the occultation event was around 3.3 days with some low level variability lasting slightly longer. The warp produced a variation in photometry,  $\Delta V$ , of 0.73mag. The polarisation was found to vary from 0.3 – 0.6% giving good agreement with the analytical model and the observed variability. Figure 2.9 shows the photometric light curves for this model at various wavelengths.

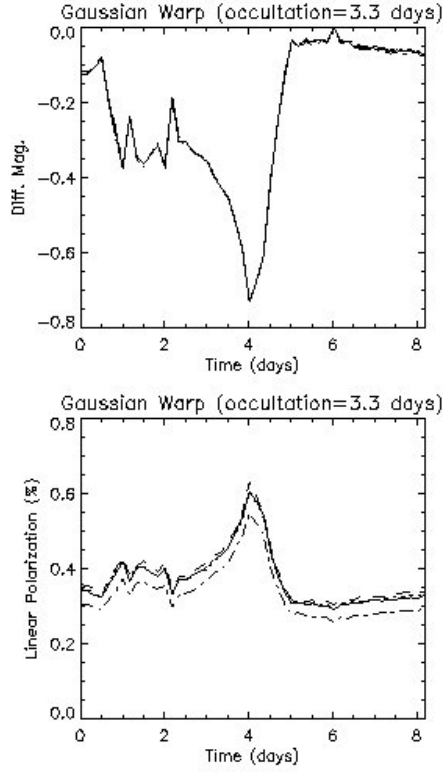


**Figure 2.9** Photometry simulations of the dynamically induced warp with an occultation duration of  $\sim 3$  days. The upper panel shows the variation in observed flux, with  $\Delta m \sim 0.73\text{mag}$ , for U (dotted), B (dashed), V (solid) and I (dot-dashed) bands. The lower panel shows the corresponding linear polarisation with  $P = 0.6 - 0.8\%$  in the V band.

In summary, I have been able to reproduce the observed photopolarimetric variability of AA Tau using the periodic occultation of the central star by a magnetically induced warped inner disk. I estimate the uncertainty in my model parameters to be  $i = 75^\circ \pm 2^\circ$ ,  $\Delta\phi = 75^\circ \pm 5^\circ$ ,  $\Delta\omega = 0.0084 \pm 0.0042$  au and  $Z_w = 0.016 \pm 0.0016$  au.

### 2.3.3 Time Sequence Scattered Light Images

In addition to eclipsing the star and producing the observed photopolarimetric variability, the warp also casts a shadow over the outer regions of the disk. Therefore, a time sequence of high spatial resolution images may detect a shadow sweeping round the disk. Figure 2.10 shows a sequence of scattered light images at a range of viewing angles for my AA Tau warped disk model. Figure 2.11 shows a series of close-up scattered light images of the warp occulting the star at a viewing angle of  $75^\circ$ .

These models may be compared with hot star spot models (Wood & Whitney 1998), which show a lighthouse effect of a bright pattern sweeping around the disk.

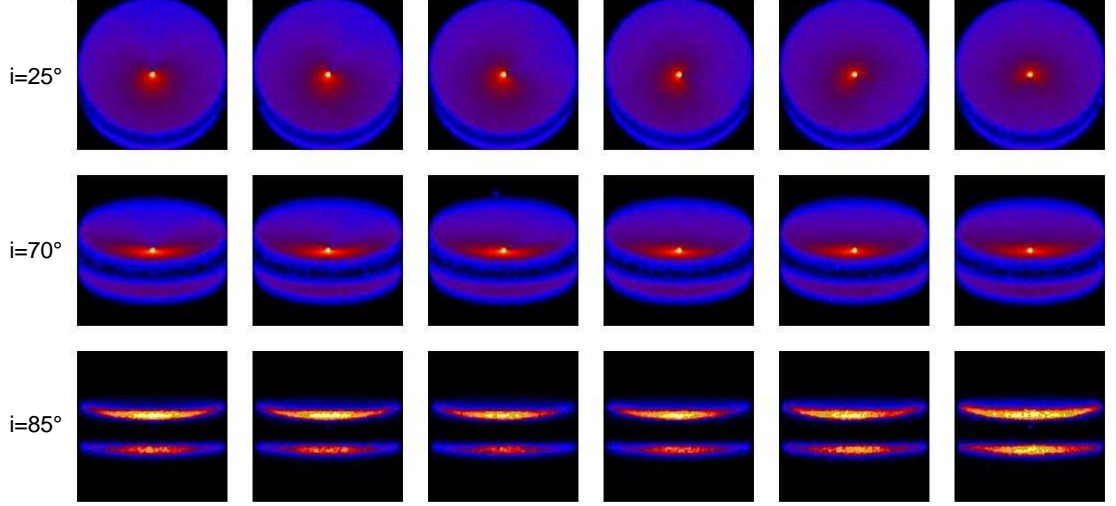


**Figure 2.10** Scattered light images of our warped disk model of AA Tau. The panels on the upper row show the disk at an inclination of  $25^\circ$ , the centre row of panels have inclination  $70^\circ$  and the panels along the bottom show an inclination of  $85^\circ$ , all are 400AU on a side. The images cover half a rotation and clearly show the shadowed area caused by the warp occulting the star and moving round the disk. To overcome the large dynamic range between the starlight and the scattered light in the disk, the images are presented on a one-tenth root (square root for the edge-on disk) stretch. The faintest regions have a surface brightness of  $10^{-6}$  that of the star.

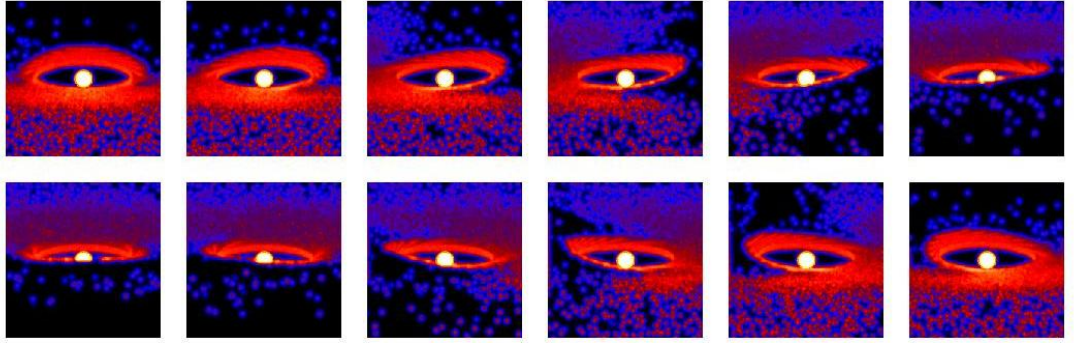


**Figure 2.11** Scattered light images of the warped disk inclined at  $75^\circ$  and with an image diameter of 0.2AU clearly showing the material responsible for the photopolarimetric variations occulting the star. To overcome the large dynamic range between starlight and scattered light in the disk, the images are again presented on a one-tenth root stretch. The faintest regions have a surface brightness of  $10^{-6}$  that of the star.

For some warped disk models, the azimuthal extent of the warp may mimic scattered light images that are the result of hot star spots, but multi-wavelength photometry can discriminate models: star spots yield chromatic variability, whereas a disk warp yields achromatic photometric variability. Notice that for edge-on viewing the time sequence images for warped disks and disks illuminated by a spotted star (Wood & Whitney 1998)

are very similar, and multi-wavelength photometry is required to distinguish between the two scenarios.

For completeness, I included spots of various sizes located at a range of latitudes with a temperature of 8000K in my warped disk models. I found that a spot with an angular radius of  $5^\circ$  was more than enough to visibly alter the photometry at all latitudes causing the wavelength dependant effects mentioned above. Figure 2.12 shows the unresolved photopolarimetric models of the warped disk illuminated by a star with hotspots on its surface. The spotted star model exhibits strong colour changes not present in the warped disk model. The shape of both the photometric variation and polarimetric variation curves are also quite different for the spot model purely as a function of the differing geometries involved. These strong colour variations are not reported in AA Tau, however, the HH30 IRS disk does exhibit colour dependence (Wood et al. 2000), so it appears that the hotspot models are more appropriate for that system.

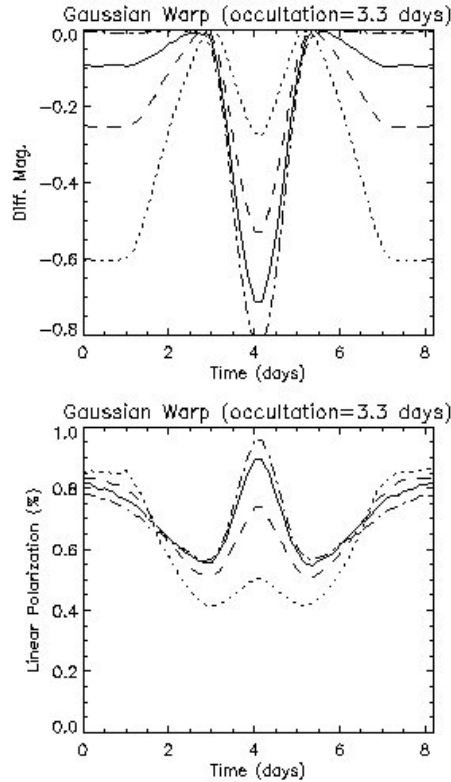


**Figure 2.12** Variations in photometry (top panel) and polarisation (bottom panel) for our warped disk illuminated by a spotted star at four different pass-bands: U (dotted), B (dashed), V (solid) and I (dot-dashed). The hotspot is at the same longitude as the warp, is at a latitude of  $65^\circ$ , has a radius of  $5^\circ$  and has a temperature of 8000K. Note the strong wavelength dependence and different shape of the light curve to that generated by a warped disk geometry.

## 2.4 Hydrodynamic Simulations

Having analytically investigated the size and shape of the inner disk warping required to match the photopolarimetry of AA Tau, a 3D hydrodynamics code was then used to explore the magnetically induced structure in the disk. With the help of Mike Truss and his 3D SPH code the inner accretion disk region of AA Tau was modelled. SPH is a LaGrangian numerical scheme in which gas flow is represented by a system of particles moving with the local fluid velocity (Monaghan 1992). The SPH method has been applied successfully to accretion disks in a host of astrophysical situations including protoplanetary disks (Rice et al. 2003a), cataclysmic variables (Truss et al. 2000) and micro-quasars (Truss & Wynn 2004) and has been applied to the magnetic warping of disks by Murray et al. (2002). The warping of a disk in response to an offset dipolar field has also been calculated with a 3D Eulerian magnetohydrodynamics code by Romanova et al. (2003).

In our model, we use operator splitting to solve for the dynamics of the gas flow subject to three forces. The gas pressure force is computed by solving the SPH momentum equation with the standard SPH viscosity term:

$$\frac{dv_i}{dt} = -\sum_j m_j \left( \frac{P_i}{\rho_i^2} + \frac{P_j}{\rho_j^2} + \frac{\beta \mu_{ij}^2 - \alpha \bar{c}_{ij} \mu_{ij}}{\rho_{ij}} \right) \nabla_i W_{ij} \quad (2.2)$$

Here,  $W_{ij}$  is the interpolating kernel between particles  $i$  and  $j$ ,  $\bar{c}_{ij}$  is the mean sound speed of the two particles and  $\mu_{ij}$  is such that

$$\mu_{ij} = \begin{cases} \frac{H \mathbf{v}_{ij} \cdot \mathbf{r}_{ij}}{r_{ij}^2 + 0.01h^2} & \mathbf{v}_{ij} \cdot \mathbf{r}_{ij} \leq 0 \\ 0 & \mathbf{v}_{ij} \cdot \mathbf{r}_{ij} > 0 \end{cases} \quad (2.3)$$

where  $h$  is the smoothing length and  $H$  is the local scale height of the disk. The viscosity parameter  $\alpha$ , should not be confused with the Shakura – Sunyaev viscosity parameter, although Murray (1996) has shown that in three dimensions with  $\beta = 0$ , the net Shakura – Sunyaev viscosity introduced by this model is

$$\alpha = \frac{1}{10} \alpha_{SPH} \quad (2.4)$$

The gravitational attraction of the star is computed via a simple Runge – Kutta fourth-order integrator. The disk self-gravity is ignored here as we are only concerned with a

small, low-mass region near the central star. Full MHD is not yet possible with SPH, so a third force is added, representing the drag on each particle as a result of the magnetic dipole field anchored on the star. The dipole field is assumed to co-rotate with the star, but is offset slightly from the rotational axis.

The magnetic drag force model has been described by Wynn, King & Horne (1997) and was first included in an SPH scheme by Murray et al. (2002) to investigate the magnetic warping of disks in cataclysmic variables. The model has been developed further in a recent paper by Matthews, Speith & Wynn (2004), in which it is used in a 1D model of accretion disks in T Tauri stars. Here we incorporate these developments into a fully 3D hydrodynamic study of a circumstellar disk. In the model, the magnetic tension force appears as

$$a_{mag} \sim \frac{B_z^2}{4\pi\rho r_c} \left( \frac{\Omega - \Omega_*}{\Omega} \right) \quad (2.5)$$

where  $\Omega$  and  $\Omega_*$  are the angular velocities of the gas and the star respectively and  $r_c$  is the local radius of curvature of the magnetic field lines. This is approximated as a fraction of the local scale height of the disk,

$$r_c = \zeta H \quad (2.6)$$

where  $\zeta \leq 1$  (Pearson, Wynn & King 1997).

For a dipole of magnetic moment  $\mu$ , we have

$$B_z = \frac{\mu}{r^3} \quad (2.7)$$

The drag force acts in a direction perpendicular to the relative velocity of the gas and the rotating field. It is positive, repelling material away from the star, for all radii  $r > R_{co}$ , where  $R_{co}$  is the co-rotation radius. Conversely, gas at radii  $r < R_{co}$  feels a net force towards the star. The functional form of this force term is plotted in figure 2.13. For numerical convenience we only model the flow of gas outside a radius  $R_{min} = 4R_*$ , because close to the star the magnetic drag force becomes very large. This has no impact whatsoever on the resolution of the structure in the accretion disk itself which is truncated well outside this radius.

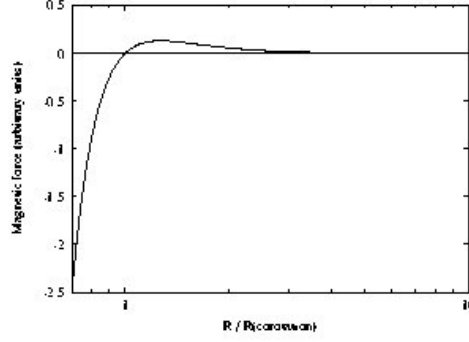


**Figure 2.13** The radial dependence of the magnitude of the magnetic drag acceleration term, plotted here for a surface density profile  $\Sigma \sim \rho H \propto 1/r$ . In the simulations the surface density is calculated self-consistently, but in practice departures from this are small. The net drag force is directed towards the central star inside the co-rotation radius and its magnitude increases sharply towards the star. Outside the co-rotation radius the net drag force is weaker and is directed away from the central star. The drag force is zero at  $R = R_{\text{co}}$ .

We set up an initial disk comprising 500,000 SPH particles, extending from the co-rotation radius  $R_{\text{co}} = 8.7R_*$  to  $20R_*$ , where the stellar radius is taken to be  $R_* = 1.87R_\odot$ . The midplane of the initial disk is co-planar with the stellar equator and has a surface density profile  $\Sigma(r) \propto r^{-1}$ . It is flared with a hydrostatic vertical density profile  $\rho(z) = \rho(0)\exp(-z^2/2H^2)$ , where  $\rho(0)$  is the density in the midplane and  $H$  is the scale height  $c_s/\Omega$ . The particles are given velocities so that the mass accretion rate is at a constant value of  $\dot{M} = 7.5 \times 10^{-9} M_\odot \text{yr}^{-1}$  throughout the disk. A constant mass accretion rate has been investigated here and it is quite possible that any variations in this mass transfer would have an effect on the size and shape of the warp in the disk. This scenario is discussed in a recent paper by Pfeiffer & Lai (2004). Another factor which may affect the long term behaviour of the warp structure is the magnetic diffusivity, although it remains unclear as to how important an effect it is. This was beyond the scope of this investigation and has not been considered here.

A Shakura – Sunyaev viscosity parameter of  $\alpha = 0.01$ ,  $\beta = 0$  and a dipole moment  $\mu = 1.2 \times 10^{37} \text{Gcm}^3$  was used to simulate the disk. With  $\zeta = 1$  the stellar magnetic field strength corresponds to  $B(R_*) = 5.2 \text{kG}$  which is slightly larger than the usual range quoted for T Tauri stars of  $2 - 3 \text{kG}$ . A field of this size was necessary to produce the warp required by the observations but there is nothing to prevent  $\zeta < 1$ , which would bring the field strengths required down in line with the observed field strengths.

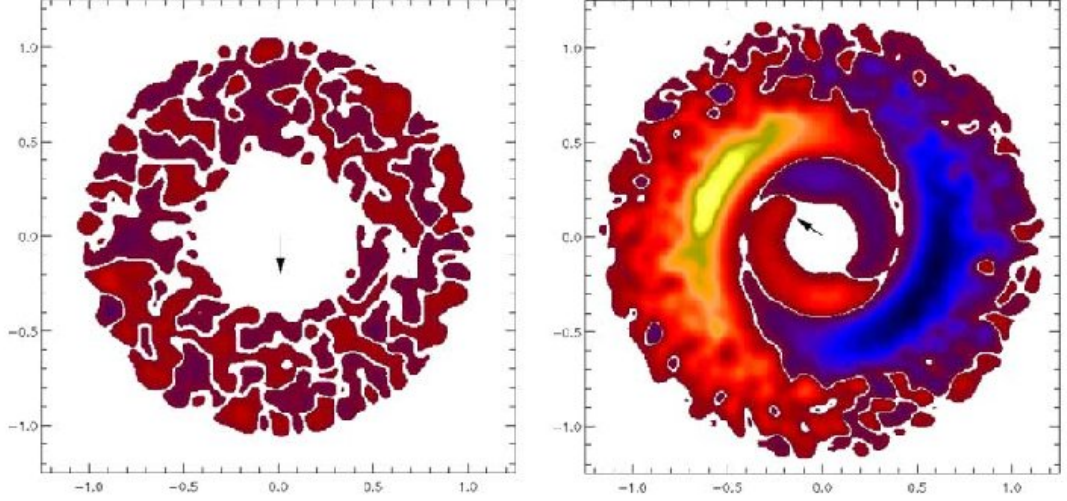


**Figure 2.14** These images of the accretion disk viewed from directly above the star are coloured according to the mean height above the midplane at the beginning (left) and end (right) of the simulation. Blue regions are, on average, below the midplane, while yellow and orange are, on average, above the midplane. Regions that remain co-planar with the stellar equator are left white. The initial conditions (left) are chosen such that the altitude of the gas at each radius is symmetric about the midplane; hence the mean height appears random (but is very close to zero). The axes are scaled in the units of  $20R_*$ . Gas that appears inside the co-rotation radius (which lies near 0.45 in these units) is threaded on to the magnetic field lines of the stellar dipole field. The black arrows at the centre of the disk show the projected direction of the north pole of the dipole, which is inclined at an angle of  $30^\circ$  to the vertical.

After several orbits under the influence of the magnetic field a stable warped structure develops near the co-rotation radius. Figure 2.14 shows the local average height of the disk above the midplane in the initial and final states. The warp has a maximum vertical height of  $\sim 2R_*$ . This result is consistent with the earlier analyses of Terquem & Papaloizou (2000) who computed the steady warped structure of the disk in AA Tau and predicted a similar trailing spiral structure near the co-rotation radius. We investigated the effect of altering the tilt angle of the magnetic dipole field and found that increasing the tilt angle to  $50^\circ$  had little or no effect on the resultant warp structure and the photometry produced was indistinguishable from that obtained in the original simulation.

## 2.5 Conclusion

Having modelled the photopolarimetric variations of the classical T Tauri system, AA Tau, I have shown that a magnetospherically induced warp of the accretion disk at roughly the stellar co-rotation radius occults the star and reproduces the observed



variability. My SED modelling provides estimates of the disk mass and large-scale density structure that are subsequently incorporated in my non-axisymmetric scattered light disk models. Spotted star models exhibit a strong wavelength dependence which is not observed in the AA Tau system. My warped disk model shows no wavelength dependence and can reproduce the occultation period and duration with the required brightness and polarisation variations. A feature of the warped disk model is that it produces a shadow that sweeps round the outer disk and this may be detectable with high spatial resolution time sequence imaging. The shadowing of different parts of the disk's outer regions is not expected to affect the simulated photometric variability by altering the 3D disk structure. The photometric variations are primarily produced by occultations of the central star and the contribution from scattered light in the outer disk is small. However the shape of the outer disk may be important for accurately modelling the polarimetric variability as it is produced by the scattering of starlight. The disk's vertical structure will be investigated in more detail in later chapters.

The stellar magnetic dipole was found to require a field-strength of 5.2kG and an inclination of  $30^\circ$  to the rotation axis to generate a warp of the size and shape needed to reproduce the observed variations by the use of a modified SPH code. The models presented here are periodic so do not reproduce the stochastic variations in the light curve of AA Tau (Bouvier et al. 2003). However our models do show that disk warping resulting from the interaction of the stellar magnetic field with the disk can reproduce the amplitude and the shape of the occultation events. In the near future it should be possible to make accurate measurements of the magnetic field structures of T Tauri stars using Zeeman Doppler imaging (Petit & Donati 2004), allowing more realistic modelling of the stellar magnetic field and its impact on the surrounding accretion disk.

### **3. Dust Settling & Grain Growth**

#### **3.1 Introduction**

With the ever increasing wealth of data on T Tauri systems it has become apparent that models consisting of multiple grain species are required to model high resolution IR spectra, essential if observations are to be reproduced. Chapter 1.6.1 detailed some of the recent studies incorporating multiple dust species in models and the observed spectral features that have highlighted the need for such investigations.

In the sub – mm region of spectrum the slope of the SED from many CTTS is too steep to be reproduced by disks consisting only of ISM grains (Beckwith et al. 1990, Beckwith & Sargent, 1991). D’Alessio et al. (1999a & 1999b) found disks in hydrostatic equilibrium and consisting of only ISM grains produced too much IR emission. A further problem with the thick disks is that they lead to too large a fraction of T Tauri stars being obscured to match the numbers of observed sources. D’Alessio et al. (1999b) also note that in order to reproduce the strength of the silicate feature observed at around 10 $\mu$ m, some combination of ISM and larger grains is required.

All of this provides the motivation for undertaking the development of a fully 3D, multiple dust species Monte Carlo radiation transfer model. The first step of which is the development of a two layer model with grains of different sizes in each layer like that of Chiang et al. (2001) and Furlan et al. (2005). In the following sections I describe the development of a model similar to these but not restricted to sharp, delineated layers of one particular type of grain. Instead the scale height of each grain type can be varied so that their vertical extent varies gradually and simulates a mix of grains. An exploration of the effects of varying different parameters of the model on the SED is carried out before applying it to a number of sources recently observed with the SPITZER space telescope.

#### **3.2 Fully 3D, Multiple Dust Species Code Development**

The model SEDs that we compute are, generally, for passive disks (although accretion luminosity generated in the inner disk can also be considered) with a flared density structure like that of Shakura & Sunyaev (1973), described in section 1.6.1 and given by equation (1.19). The temperature structure and emergent SED are then calculated using the Monte Carlo radiative equilibrium technique of Bjorkman & Wood (2001). In the investigation the above density structure is calculated for each dust grain type to be

included in the investigation and each is assigned a mass fraction of the total disk mass. The base density,  $\rho_0$ , is then:

$$\rho_0 = (\beta + 2 - \alpha) n M_{\text{disk}} / 2\pi^{1.5} h_0 R_*^3 \quad (3.1)$$

where  $n$  is the fraction of the total disk mass attributed to each dust type, the disk mass and stellar radius are in solar units and  $\alpha$  and  $\beta$  are 2.25 and 1.25 respectively, typical values for irradiated accretion disks (D'Alessio et al. 1999a). The  $\alpha$  and  $\beta$  parameters control the rate at which the density falls off with the radius and the vertical extent of the flaring, respectively, shown in equation (3.2). D'Alessio et al. (1999a) showed that irradiated accretion disks in general have surface densities varying as  $\omega^{-1}$ , so  $\beta - \alpha$  must always equal -1.

$$\Sigma \propto \omega^{\beta-\alpha} \quad (3.2)$$

The surface density is the integral of the density (equation 1.19) with respect to  $z$ , the vertical height above or below the disk midplane.

Each dust type is also given a different initial scale-height,  $h_0$ , so the vertical distribution and mass contribution to the disk of each type of dust can be tailored to give any combination and a huge range of disk structure and constitutions to study. It is also possible to introduce regions where there are only a few dust types or even none at all. This is particularly useful in simulating proposed cleared inner regions of disks or regions where high temperatures destroy grains (typically above 1600K, Lada & Adams 1992 and Isella et al. 2006). This in turn means that the density, mass and dust temperature arrays are now not only dependant on cell location in the simulation but also on dust type.

As photons are tracked through the simulation using the MCRT technique, described in chapter 1.5, and in the case of this simulation incorporating multiple dust species the opacity encountered by the photon is the total opacity contributed by all dust species in all the cells the photon passes through. Once an interaction point is reached it is important to establish which dust species the photon is interacting with in the cell so that the correct optical properties can be used to determine the new temperature in the cell and insure that the correct energy distribution is output. The probability of interacting with a specific dust is dependent on the density of that dust in the cell and its opacity. The probability of interacting with dust type  $i$  is:

$$P_i = \rho_i \kappa_i / \sum \rho_n \kappa_n$$

where  $\rho$  and  $\kappa$  are the density and opacity respectively and the subscripts denote which of  $n$  dust types is being considered. A random number generator is then used to select which dust type will interact with the photon packet so that it is not necessarily the most abundant dust type in the cell that will interact with the photon. If the random number is less than  $P_1$  then dust one is selected, if the number is less than  $P_1+P_2$  then interact with dust 2 and so on for  $n$  dust types.

### 3.2.1 Dust Grains

As described above, the program can use the optical properties of any number of dust grain sizes or the mean properties of any number of grain size distributions to simulate the environments of YSOs. Most of my work has focused on using distributions of different sized grains rather than several individual grain sizes. To represent the small grains found in the ISM I have used opacity and scattering properties of Mathis, Rumpl & Nordsieck (1977) who used a power law distribution with a particle size range of  $0.005\mu\text{m} - 0.25\mu\text{m}$ , given by

$$n(a) = n_0 a^{-p} \quad (3.3)$$

Where  $a$  is the grain radius,  $n_0$  is a normalisation constant and the exponent  $p$  is a free parameter which was set to 3.5, referred to as ISM grains throughout. The resulting opacity reproduces the observed extinction in the diffuse ISM of the Galaxy. Larger grains are represented by a power law distribution with an exponential cut off described by Wood et al. (2002a) and shown in section 1.6.1, equation (1.18), this size distribution will be referred to as W02 grains throughout.

As expected these two distributions have very different optical properties (figure 3.1) and it is these differences that lead to the variety of SEDs one can generate by varying the abundances and locations of these dust species. The combination of these grain size distributions gives a shallower sloping opacity across the spectrum and reduces the size of the silicate feature when compared to ISM grains alone.

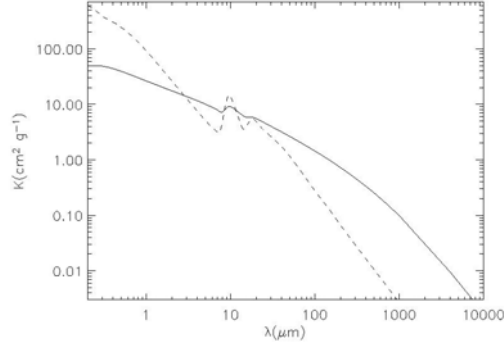


**Figure 3.1** Comparison of dust species opacities, the dashed line is the smaller ISM distribution and the solid line is the W02 distribution.

### 3.3 Exploring the Effects of Multiple Dust Species

Before applying the multiple dust species model to specific sources (section 3.4) I conducted an exploration of the effects of the different scale-heights and mass fractions of a multi-species disk structure on the simulated SED. To illustrate these I have run models based on a typical T Tauri disk consisting of varying amounts of the different dust species at different scale heights in the disk. I used a passive flared disk with a density structure like that of Shakura & Sunyaev (1973) described in section 3.2 and the parameters shown in table 2. For comparison, the modelled systems of GM Aur (Schneider et al. 2003) and HH30 (Wood et al. 2002) use disk scale heights at 100AU of 10 and 15AU respectively.

$M_*(M_\odot)$	$R_*(R_\odot)$	$T_*(K)$	$M_d(M_\odot)$	$R_d(AU)$	$h_0(R_*)$	$h_{(1AU)}(AU)$	$h_{(100AU)}(AU)$	$\alpha$	$\beta$
0.6	1	4000	0.01	200	0.008	0.03	9.68	1.25	2.25

**Table 2.** Shows the disk parameters used in the general investigation into the effect of different grain size distributions on the SED.

The model disk was given an inclination of  $45^\circ$  and at first consisted entirely of the W02 grain distribution. This dust species was given a scale height of  $h_{100} = 9.68AU$  (at  $R = 100AU$ ) above the disk midplane, represented by the dot-dashed curve in figures 3.2, 3.3 and 3.4. A smaller dust species consisting of the MRN distribution (Mathis, Rumpl & Nordsieck 1977) was then added in a range of mass fractions and scale-heights and the resultant SEDs compared with the single grain SED. The  $\alpha$  and  $\beta$  parameters shown in table 2. were used throughout this investigation, i.e.  $\Sigma \propto r^{-1}$ .

Small Grains (MRN)				Large Grains (W02)			
Mass Frac.	$h_0$	$h_{(1\text{AU})}$	$h_{(100\text{AU})}$	Mass Frac.	$h_0(R_*)$	$h_{(1\text{AU})}(\text{AU})$	$h_{(100\text{AU})}(\text{AU})$
1%	0.008	0.03	9.68	100%	0.008	0.03	9.68
1%	0.012	0.046	14.53	100%	0.008	0.03	9.68
1%	0.016	0.061	19.37	100%	0.008	0.03	9.68

**Table 3.** Shows the grain parameters used to generate the SEDs of figure 3.2.

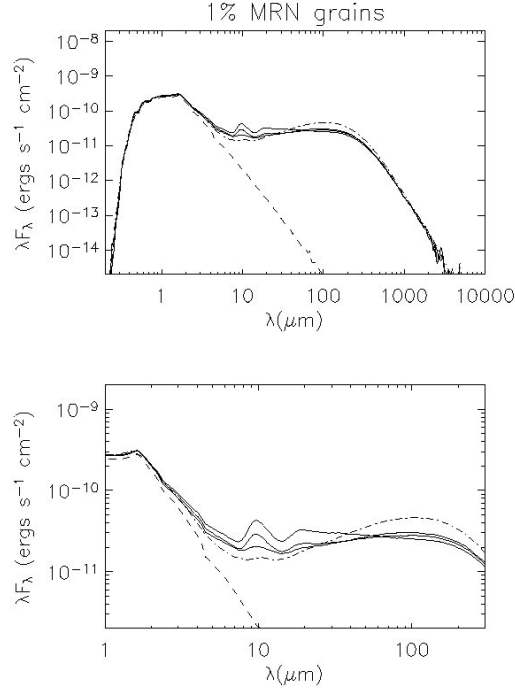


**Figure 3.2** SEDs generated with 1% MRN grains (solid lines) with the MRN grains at three different scale heights (lower line  $h_{100} = 9.68$ , middle line  $h_{100} = 14.53$  and upper line  $h_{100} = 19.37$ , all AU). SED of the disk composed of W02 grains only shown for comparison (dot-dashed line).

Figure 3.2 shows the SEDs generated with an extra 1% of the disk mass added in the form of the smaller MRN grains. While figure 3.3 shows the SEDs with an extra 5% and figure 3.4 an extra 15%. The MRN grains were assigned scale heights of 1, 1.5 and 2 times the scale height of the W02 grains making up the vast majority of the disk. Tables 3, 4 and 5 summarise the parameters of the models displayed in figures 3.2, 3.3 and 3.4 respectively.

Small Grains (MRN)				Large Grains (W02)			
Mass Frac.	$h_0$	$h_{(1\text{AU})}$	$h_{(100\text{AU})}$	Mass Frac.	$h_0(R_*)$	$h_{(1\text{AU})}(\text{AU})$	$h_{(100\text{AU})}(\text{AU})$
5%	0.008	0.03	9.68	100%	0.008	0.03	9.68
5%	0.012	0.046	14.53	100%	0.008	0.03	9.68
5%	0.016	0.061	19.37	100%	0.008	0.03	9.68

**Table 4.** Shows the grain parameters used to generate the SEDs of figure 3.3.

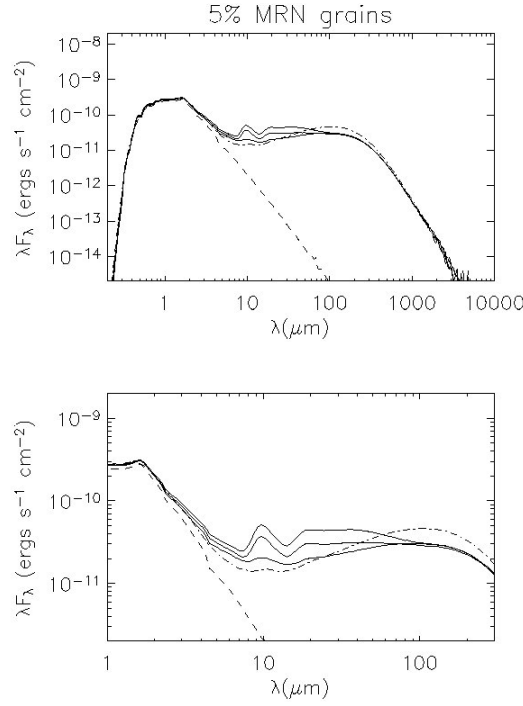


**Figure 3.3** SEDs generated with 5% MRN grains (solid lines) with the MRN grains at three different scale heights (lower line  $h_{100} = 9.68$ , middle line  $h_{100} = 14.53$  and upper line  $h_{100} = 19.37$ , all AU). SED of the disk composed of W02 grains only shown for comparison (dot-dashed line).

It is immediately obvious that the multi-grain disks are noticeably different from the single grain model as there is a pronounced reduction in the emission around  $100\mu\text{m}$ . This is due to the MRN grains at higher altitudes in the disk shadowing the larger W02 grains and emitting at shorter wavelengths than the W02 grains would normally emit at. The sub – mm part of the SED remains unchanged throughout but this is unsurprising as radiation in this part of the spectrum is primarily emitted from the cooler inner parts of the disk which are unaffected by the addition of the smaller grains.

Small Grains (MRN)				Large Grains (W02)			
Mass Frac.	$h_0$	$h_{(1\text{AU})}$	$h_{(100\text{AU})}$	Mass Frac.	$h_0(R_*)$	$h_{(1\text{AU})}(\text{AU})$	$h_{(100\text{AU})}(\text{AU})$
15%	0.008	0.03	9.68	100%	0.008	0.03	9.68
15%	0.012	0.046	14.53	100%	0.008	0.03	9.68
15%	0.016	0.061	19.37	100%	0.008	0.03	9.68

**Table 5.** Shows the grain parameters used to generate the SEDs of figure 3.4.

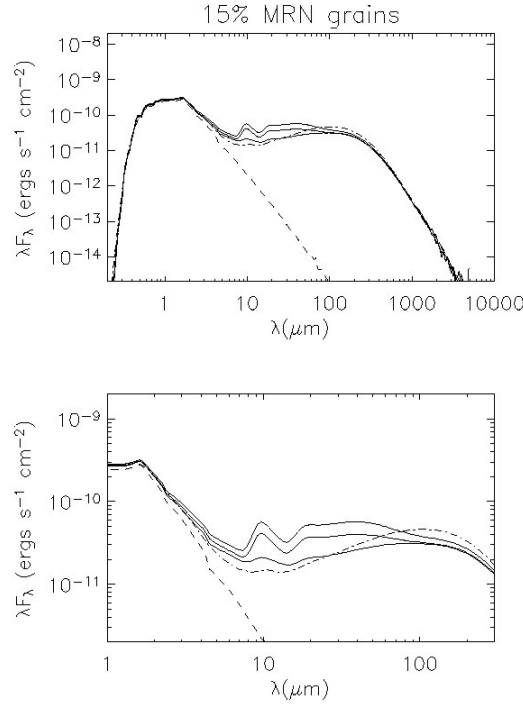


**Figure 3.4** SEDs generated with 15% MRN grains (solid lines) with the MRN grains at three different scale heights (lower line  $h_{100} = 9.68$ , middle line  $h_{100} = 14.53$  and upper line  $h_{100} = 19.37$ , all AU). SED of the disk composed of W02 grains only shown for comparison (dot-dashed line).

The inclusion of the smaller MRN size distribution is most obvious in the near – IR, particularly around  $10\mu\text{m}$ . Even the addition of just 1% of the disk mass is enough to cause a marked increase in emission in this region of the spectrum. With increasing scale height the effect becomes even more pronounced, simulating the conditions where larger grains have settled towards the midplane leaving the smaller grains at higher altitudes. As the fraction of mass contained in the MRN grains is increased the emission also increases and extends further into the mid – IR. These results agree well with the findings of D’Alessio et al. (2006; figure 12) and their investigation, described earlier in section 1.6.1 and shown here in figure 3.5. Rather than increase the scale height of the



small grains as I have done, they start with the two grain populations at different scale heights and increase the height of the large grains until they have a well mixed grain population. The overall result is the same with an obvious contribution to the near – IR from the smaller grain distribution.

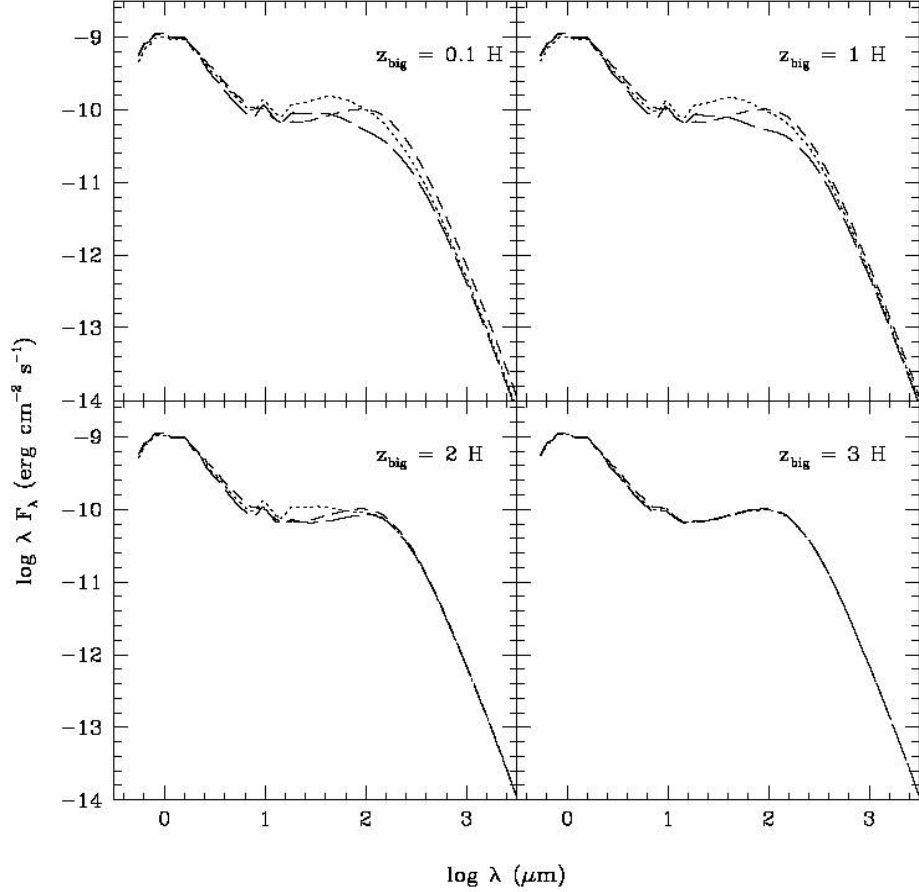


**Figure 3.5** SEDs showing dependence of height of big grains with scale heights of 0.1, 1, 2, 3 H. The models are for ISM dust and isotropic scattering, for  $\epsilon = 0.1$  (dotted line), and 0.01 (dashed line) and a well mixed model with  $a_{\max} = 1\text{mm}$  and  $\epsilon = 1$  (thick dashed line) for comparison. Taken from D’Alessio et al. (2006)

In order to understand the effects on the SEDs of the population of small grains being added with increased scale heights compared to the larger grains discussed above it is useful to examine cross-sections of the density and temperature distributions in the disk. Figure 3.6 shows vertical cuts through the density and temperature of the W02 grains and the W02 grains + 15% MRN grains models where the MRN grains have twice the initial scale height of the larger grains. The cuts are at 0.5, 5 and 100 AU and it can be clearly seen that the density of the W02 grains (solid and dot-dashed lines) is higher all

across the disk but has a narrower vertical extent above and below the disk midplane. Due to the fact that the MRN grains have a larger vertical distribution they intercept more direct radiation from the central source. This is apparent in the temperature cuts shown in figure 3.6. The single grain model has W02 grains (solid lines) with a higher temperature than in the multi-grain model as the MRN grains (dashed lines) shadow the W02 grains and have much higher temperatures than the embedded W02 grains.

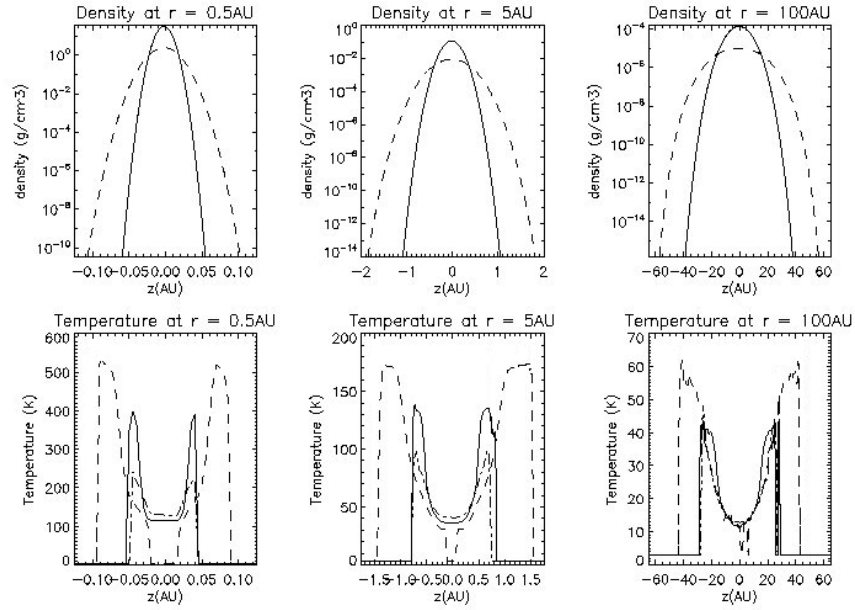


**Figure 3.6** Cuts through the midplane density and temperature distributions of the HH30 grains and W02 grains + 15% MRN models at 0.5, 5 and 100AU. Upper plots show density, lower plots show temperature, against vertical height above and below the disk midplane of W02 grains only (solid lines), W02 with MRN grains present (dot-dashed lines) and MRN grains (dashed lines).

### 3.4 Investigation of Dust Settling & Grain Growth in a sample of CTTS

The recent release of archival IRS data taken with the SPITZER space telescope in the near to mid-IR has given us the opportunity to look at the structure, extent and constituents of protoplanetary disks in greater detail than possible with ground based data. The IR region of the spectrum can provide information on the growth and evolution of the dust grains. In particular information on the small grain population with the presence or absence of Silicate features and the nature of the grains themselves along with whether or not they are amorphous or crystalline grains (Bouwman et al. 2001 & 2003) can be obtained.

After exploring the effects of multiple dust species with a range of scale heights and mass fractions in section 3.3 I will now model a number of T Tauri disks with publicly

available SPITZER IRS data in the near to mid-IR and data from the Kenyon & Hartmann (1995, hereafter KH95) compilation spanning a wavelength range from around  $0.1\mu\text{m}$  to a few millimetres. Several of the objects selected also have HST scattered light images which I have compared by eye with images of my model disks to provide a further constraint on the models. Table 6 lists the sources investigated and the stellar parameters that were used in the models.

Object	Spectral Type	$T_{\text{eff}}(\text{K})$	$M_*(M_{\odot})$	$R_*(R_{\odot})$
AA Tau	K7	4000	0.8	1.85
CoKu Tau/4	M1.5	3720	0.5	1.9
DM Tau	M1e	3720	0.65	1.2
GM Aurigae	K3/K5e/K7V	4730	1.2	1.5
GO Tau	M0	4000	0.8	1.3
LkCa 15	K5	4000	0.5	1.85
TW Hydra	K7V	4000	0.6	1

**Table 6.** The stellar parameters of the sources investigated throughout section 3.4.

The nature of MCRT models allows for a large number of variables to be incorporated and in some cases this can be unnecessary. In order to limit this variability I have used two documented grain size distributions throughout, the MRN distribution of Mathis, Rumpl & Nordsieck (1977) is the smaller of the two and consists of dust particles in the range  $0.005\mu\text{m} - 0.25\mu\text{m}$ . The larger of the two distributions is that of Wood et al. (2002a), developed for their investigation of the T Tauri star HH30 IRS. This distribution is an extension in particle size of the ISM distribution derived by Kim, Martin & Hendry (1994, hereafter KMH) described in section 1.6.1, equation 1.18 and referred to as the W02 distribution. In one model I have applied the KMH distribution for the smaller grains as it proved a better fit to the observations than the MRN grains. Figure 3.7 compares the optical properties of the W02, MRN and KMH size distributions.

A surface density of  $\Sigma \propto r^{-1}$  with the  $\alpha$  and  $\beta$  parameters set to 2.25 and 1.25 respectively in line with D'Alessio et al. (1999a) is applied throughout and disk radius of 200AU has been used unless a significantly different radius has been observed. This is a reasonable assumption as it has been shown that the radius of the disk does not have a large effect on its SED (Sholz et al. 2006 and Allers et al. 2006). The parameters of

the central protostars themselves are those reported in recent studies and as in the above investigation the only parameters being varied are the disk mass, mass fraction and scale height for each grain type and the inclination of the disk, summarised in table 7. For sources with directly visible central protostars the inclination has little effect on the SED and so unless other studies have determined an inclination angle I have adopted an angle of  $45^\circ$ .

The next few sections detail the models and fits to the observations and discuss what information we can learn from these results. Each model is compared using a “ $\chi^2$  goodness of fit” test with the equivalent HSEQ model generated using only the larger W02 grains with a self consistently solved density structure and no simulation of settling. While these are not unique fits they demonstrate the need for grain growth to explain the observed SEDs.

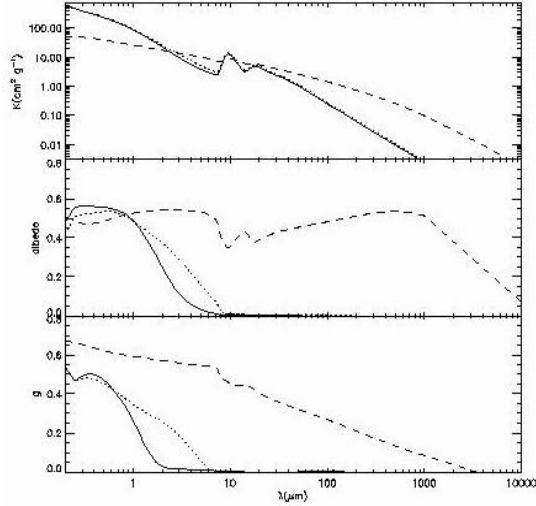


**Figure 3.7** Opacity, albedo and scattering function comparison for the MRN (solid line), KMH (dotted line) and HH30 (dashed line) grain size distributions.

The  $\chi^2$  test used here is a statistical method of assessing how well a model reproduces observation and the  $\chi^2$  value is given by:

$$\chi^2 = \frac{1}{N} \frac{\left[ \sum_{i=1}^N \log_{10}(D_i) - \log_{10}(M_i) \right]^2}{[\sigma_i / D_i / \ln(10)]^2} \quad (3.4)$$

where  $N$  is the number of data points (4 on average),  $D_i$  and  $M_i$  are the observed and model data points respectively and  $\sigma_i$  is the error in the observed data (2% for  $0 < \lambda \leq 20 \mu\text{m}$ , 5% for  $20 < \lambda \leq 99 \mu\text{m}$  and 10%  $\lambda \geq 100 \mu\text{m}$ ). The test has been carried out using IRAS data over a range of  $12 - 100 \mu\text{m}$ .

The chi-square distribution is a two-tailed distribution and if we assume the model values are normally distributed then the expectation value of chi-square is the value that has a 50% chance of being obtained. Half the time we would expect to obtain a chi-square value that is less than the expectation value and half the time we would expect a value greater than the expectation value. If we apply the standard 5% significance to the chi-squared values we are accepting a 5% chance that the distribution model for the data points is a poor fit. We assign the value of 0.025 to each end of the chi-square distribution curve so the chi-square probability values are then  $0.05/2 = 0.025$  (low value end) and  $1 - 0.05/2 = 0.975$  (high value end). If the value of chi-square obtained falls within the range of values that correspond to these two values, then we accept the hypothesis that the data are consistent with the model assumptions.

Here we have an average of 4 data points and the chi-square values corresponding to the probability values of 0.025 and 0.975 are 0.4844 and 11.14 respectively. If we obtained a chi-square value between these two values we would conclude that our data are consistent with our model assumptions.

### 3.4.1 AA Tau

The T Tauri star AA Tau is an excellent example of a classical T Tauri star that has been well studied over the years (Bouvier et al. 1999 & 2003, D'Alessio et al. 1999a) and exhibits a number of departures from a passive disk in HSEQ in its spectrum. It exhibits an achromatic, periodic variation in its photopolarimetry consistent with some form of occultation of the central star and its SED shows a strong Silicate feature and reduced mid-IR emission when compared to our HSEQ SED model (figure 3.8). This may be due to ongoing dust settling. In chapter 2 I discussed modelling the photopolarimetric variability of this source, in this section however I will be concerned with what the new SPITZER IRS data can reveal about the state of dust settling and grain growth in this object.

The central star in this system has been classified as a K7 dwarf (Kenyon & Hartmann 1995), with a mass of  $0.8M_{\odot}$ , radius of  $1.85R_{\odot}$  and an effective temperature of  $4030 \pm 30\text{K}$  (Bouvier et al. 1999), although a temperature of 4000K was used here. An inclination estimate of  $70^{\circ}$  or greater (Bouvier et al. 1999) has been inferred from analysis of the systems photometric variability and IR excess emission (e.g., D'Alessio et al. 1999), in chapter 2 I derived an inclination of  $75^{\circ}$ .

The best fit to the observational data shown in figure 3.8 was for a disk with a mass of  $0.015M_{\odot}$ , radius of 200AU inclined at  $71^{\circ}$ . I found that in order to fit the observations I not only needed two dust species with a degree of settling throughout the disk but an inner disk stretching out to 10AU from the star that consisted of only the smaller MRN grains. 10% of the disk mass is contained in this inner region and the material has a scale height of  $h_{100} = 15.57$ . This is the scale height of the material at a radius of 100AU and will be represented as  $h_{100}$  hereafter. Throughout the rest of the disk 60% is composed of the larger W02 dust with  $h_{100} = 5.19$  and the remaining 30% is made up of the MRN grains in the outer part of the disk with  $h_{100} = 9.34$ . The different grains have different scale-heights as expected if the large grains are to preferentially settle out.

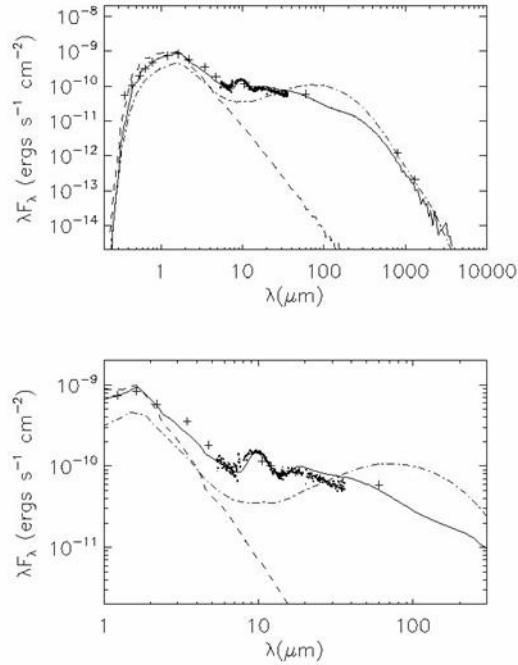


**Figure 3.8** SED models for AA Tau. Broken line is HSEQ disk and solid line is multiple species model. The small filled dots are the SPITZER IRS data and the crosses are the IRAS data from the KH95 compilation.

The model looks to reproduce the observations well, particularly the high resolution SPITZER data and there was a noticeable difference between my model and the HSEQ model.  $\chi^2_M = 8.5$ ,  $\chi^2_H = 175.6$ , indicating that in this case my model produces a better fit than that of the HSEQ model. As predicted in chapter 2 the inclination is higher than  $70^{\circ}$  (although not as high as the  $75^{\circ}$  predicted there) and this reinforces the case for dust settling in this object as the inability of the HSEQ model to fit the stellar dominated

emission implies that the star is being obscured at this inclination by the flared outer regions of the disk. In the settled disk the flaring is less pronounced and hence the central star is still visible and its contribution to the resultant SED matches the observations.

The presence of the inner disk of smaller particles is interesting as it implies that something is preventing the growth of these grains as in the rest of the disk and producing this discontinuous size distribution. While it is accepted that a young planet in this region would accrete the available circumstellar material and produce the cleared gaps in the disk now being observed some other mechanism must be responsible for maintaining an inner disk of only small ISM type grains. A recent study by Rice et al. (2006) has shown that the presence of a young planet in the inner regions of a disk not only creates an annular gap in the planets orbit but can also act as a filter. Pressure gradients at the inner edge of the cleared region prevent particles larger than a critical size from entering the cleared region. Rice et al. (2006) found that this critical size is typically around  $10\mu\text{m}$  (dependent on the mass of the planet) which compares well with my inner disk consisting entirely of small, ISM type grains. The fact that we require material in this inner region also fits well with observed flux levels attributed to accretion onto the stellar surface and the hypothesis that a warp in the inner regions of the disk is responsible for the photopolarimetric variability observed in this system. An accretion rate of  $5 \times 10^{-9} \text{ M}_{\odot} \text{ yr}^{-1}$  gave the best fit to the above data, much more than this and the flux levels across the near – IR begin to rise. Figure 3.9 shows scattered light images of the disk model at an inclination of  $71^{\circ}$  with an obvious dark dust lane running through the image.

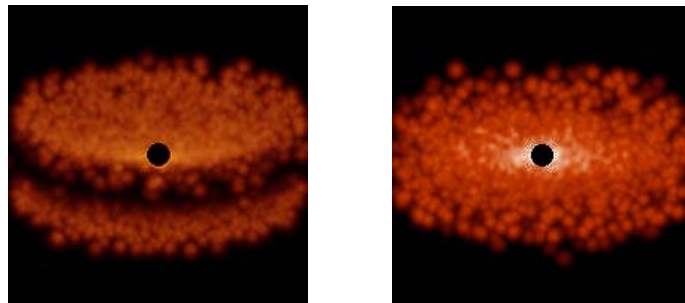


**Figure 3.9** K-band (left) and  $160\mu\text{m}$  (right) images of AA Tau inclined at  $71^{\circ}$  (400AU on a side). The central star has been coronagraphically removed.

### 3.4.2 CoKu Tau/4

This relatively young object, thought to be  $\sim 1$  Myrs old (Webb et al. 1999), exhibits the signature in its SED of a large evacuated inner hole in its disk which may be attributed to clearing by a planet (Quillen et al. 2004). If this is indeed the case then it would require planet formation to occur much earlier and progress much more rapidly than the few million years generally thought (Wuchterl et al. 2000, Nagasawa et al. 2007). A recent study of this object by D'Alessio et al. (2005) modelled Coku Tau/4 with a  $0.5M_{\odot}$  star with a radius of  $1.9R_{\odot}$  at 3720K and a disk with a radius of 200AU with an inner hole of radius  $\sim 10$ AU and a mass of  $0.001M_{\odot}$ , they estimate that there is  $0.007 M_{\text{Lunar}}$  of material in the cleared hole. They are undecided about the disk's inclination and settle on it being virtually face on with quite a large extinction,  $A_v = 3$ . This large extinction means that all inclinations lower than  $70^{\circ}$ , the point where the disk obscures the central star, produce virtually the same SED and these parameters are unable to fit the 1 -  $10\mu\text{m}$  data or the data from 30 –  $100\mu\text{m}$ , both regions they do not show in their fits.

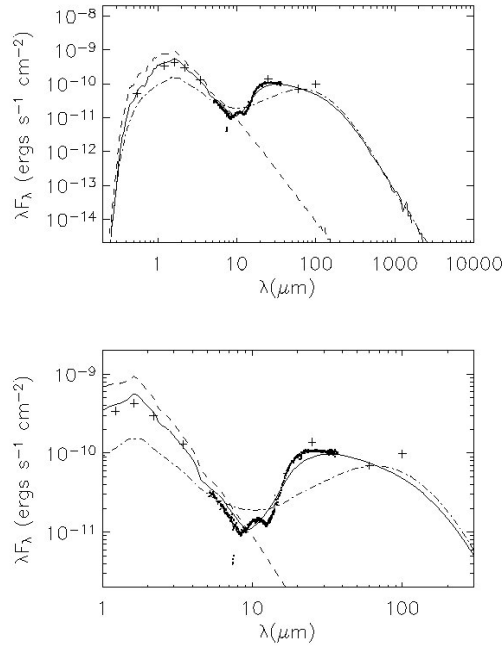


**Figure 3.10.** SED models for CoKu Tau/4. Broken line is HSEQ disk and solid line is multiple species model. The small filled dots are the SPITZER IRS data and the crosses are the IRAS data from the KH95 compilation.

I find the best fit to the observational data (shown in figure 3.10) using the same stellar and disk parameters as in the previously mentioned investigation but with an inner hole



of radius 8.5AU and an inclination of  $76^\circ$ . The large evacuated inner hole in the disk is responsible for the large dip in the near - IR region of the SED. The small silicate emission feature at the base suggests that there is some small, MRN distribution sized material in a very thin, low mass disk responsible for this emission. My inclined disk reproduces the sub-micron and mid to far - IR emission with an outer disk made up of 98.9995% W02 grains with  $h_{100} = 10.31$  and 1% MRN grains with  $h_{100} = 10.31$ . In the inner disk the tiny amount of material responsible for the silicate emission was best reproduced by a disk of MRN grains consisting of only 0.0005% of the total disk mass with  $h_{100} = 0.516$ .

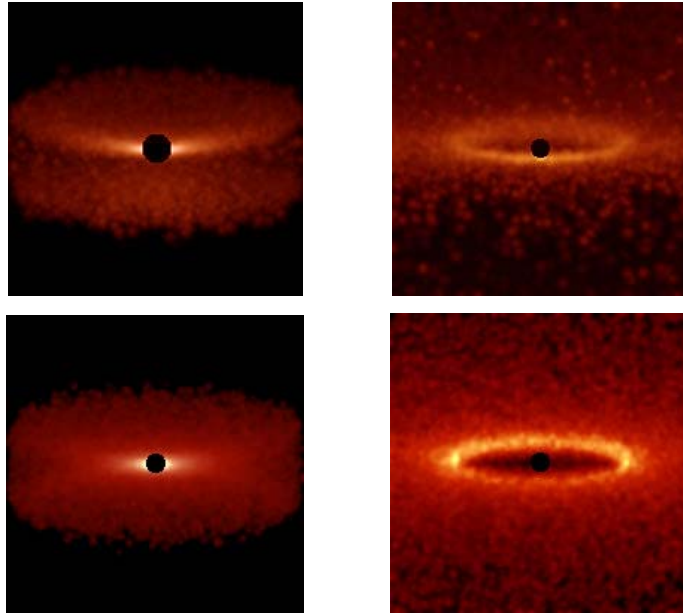


**Figure 3.11** Upper panels show K-band images of CoKu Tau/4, the lower panels show images at  $160\mu\text{m}$ . The disk has an inclination of  $76^\circ$  and the left-hand images are 400AU on a side, with the right-hand images 30AU on a side. The central star has been coronagraphically removed.

There was a noticeable difference between my model and the HSEQ model.  $\chi_M^2 = 11.2$ ,  $\chi_H^2 = 60.9$ , indicating that in this case my model produces a better fit than that of the HSEQ model, although slightly outside the range of acceptable values. The HSEQ model produces a disk that is too large in vertical extent to directly observe the central star at such a high inclination so fails to reproduce the optical component of the SED. At the same time the simple inclusion of an evacuated inner region fails to reproduce the depth of the observed feature or the correct wavelength range of the spectrum affected by it. Predicted images of the inclined disk of CoKu Tau/4 are shown in figure

3.11. Observations in the far – IR are necessary to determine the mass and extent of the disk and aid in finding a more detailed description of the grain growth and dust settling present in this object.

The close-up image, also shown in figure 3.11 shows the dark inner hole and the brightly illuminated inner wall of the outer disk's inner edge. This feature is responsible for the emission around  $20\mu\text{m}$  and a more detailed treatment of both the temperature structure and the shape of the disk may better reproduce the observed emission (details of an approach to this problem including a rounding of the inner edge can be found in Isella & Natta 2005).

### 3.4.3 DM Tau

The central star in the DM Tau system has been classified as a K5 and the disk is believed to have an inclination of  $37^\circ$  (Schneider et al. 2007). A recent study by Calvet et al. (2005) used a central star of mass  $M_* = 0.65M_\odot$ , radius  $R_* = 1.2R_\odot$  and temperature of 3720K. In this study they used a disk of mass  $M_d = 0.05M_\odot$  inclined at  $40^\circ$ . I have included their model SEDs for comparison in figure 3.12.

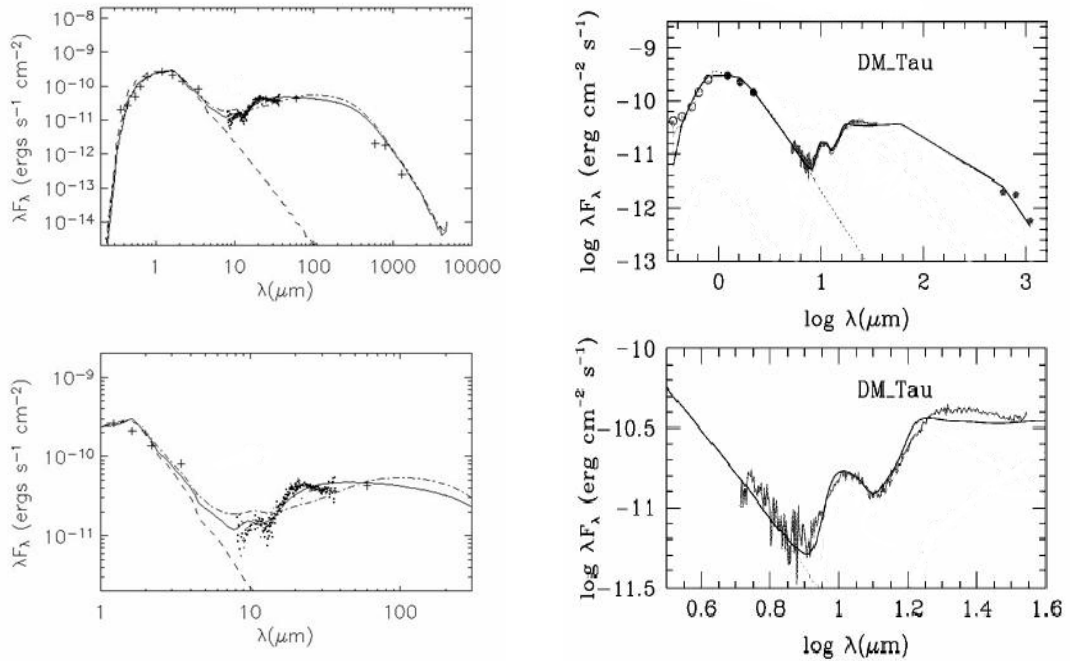


**Figure 3.12** Comparison of model SED fits to DM Tau observations. Left hand side is my multiple dust species model where the broken line is HSEQ disk and solid line is multiple species model. The small filled dots are the SPITZER IRS data and the crosses are the IRAS data from the KH95 compilation. The right hand side is the Calvet et al. (2005) model using the same data sets.

The observed SED was reproduced using a central star with a mass  $M_* = 0.65M_\odot$ , a radius  $R_* = 1.2R_\odot$  and a temperature of 3720K. I used a disk with a mass  $M_d = 0.05M_\odot$  and a radius  $R_d = 200\text{AU}$ , inclined at  $40^\circ$  and found that, like Calvet et al. (2005), the disk model required an inner hole (also speculated about by Schneider et al. 2007) stretching out to 4.5AU (larger than the Calvet et al. estimate of 3AU) with a very low density disk of MRN grains inside this annulus. Only 0.009% of the disk mass is inside this annulus and this inner disk has  $h_{100} = 8.1$  while throughout the rest of the disk there is a mixture of both dust species with 94.991% of the mass in the form of the W02 type grains,  $h_{100} = 9.83$ , and another 5% of the mass made up of MRN grains with  $h_{100} = 9.26$ . The  $\chi^2$  values for my model and the HSEQ model are  $\chi_M^2 = 0.06$  and  $\chi_H^2 = 0.39$  respectively, and so in this case there is little difference between the two models and both values lie outside the expected range.

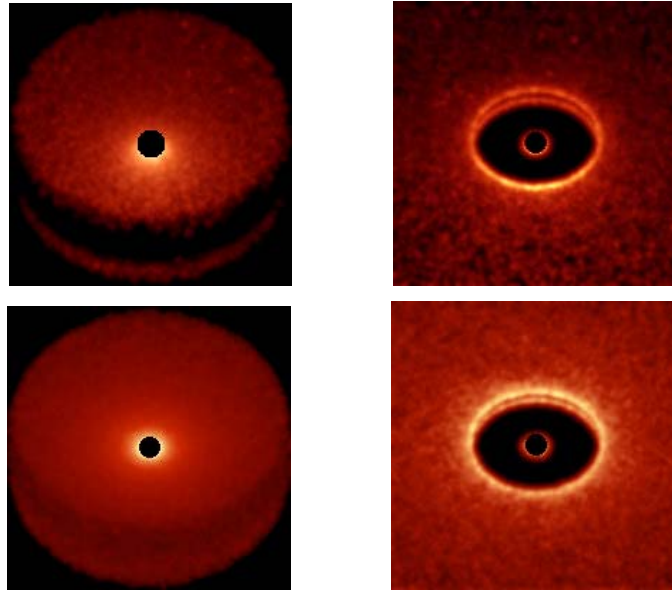


**Figure 3.13** Upper panels show K-band images of DM Tau, lower panels show images at 160μm. The disk has an inclination of  $40^\circ$  and the left-hand images are 400AU on a side with the right-hand images 20AU on a side. The central star has been coronagraphically removed.

These parameters reproduce the depth of the drop in emission around  $10\mu\text{m}$  and the shape of the silicate emission feature at  $10\mu\text{m}$ , the far – IR emission is also reproduced indicating a good estimate of the disk optical depth (mass). Again the steep slope and rapid change in the shape of the emission around  $20\mu\text{m}$  isn't exactly reproduced and this is most likely due to an insufficiently detailed treatment of the shape of the inner edge

of the outer disk (Isella & Natta 2005). The Calvet et al. (2005) model examines this effect in some detail and uses techniques developed by D'Alessio et al. (2005) to model the contribution of this irradiated wall. They use a single power law size distribution of dust grains with exponent 3.5 between  $0.005\mu\text{m}$  and  $0.25\mu\text{m}$  (equivalent to MRN grains) but have a layered disk structure with differing optical depths, increasing towards the midplane to reproduce the settling and grain growth of the system.

The simulated images of DM Tau shown in Figure 3.13 show a very pronounced dust lane in the K-Band due to the inclination of the source. The close-up image shows the bright ring of the wall-like inner edge of the outer disk with a slightly darker line running through the centre of the far edge of the ring due to shadowing by the low density inner disk.

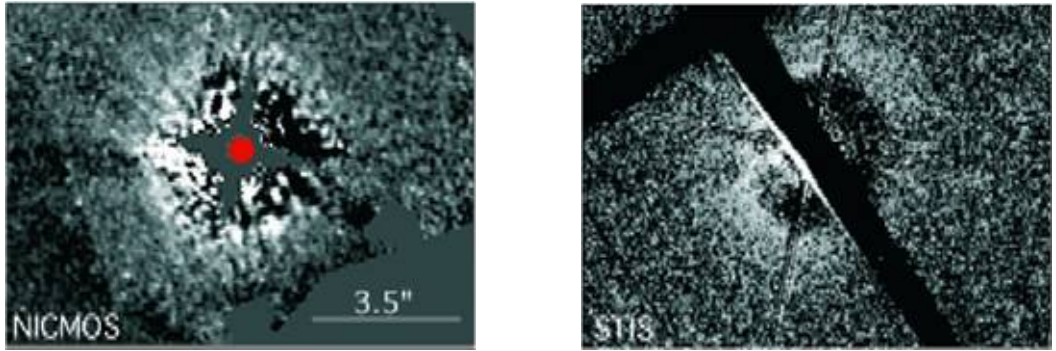


**Figure 3.14** Images of DM Tau taken with NICMOS (left) and STIS (right) on the Hubble Space Telescope, both images are on the same scale shown on the right of the NICMOS image. Images taken from Schneider et al. (2007).

For comparison I have included two images of the source taken with NICMOS (Near Infrared Camera and Multi-Object Spectrometer) and STIS (Space Telescope Imaging Spectrograph) on the Hubble Space Telescope, shown in figure 3.14, from Schneider et al. (2007). Both these images seem to show a very large dark area surrounded by a brighter annulus, Schneider estimates the inner dark area has a radius of 240AU and the brighter annulus stretches out a further 80AU to 320AU. This is much larger than the disk I (and Calvet et al. 2005) have modelled and the cleared hole I have simulated but the properties of the SED do not indicate such a massive disk or large cleared area and from the fit I have obtained seem unlikely.

### 3.4.4 GM Aurigae

There has been a lot of interest in GM Aurigae over recent years with speculation that it has a large evacuated inner region in its protoplanetary disk possibly due to clearing by a planet sized object (Marsh & Mahoney 1992, Koerner et al. 1993, Rice et al. 2003a). As with DM Tau, Calvet et al. (2005) have applied their model to this source and I have included their model SED for comparison in figure 3.15.

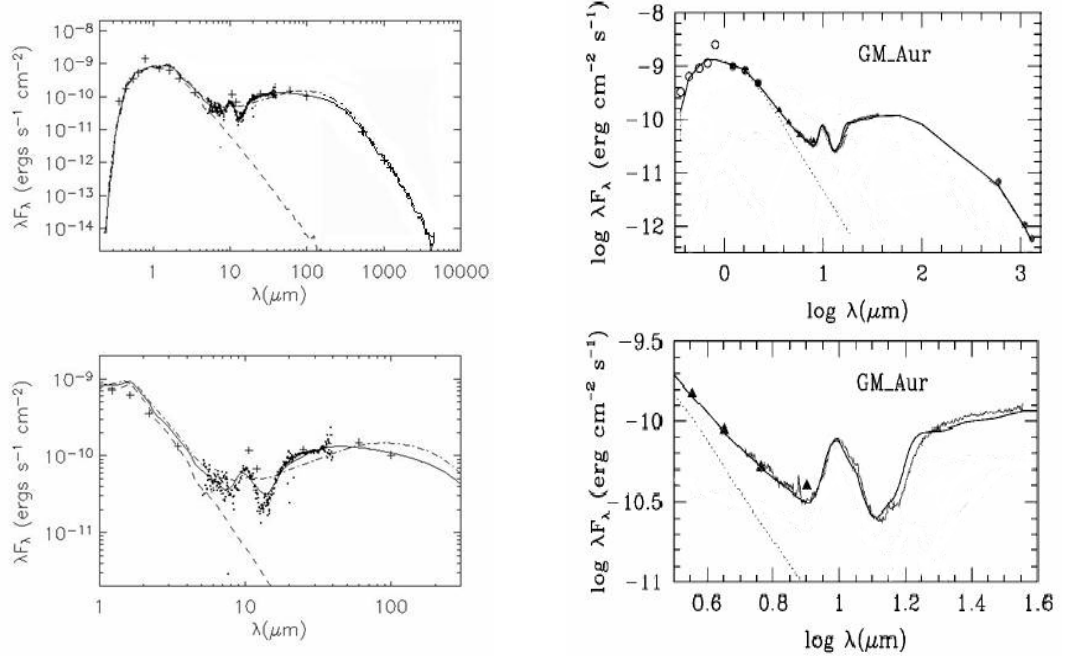


**Figure 3.15** Comparison of model SED fits to GM Aurigae observations. Left hand side is my multiple dust species model where the broken line is HSEQ disk and solid line is multiple species model. The small filled dots are the SPITZER IRS data and the crosses are the IRAS data from the KH95 compilation. The right hand side is the Calvet et al. (2005) model using the same data sets.

There are a few differences in the models used to produce the SEDs shown in figure 3.15, aside from the different technique used by Calvet et al. (2005) mentioned in section 3.4.3. The Calvet model uses a central star with  $M_* = 1.2M_\odot$ , a radius  $R_* = 1.5R_\odot$  and a temperature of 4730K ( $L_* = 1L_\odot$ ). Their disk is inclined at  $55^\circ$ , has a mass  $M_d = 0.09M_\odot$  and an inner hole with radius  $R_h = 24\text{AU}$ . While I fit the observational data with the Schneider et al. (2003) parameters;  $M_* = 0.85M_\odot$ ,  $R_* = 1.75R_\odot$  and a temperature of 4000K ( $L_* = 0.71L_\odot$ ). The disk in this model also has an inclination of  $55^\circ$  but has a lower mass,  $M_d = 0.047M_\odot$ , and in that paper extended from 0.25 – 300AU. With the inclusion of the SPITZER IRS data it becomes more obvious that an inner hole is required to reproduce the SED but unlike the very sparsely populated holes

in the previously described systems GM Aurigae exhibits slightly different characteristics. Calvet et al. (2005) found the SED is best reproduced by having a small inner disk stretching from near the stellar surface (0.25AU) to 5AU and then an evacuated/cleared annulus stretching out to 20.5AU where there is a disk wall at the inner edge of the outer protoplanetary disk which has the standard flared structure used throughout. I found that an inner disk containing 0.7% of the total mass and consisting of MRN grains with  $h_{100} = 7.89$  and an outer disk containing 0.9% MRN and 98.4% W02 grains by mass with  $h_{100} = 15.79$  and  $h_{100} = 7.89$  respectively gave the best reproduction of the observed SED. The chi-squared values of both my model and the HSEQ model,  $\chi_M^2 = 3.1$ ,  $\chi_H^2 = 8.1$  respectively, lie within the expected range so in this case there is little difference between the two models.

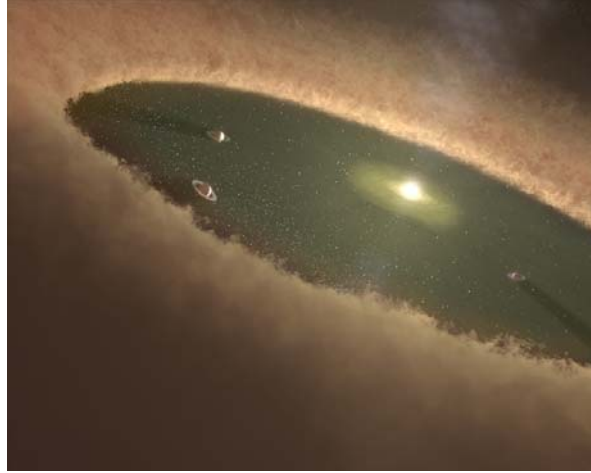


**Figure 3.16** Artist's impression of GM Aurigae showing inner disk wall, evacuated region and central dust disk (image from NASA)

This evacuated annulus is believed to have been cleared by the formation of one or more young Jupiter - like planets (Rice et al. 2003a) and is reminiscent of our own solar system which also has gas giant planets orbiting between 5 and 20AU from their parent star. Figure 3.16 shows an artist's impression of what this system might look like and depicts nicely the inner dusty disk and thicker outer disk with its walled inner edge.

The scattered light images produced by my model are shown in figure 3.17 and look a lot like the artist's impression of the GM Aurigae system. An interesting feature that is obvious in the K-band images is the dark band on the face of the outer disk's inner wall. A similar effect was also visible in the model K-band images of DM Tau in section

3.4.3, although not as pronounced, and is due to shadowing from the material in the inner part of the disk.

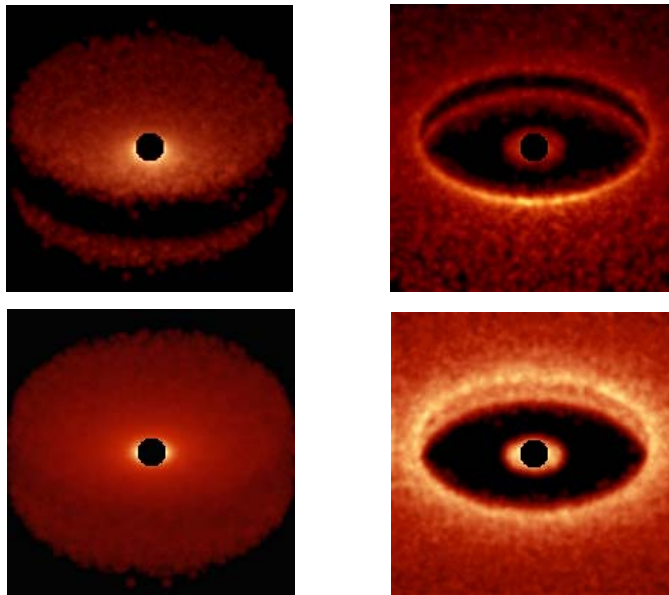


**Figure 3.17** Upper panels show K-band images of GM Aurigae, lower panels show images at 160μm. The disk has an inclination of 55° and left-hand images are 400AU on a side with the right-hand images 50AU on a side. The central star has been coronagraphically removed.

A two-colour combination of the F110W and F160W filters on the Hubble Space Telescope's NICMOS instrument image of GM Aurigae is shown in figure 3.18. The bright upper disk surface with the dark dust lane below and the fainter lower disk surface are clearly visible. The inner regions are not resolved but the general shape of the system matches the model images of figure 3.17.



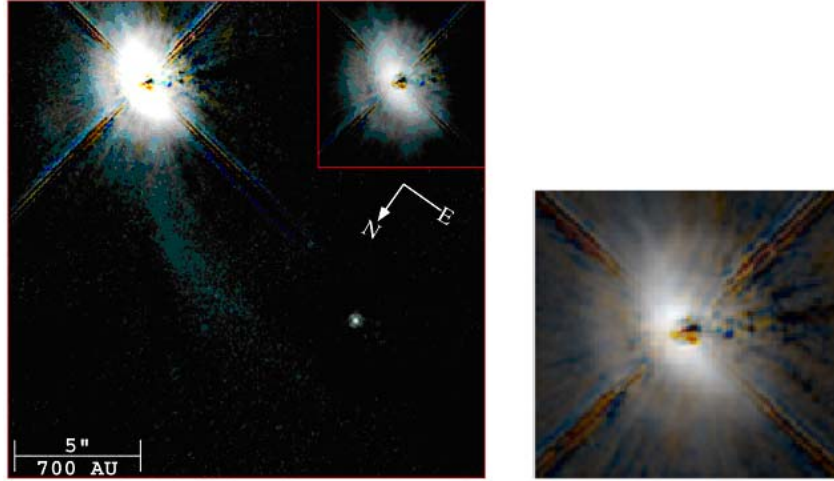


**Figure 3.18** Two-colour composite images of GM Aurigae using the F110W and F160W filters on the HST NICMOS coronagraph, the left panel shows the logarithmic display stretch of the full  $19.4'' \times 19.3''$  field and the right panel is an enlargement of the inset image in the left panel concentrating on the protoplanetary disk itself. Taken from Schneider et al. (2003)

### 3.4.5 GO Tau

GO Tau has been classified as an M0 star by Kenyon & Hartmann (1995) and Furlan et al. (2005) used the SPITZER data of this source to show how variations to their dust settling model would look against a “typical” low-mass CTTS.

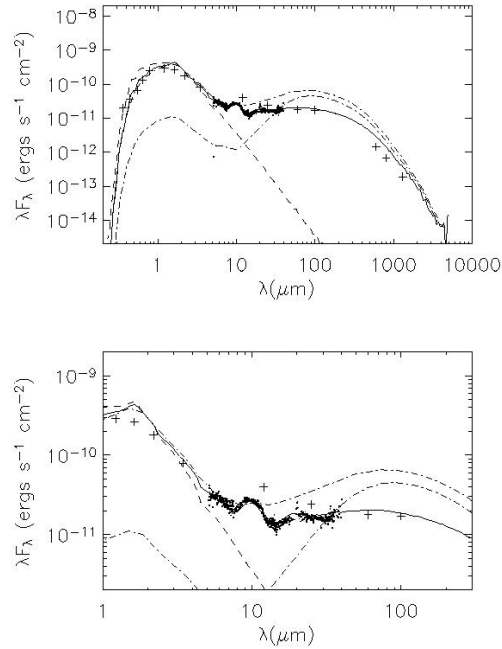


**Figure 3.19** SED models for GO Tau. Broken lines are HSEQ disk (lower curve is for an inclination of  $75^\circ$  while the upper is for  $66^\circ$ ) and solid line is multiple species model (at an inclination of  $75^\circ$ ). The small filled dots are the SPITZER IRS data and the crosses are the IRAS data from the KH95 compilation.



The SED for this source, shown in figure 3.19, doesn't exhibit the large drop in IR emission from  $\sim 6\mu\text{m}$  to  $\sim 20\mu\text{m}$ , suggesting that there is no evacuated inner hole in the protoplanetary disk caused by planetary formation or some other mechanism. This would suggest that GO Tau is younger than some of the other sources exhibiting clearing but there is no indication that it is significantly younger (Furlan et al. 2005) so there may be no planet formation in the innermost regions of the disk at present. There is, however, evidence for dust settling and grain growth in this system. The mid – IR section of the emitted spectrum is much lower than expected for a disk in HSEQ and the model shown in figure 3.19 is for a disk with an inclination of  $75^\circ$  but at this inclination a disk in HSEQ obscures the central star and removes the stellar emission component from the SED (shown in figure 3.19).

Using a central star with mass  $M_* = 0.8M_\odot$ , a radius  $R_* = 1.3R_\odot$  and a temperature of 4000K and a disk with mass  $M_d = 0.065M_\odot$ , extending out to 200AU and inclined at  $75^\circ$  I was able to reproduce the observed spectral data. In this model the protoplanetary disk consists of 98.5% W02 and 1.5% MRN grains by mass with initial scale heights  $h_{100} = 5.1$  and  $h_{100} = 6.8$  respectively. There was a significant difference between my model and the HSEQ model,  $\chi_M^2 = 4.1$ ,  $\chi_H^2 = 58.3$ , indicating that in this case my model produces a better fit than that of the HSEQ model.

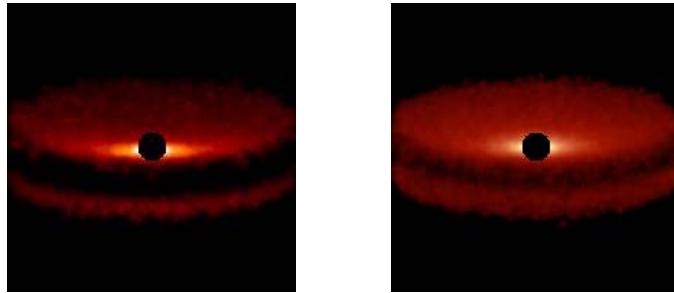


**Figure 3.20** K-band image (left) and  $160\mu\text{m}$  image (right) of GO Tau with an inclination of  $75^\circ$  (images are 400AU on a side). The central star has been coronagraphically removed.

Not only the mid and far – IR emission is reproduced with this model but the Silicate emission feature at  $10\mu\text{m}$  is also reproduced. The smaller grains responsible for this are more abundant near the star and in the upper surface regions of the disk, also an indication that grain growth and settling is ongoing in this system.

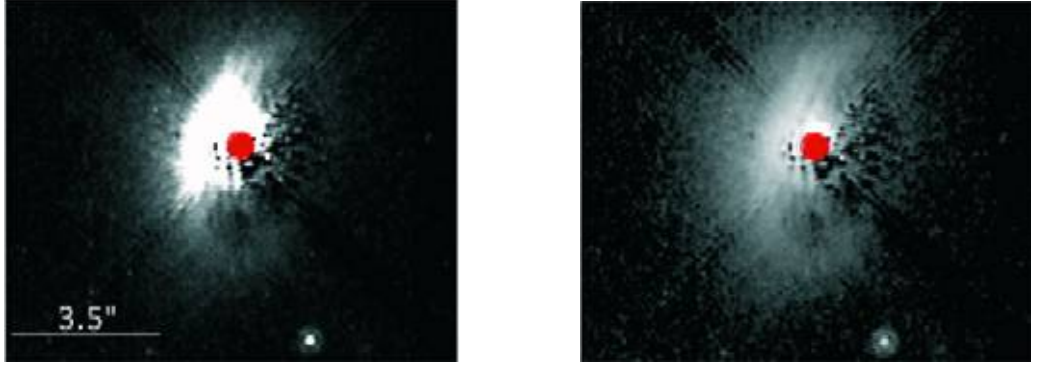


**Figure 3.21** Images of GO Tau taken with NICMOS, the image on the left is a linear display of 0 - 0.134mJy arcsec<sup>-2</sup> and the image on the right is a logarithmic display from 0.02 - 3.2mJy arcsec<sup>-2</sup>. Both images are on the same scale shown on the left. Images taken from Schneider et al. (2007).

As the disk is at such a high inclination there is a pronounced dark dust lane in both the scattered light images of the model, shown in figure 3.20. Figure 3.21 shows HST NICMOS images of GO Tau. Of the sources modelled here GO Tau shows one of the largest departures from HSEQ in its SED which implies that its disk is flatter than HSEQ disks.

#### 3.4.6 LkCa15

The central star of this object has been classified as K5 by Kenyon & Hartmann (1995). For this investigation I have used a central star with a mass  $M_* = 0.5M_{\odot}$ , a radius  $R_* = 1.85R_{\odot}$  and a temperature of 4000K and a disk with mass  $M_d = 0.075M_{\odot}$ , extending out to 200AU and inclined at 45°. The large drop in emission between 6 $\mu$ m and 20 $\mu$ m indicates the presence of a cleared region in the inner disk and the very low ‘flat’ mid – IR emission profile suggests a very thin settled disk is present.

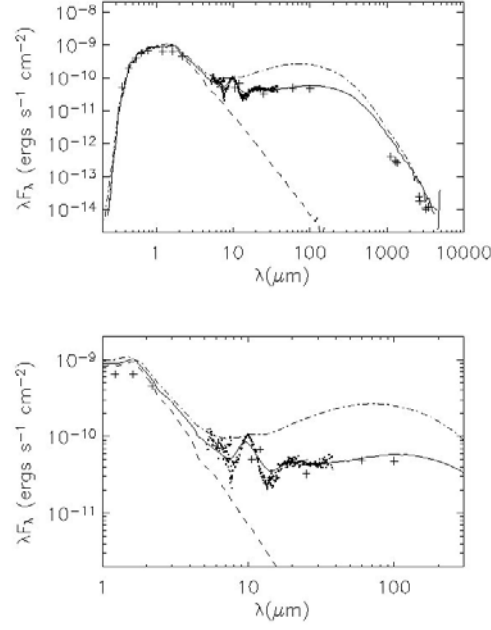


**Figure 3.22** SED models for LkCa15. Broken line is HSEQ disk and solid line is multiple species model.

The best reproduction of the observed SED (shown in figure 3.22) required a very sparsely populated inner disk stretching out to only 2AU with a cleared annulus stretching out a further 13AU to 15AU where the disk then extends out to 200AU. The inner part of the protoplanetary disk consists of 0.02% of the disk mass in the form of MRN grains with a scale height of  $h_{100} = 12.98$ . The outer disk consists of 99.93% W02 and 0.05% MRN grains by mass with initial scale heights  $h_{100} = 5.19$  and  $h_{100} = 13.49$  respectively. There was a significant difference between my model and the HSEQ model,  $\chi_M^2 = 17.6$ ,  $\chi_H^2 = 190$ , indicating that in this case my model produces a better fit than that of the HSEQ model, as can also be seen by eye, although both values are outside the expected range.

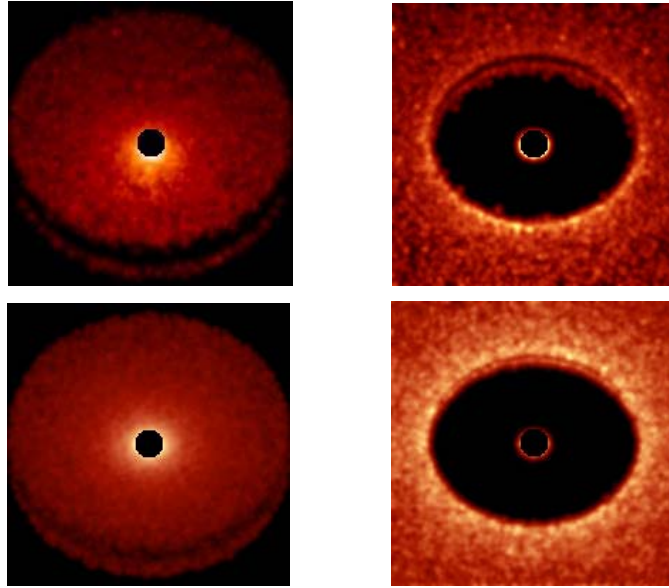


**Figure 3.23.** Upper panels show K-band images of LkCa15, lower panels show images at  $160\mu\text{m}$ . The disk has an inclination of  $45^\circ$  and the left-hand images are 400AU on a side with the right-hand images 40AU on a side. The central star has been coronagraphically removed.

The scattered light images of the model disk, shown in figure 3.23, again show the dark shadowed region on the face of the outer disks inner wall, most evident in the K-band images. This wall is also far dimmer than the walls of the disks investigated previously. This is due to the lower inclination of the disk meaning that less radiation is reflected towards the observer and the overall reduction in the disks vertical thickness.

### 3.4.7 TW Hydra

An investigation into the small TW Hydrae association was carried out by Jayawardhana et al. (1999) who found that of the fifteen members only four showed any significant IR excess indicating the presence of circumstellar disks. They found that only TW Hydra exhibited an optically thick, actively accreting disk and that this system is  $\leq 10$  Myr old and as such of great interest for studying the onset of planetary formation in this type of object.

A study of this system's disk was undertaken by Wilner et al. (2000) using the Very Large Array, VLA, to image the disk at 7mm and 3.6cm. They attributed the observed 7mm emission to a disk viewed almost pole on extending to a radius greater than 50AU with a mass of around  $0.03M_\odot$ . The near – IR was studied by Sitko et al. (2000) and evidence for silicate emission around  $10\mu\text{m}$  was found but without mid – IR data very little could be inferred about the overall structure of the TW Hydra disk.

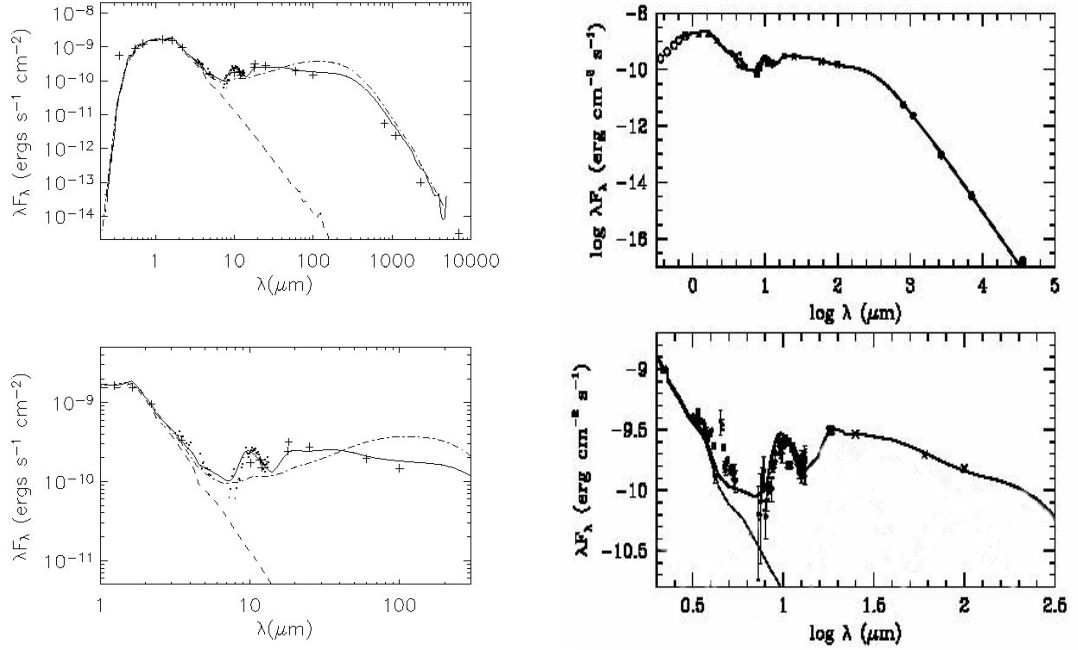


**Figure 3.24** Comparison of model SED fits to TW Hydra observations. Left hand side is my multiple dust species model where the broken line is HSEQ disk and solid line is multiple species model. The small filled dots are the SPITZER IRS data and the crosses are the IRAS data from the KH95 compilation. The right hand side is the Calvet et al. (2002) model using data sets from Rucinski & Krautter (1983; average of UBVR measurements), Webb et al. (1999), Sitko et al. (2000), their 2002 paper, Jayawardhana et al. (1999), IRAS (de la Reza et al. 1989; Gregorio-Hetem et al. 1992), Weintraub, Sandell, & Duncan (1989), Wilner (2001), and Wilner et al. (2000), see paper for details.

A model requiring significant grain growth and the evacuation of the inner disk to fit the observed emission was derived by Calvet et al. (2002). They used an outer disk extending to 140AU with a mass of  $0.06M_{\odot}$ , much larger than that estimated from the 7mm data of Wilner et al. (2000), with the inner 4AU of the disk being optically thin. They found that they required a mass of  $0.5M_{\text{Lunar}}$  of small ISM type grains to reproduce the observed silicate emission. They took the combination of these effects to signify the onset of gap clearing by the formation of a growing protoplanet, they're fit of the SED is shown in figure 3.24.

My SED model for TW Hydra comprises a central star with a mass  $M_{*} = 0.6M_{\odot}$ , a radius  $R_{*} = 1R_{\odot}$  and a temperature of 4000K and a pole on disk of mass  $M_d = 0.04M_{\odot}$  (more inline with the 7mm predictions), extending out to 200AU. Like Calvet et al. (2002), I required an inner disk of small particles (MRN grains) extending out to 4AU consisting of 8% of the total disk mass and with an initial scale height of  $h_{100} = 12.11$ . The outer disk was composed of 91% larger W02 grains and only 1% MRN grains with  $h_{100} = 7.26$  and  $h_{100} = 16.35$  respectively. This may be explained if there has been a

large degree of dust settling and grain growth in this system and that there are indeed the beginnings of a cleared inner disk. The difference between my model and the HSEQ model,  $\chi_M^2 = 4.1$ ,  $\chi_H^2 = 34.8$ , indicates that in this case my model produces a better fit than that of the HSEQ model.

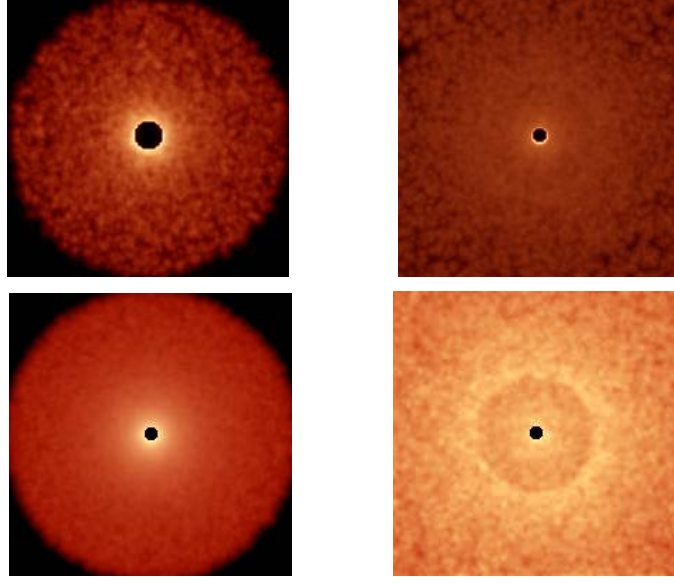


**Figure 3.25** Upper panels show K-band images of TW Hydra, lower panels show images at 160μm. The disk has an inclination of 0° and the left-hand images are 400AU on a side with the right-hand images 20AU on a side. The central star has been coronagraphically removed.

Scattered light images of my model disk are shown in figure 3.25 with NICMOS images in figure 3.26 for comparison. In the close up image on the upper right of figure 3.25 the faint outline of the inner disk region can just be made out but at this stage the low density MRN grains in this region scatter so much of the incident light that the clearing in the inner disk will not yet be very apparent in observations in the IR. Observations at longer wavelengths may be able to detect the inner disk as it is much more obvious at a wavelength of 160μm (lower right image in figure 3.25).

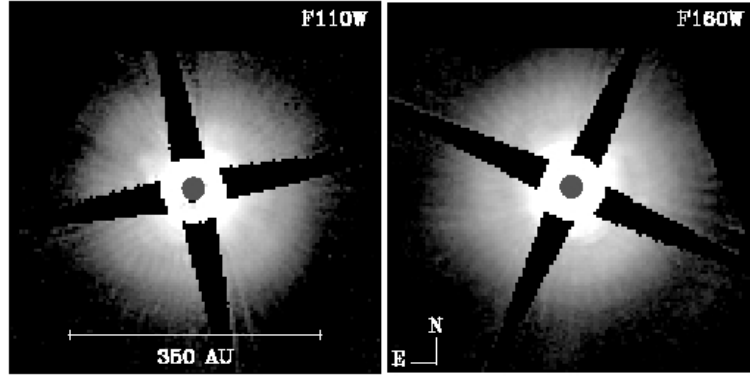


**Figure 3.26** Scattered light images of the disk of TW Hydra taken at two wavelengths with the NICMOS camera on the Hubble Space Telescope. Both images are shown with a natural logarithmic stretch and on the same spatial scale and orientation. Images taken from Weinberger (2006).

The NICMOS images taken of TW Hydra lack the spatial resolution to view the inner regions directly but they show a disk that is roughly pole on and don't exhibit any signs of dark dust lanes seen in more inclined objects. The disk appears to be slightly smaller than the one I have modelled which has a radius of 200AU, the NICMOS images suggest a radius of  $\sim 175$  AU, but this difference shouldn't significantly affect the SED.

### 3.5 Conclusion

Throughout this chapter I have presented model SEDs fitting the latest publicly available IR data on a number of sources at differing stages of evolution in the ongoing process of planetary system formation and accretion of protoplanetary disk material.

The model parameters used to fit the observational data throughout this section are summarised in table 7 and the comparison of my models with the HSEQ models are summarised in table 8. I have shown that my multiple dust species model is capable of reproducing the observations and that the departures from HSEQ in the SEDs may be explained by the observed effects of dust grain growth and settling. The SEDs modelled in this chapter are displayed in figures 3.27 and 3.28. Figure 3.27 shows the full range of the SEDs modelled while figure 3.28 shows a close up of the near-IR region from  $1\mu\text{m} - 130\mu\text{m}$  of the SED.

	AA Tau	CoKu Tau/4	DM Tau	GM Aur	GO Tau	LkCa15	TW Hydra
Inclination	71°	76°	40°	55°	75°	45°	0°
$M_{\text{disk}}(M_{\odot})$	0.015	0.001	0.05	0.047	0.065	0.075	0.04
Inner Disk							
Radius (AU)	0-10	0-8.5	1-4.5	5-20.5	N/A	2-15	0-4
Small Grains							
Mass Fraction	0.1	$5 \times 10^{-6}$	$9 \times 10^{-5}$	0.007	N/A	$2 \times 10^{-4}$	0.08
$h_0(R_*)$	0.015	$5 \times 10^{-4}$	0.008	0.0075	N/A	0.0125	0.01
$h_{100\text{AU}}(\text{AU})$	15.57	0.516	9.26	7.89	N/A	12.98	12.11
Large Grains							
Mass Fraction	0	0	0	0	N/A	0	0
$h_0(R_*)$	0	0	0.0085	0	N/A	0	0
$h_{100\text{AU}}(\text{AU})$	0	0	9.83	0	N/A	0	0
Outer Disk							
Radius (AU)	10-200	8.5-200	4.5-200	20.5-300	0-200	15-200	4-200
Small Grains							
Mass Fraction	0.3	0.01	0.05	0.008	0.015	$5 \times 10^{-4}$	0.01
$h_0(R_*)$	0.009	0.01	0.007	0.015	0.006	0.013	0.0135
$h_{100\text{AU}}(\text{AU})$	9.34	10.31	8.1	15.79	6.8	13.49	16.35
Large Grains							
Mass Fraction	0.6	0.989495	0.94991	0.984	0.985	0.9993	0.91
$h_0(R_*)$	0.005	0.01	0.0085	0.0075	0.0045	0.005	0.006
$h_{100\text{AU}}(\text{AU})$	5.19	10.31	9.83	7.89	5.1	5.19	7.26

**Table 7.** Summary of model parameters derived throughout chapter 3.

	$\chi_M^2$	$\chi_H^2$
AA Tau	8.5	175.6
CoKu Tau/4	11.2	60.9
DM Tau	0.06	0.39
GM Aur	3.1	8.1
GO Tau	4.4	58.3
LkCa15	17.6	190
TW Hydra	4.1	34.8

**Table 8.** Summary of  $\chi^2$  results described throughout chapter 3.



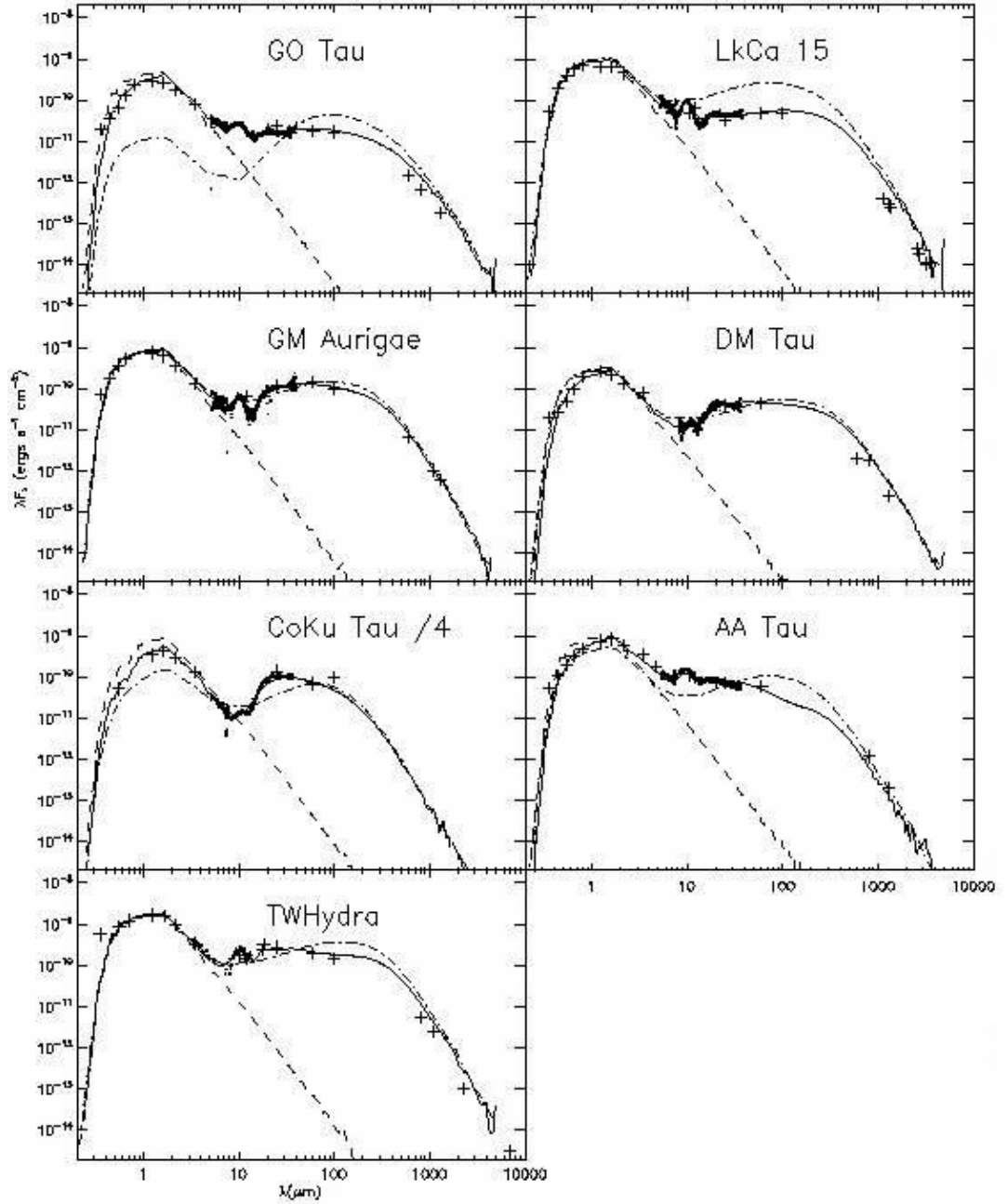


**Figure 3.27** Model SEDs of the sources investigated in this chapter. Solid lines are multiple dust species models, dot-dashed lines are HSEQ models and dashed lines are the stellar emission. The crosses mark IRAS data and the dots mark SPITZER IRS data.

Comparison with similar models for some of these sources (Calvet et al. 2005, Furlan et al. 2006 and D’Alessio et al. 2006) shows agreement in the overall conclusions as to the cause of features present in the observational data. These are not unique fits but as better, higher resolution data becomes available it will be possible to further constrain the dust types and particle sizes present at different locations throughout the disk and improve the model results.

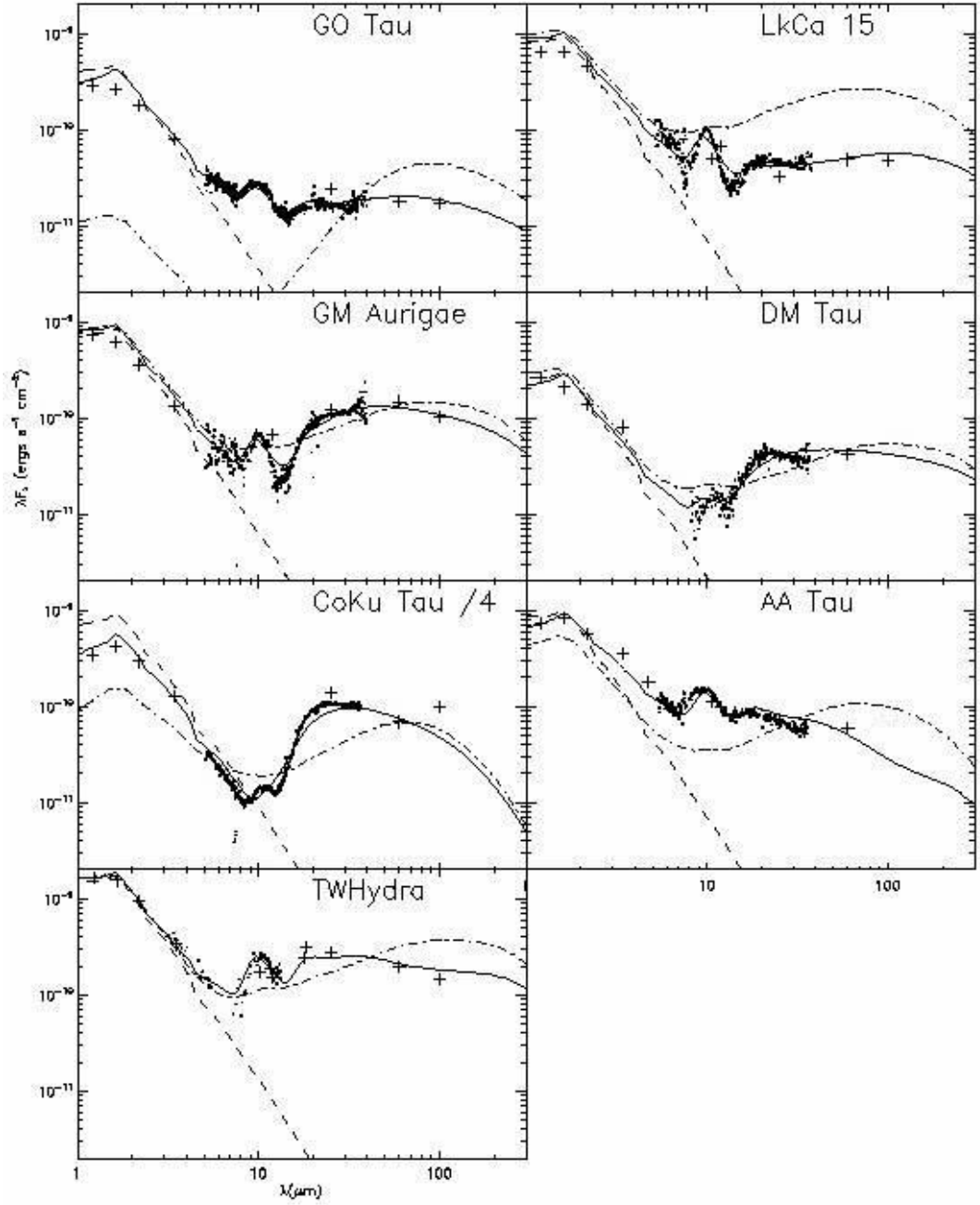


**Figure 3.28** Close-ups of the model SEDs developed in this chapter focusing on the near-IR region of the SED. Solid lines are multiple dust species models, dot-dashed lines are HSEQ models and dashed lines are the stellar emission. The crosses mark IRAS data and the dots mark SPITZER IRS data.

## **4. Non – LTE Molecular Line Transitions**

### **4.1 Introduction**

Observations at (sub) millimetre and infrared wavelengths provide astronomers with an indispensable tool in determining the physical parameters of circumstellar disks. The mass and rotational velocities of the disks along with the mass of the central source can all be found from analysis of spectral energy distributions in this region of the spectrum. The most commonly studied molecular species found in the dusty material orbiting in circumstellar disks are CO and  $\text{HCO}^+$  and it is generally the transitions of these species which are modelled and compared with observations in order to interpret and understand the physical processes in the disks.

The low densities found in many regions of circumstellar and molecular cloud environments mean that the excitation of many molecules is out of Local Thermodynamic Equilibrium (LTE) and the transition line emission is important in the determination of the molecular excitation (Leung & Liszt 1976). In order to simulate the radiation emitted during the line transitions of molecules in these environments a procedure for the solution of non-LTE, multi-level, radiation transfer problems must be implemented. Just such a procedure was developed by Bernes (1979) for application to CO line transitions in a spherically symmetric, collapsing dark cloud. The Bernes code was one-dimensional and as such it is limited in the extent to which it can take account of the complex density structures, both observed and theorised, discussed throughout this work. The high spatial resolution of current and future instruments will require at least a two-dimensional treatment like that developed by Park & Hong (1995), Juvela (1997) and Hogerheijde & van der Tak (2000).

Throughout the rest of this chapter I will briefly describe Bernes' original 1D model and my modification and expansion of it to a fully 3D simulation. Test comparisons with the results of the original program will be made at each stage before moving on to the application of my new 3D NLTE code to circumstellar disks in the following chapter.

### **4.2 The Bernes Model and its Expansion to 3D**

In 1979 Bernes presented a Monte Carlo approach for solving non-LTE radiative transfer problems and applied it to a spherically symmetric 1D treatment of a collapsing dark molecular cloud. I will briefly describe the basic procedure followed by the Bernes simulation here.

The spherical region of the radiation transfer simulation is divided into a number of radial shells in such a way that the density and temperature is constant throughout the shells. A number of model photons each representing a large number of real photons is emitted isotropically from each shell and followed through the simulated region until they leave the grid or their weight is very small. The number of absorption events caused by the radiation is stored, as are the number of stimulated emissions that take place. The weighting of the model photons is continuously modified in order to account for these absorptions and emissions. Once all the photons have been followed the total number of absorption events is used to derive new level populations and the whole process is repeated until convergence is reached and the level populations settle to constant values.

The level populations are governed by excitation and de-excitation from collisions, CO line emission and Cosmic Microwave Background emission, CMB. In these simulations stellar radiation and dust emission are not considered but these can easily be included. The effects of the central star emitting as a black body at some temperature with a fraction of its emission coinciding with the excitation energy of the CO molecule can be simulated in much the same way as it is for the radiation transfer models described earlier and the effects of dust emission and absorption can be included.

Photons are emitted through excitations to the upper energy level followed by spontaneous radiative de-excitations and the number,  $N_r$ , of these emissions per second per unit volume is

$$N_r = n_u A_{ul} \quad (4.1)$$

where  $A_{ul}$  is the Einstein probability for spontaneous emission and  $n_u$  is the upper level population. The initial level population values in the Bernes code are a partly converged estimate obtained during the initial testing of his code after only a few iterations. These are then used to reduce the number of iterations required and speed up the simulation when running it in its finished form. When expanding the model to 3D and applying it to different geometries it would no longer be possible to use Bernes' pre-determined level populations so an initial value based on the fraction of CO molecules in the simulation spread evenly throughout the energy levels is used

$$n_{pop} = \rho_n / f \times N_{lev} \quad (4.2)$$

where  $\rho_n$  is the number density of particles in a certain cell,  $f$  is the fraction of CO molecules and  $N_{lev}$  is the number of energy levels being considered in the simulation. It

would also be possible to use level populations derived for a LTE disk as an initial starting value.

Each model photon is emitted in a random direction, represented by the unit vector  $\mathbf{n}$ , and has a random frequency deviation,  $\Delta\nu$ , from line centre,  $\nu$ . The distribution of emission directions is isotropic and the frequency distribution is defined using the normalised Doppler profile

$$\phi(\nu) = \frac{1}{\sigma\sqrt{\pi}} \exp \left[ - \frac{\left( \nu - \nu_{ul} - \mathbf{v} \cdot \mathbf{n} \frac{\nu_{ul}}{c} \right)^2}{\sigma^2} \right] \quad (4.3)$$

The Doppler width,  $\sigma$ , is determined by the local kinetic temperature and the frequency of the actual line centre can be shifted from  $\nu_{ul}$  by a velocity field specified by the vector  $\mathbf{v}$ .

The emitted photons travel a short distance,  $s_l$ , in the direction  $\mathbf{n}$  and the optical depth along this path is found from

$$\tau_1 = \frac{h \nu_{ul}}{4\pi} \phi(\nu) (n_{l,m} B_{lu} - n_{u,m} B_{ul}) s_1 \quad (4.4)$$

where  $n_{l,m}$  and  $n_{u,m}$  are the level populations in the shell  $m$ .  $B_{lu}$  and  $B_{ul}$  are the Einstein probabilities for stimulated absorption and emission respectively. The maximum distance that the emitted photons can travel is a constant in the Bernes code set so that at any radius the change in  $\mathbf{v}(\mathbf{r}) \cos \mu$  cannot be larger than 10% of the Doppler velocity width, where  $\mu$  is the angle between the direction of the photon and the outward radial direction. If the photon were to travel further than this distance the molecules it next interacted with would have a very different velocity than the molecules in the initial position, so the photon would not be absorbed in the new position and the absorption term would be underestimated. Another way to overcome this problem of preventing the photon travelling too far occurs quite naturally when converting Bernes' model to 3D. In a 3D model the radial velocity has to be expressed in terms of its  $x$ ,  $y$ ,  $z$  components and cannot be treated in the simple way it is in Bernes 1D model:

$$\mathbf{V} = a\mathbf{x} + b\mathbf{x} \times \mathbf{r} \quad (4.5)$$

where  $a\mathbf{x}$  and  $b\mathbf{x} \times \mathbf{r}$  are constants in the linear velocity field. The simplest way to do this is to discretise the velocity so that each cell in the simulation has a velocity consisting of an  $x$ ,  $y$ ,  $z$  component so the velocity is assumed constant inside each individual cell. In order to prevent errors occurring when the photon moves between cells it cannot move

further than the opposite edge of the cell it's travelling through in one step. This also means that the photon cannot travel across a large change in velocity and so the above problem is solved automatically. With this approach it is the grid which defines the resolution. So in order to resolve the velocity structure we need a fine grid structure.

In the Bernes model the background radiation photons are redefined relative to a uniform reference field for each transition. This procedure is employed in order to reduce the noise inherent in the Monte Carlo method but relies on setting the temperature of the reference field so that it is similar to the excitation temperature for each transition. For a region that is not isothermal like the molecular cloud modelled by Bernes this is impractical as the excitation conditions change substantially with radius (Crosas & Menten, 1997). The reference field is, consequently, removed from my expanded 3D model and the improved reduction in noise can be achieved by using a larger number of model photons. This method does not pose the problems of long computation times Bernes was trying to avoid as the computers available today are many times faster than those available in 1979.

Once all the photons have been emitted and tracked through the region the level populations in each cell are adjusted using the equation of statistical equilibrium:

$$n_l \left\{ \frac{B_{lu}}{4\pi} \oint \int_0^\infty I(\nu, n) \phi(\nu) d\nu d\omega + C_{lu} \right\} = n_u \left\{ A_{ul} + \frac{B_{ul}}{4\pi} \oint \int_0^\infty I(\nu, n) \phi(\nu) d\nu d\omega + C_{ul} \right\} \quad (4.6)$$

$C_{lu}$  and  $C_{ul}$  are the collisional excitation and de-excitation rates respectively and  $I(\nu, n)$  is the specific intensity at frequency  $\nu$  in the direction  $n$ . The term on the left hand side is the number of absorptions per atom or the number of radiation induced excitations and is stored in the counters for each cell. The right hand side is the rate of radiation induced de-excitations (stimulated emissions). The first term in the brackets on the left hand side of equation (4.6) is the rate of absorptions per atom in the lower state and as mentioned earlier has accumulated in the counters  $\sum S_{lu,m}$  for each shell,  $m$ , in Bernes's model but each cell in my 3D model. Similarly the second term inside the brackets on the right hand side of equation (4.6) is the rate of radiation induced de-excitations and since

$$g_l B_{lu} = g_u B_{ul}$$

where  $g_l$  and  $g_u$  are the statistical weights of the two levels this second term can be substituted and equation (4.6) simplifies to

$$n_l \left\{ \sum S_{lu,m} + C_{lu} \right\} = n_u \left\{ A_{ul} + \frac{g_l}{g_u} \sum S_{lu,m} + C_{ul} \right\} \quad (4.7)$$

which can be solved using the condition that  $n_l + n_u = \text{constant}$ . The new values of  $n_u$  are used to revise the value of  $N_r$  in equation (4.1) for each cell as the model moves towards convergence. My 3D NLTE code uses Bernes algorithm and inversion routine for solving the statistical equilibrium equation, expanded to operate on the arrays generated by a 3D grid as opposed to a 1D radial grid.

After all the iterations are complete and the level populations have converged the emitted spectrum can be calculated. The intensity  $I_{em}(\nu)$  of the emitted radiation along a ray through the grid is

$$I_{em}(\nu) = I_{bg}(\nu) \exp\{-\tau(X)\} + \int_0^X j(\nu, x) \exp\{-\tau(x)\} dx \quad (4.8)$$

$I_{bg}(\nu)$  is the specific intensity of the background radiation,  $\tau(x)$  is the optical depth from the near surface of the region to the position  $x$  along the ray path with  $X$  marking the position where the ray leaves the region on the far side. By following a number of rays through the region a channel map of the emitted radiation can be constructed and the line profile of the region can be obtained by plotting the integrated intensity distribution.

### 4.3 Comparison with Bernes Non-LTE Radiative Transfer Program

In order to test my 3D Monte Carlo code I compared it to the original 1D code produced by Bernes (1979). In this paper Bernes presented a constant density, constant temperature, cloud model so it is this that I reproduce in the following sections, first in 1D and then in 3D. Reproducing these well documented results is an essential test of the codes ability to correctly determine and represent Non-LTE Molecular Line Transitions.

#### 4.3.1 1D comparison

I have expanded and modified the Bernes method of solving Non-LTE Molecular Line Transitions as described in section 4.2 so that it can be applied to a 3D spherical polar grid and any geometry that I wish to study. To test that my code reproduces the Bernes results in 1D I set up the grid so that it has the same number of radial cells (size and location) and an analytic radial velocity as in the Bernes simulation but uses only one  $\theta$  and one  $\phi$  cell so is effectively 1 dimensional.

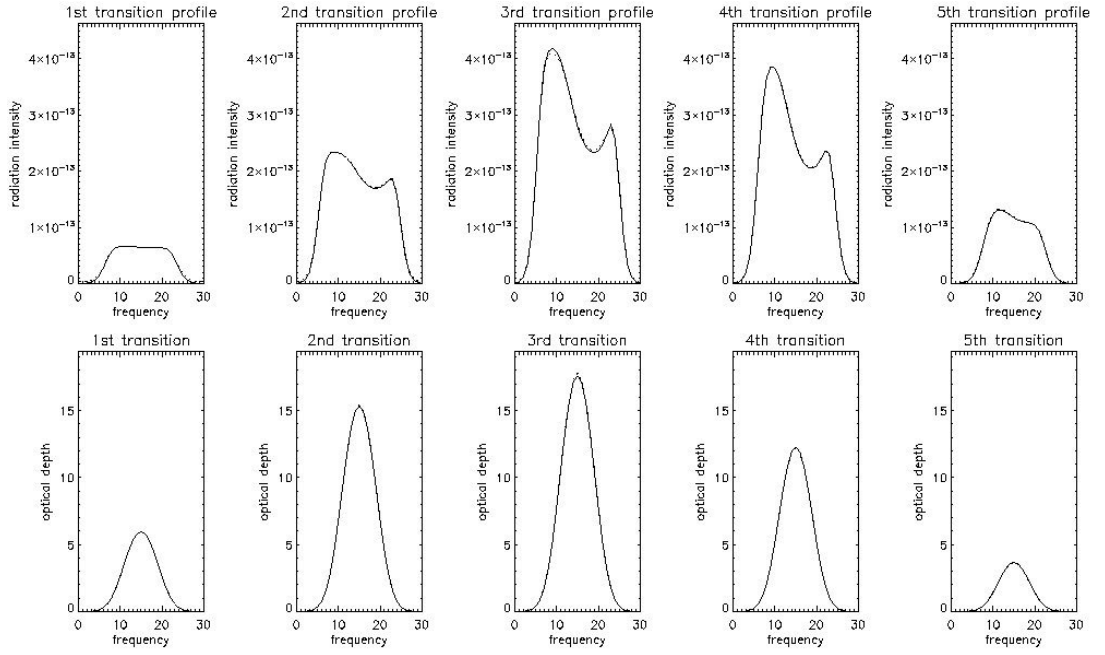


**Figure 4.1** Comparison of Bernes 1D results (dotted line) with my 3D code restricted to 1D (solid line). Plot shows the line profiles and optical depths for the first five transitions of the CO molecule along a ray passing through the centre of the simulated region.

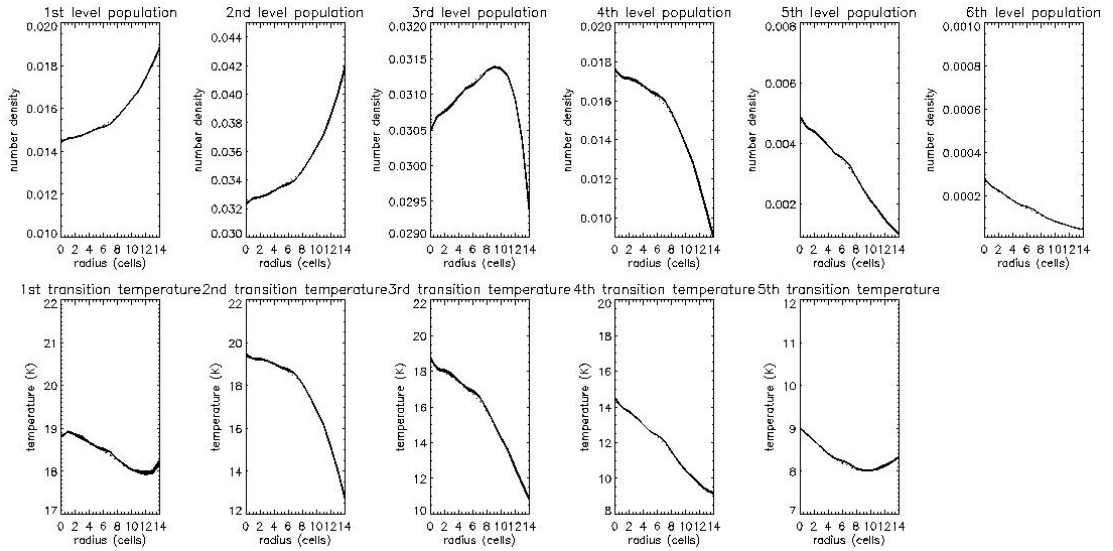
Figure 4.1 shows the line profiles for transitions between the first six energy levels of the CO molecule, transitions  $J=1-0$ ,  $2-1$ ,  $3-2$ ,  $4-3$  and  $5-4$ . The profiles are those for a line of sight passing close to the centre of the simulated molecular cloud.

Figure 4.2 shows the radial variation of the converged level populations and excitation temperatures of the two models after the final iteration is complete. Both figures 4.1 and 4.2 show the results of the original Bernes model and my model run with the same parameters and initial conditions as the Bernes model (cloud parameters shown in table 9). It can be seen that my modified Monte Carlo code, restricted to operating in only 1D, reproduces the Bernes results and an inspection by eye reveals no discernable differences.

$n(\text{cm}^{-3})$	$X_{\text{CO}}$	$T(\text{K})$	$V(r)(\text{km s}^{-1})$	$a$	$b$	$V_{\text{turb}}(\text{km s}^{-1})$	$R_{\text{min}}(\text{AU})$	$R_{\text{max}}(\text{AU})$
2000	$5 \times 10^{-5}$	20	$ax+bx \times r$	0	$-3.33 \times 10^{-19}$	1		200,000

**Table 9.** Cloud parameters used in Bernes model.





**Figure 4.2** Level populations and excitation temperature comparison between the original Bernes 1D model (dotted line) and my 3D model restricted to 1D (solid lines). Plots show the radial variation of the level populations for each of the first six energy levels of the CO molecule and the excitation temperatures for the corresponding transitions.

### 4.3.2 3D comparison

The comparison of my models results when using a 3D spherical polar grid with the original Bernes results is a much more rigorous test due to some of the alterations that were necessary. When running my model in it's fully 3D form it was necessary to use a discretised velocity function as mentioned in section 4.2 so that the radial velocity could be expressed correctly in its x, y, z components. The discretised velocity will also make it simpler to use more complex or predetermined velocity descriptions in future models and so it is vitally important that it can reproduce the original results.

Figures 4.3 and 4.4 show the original Bernes 1D model along with my fully 3D model. In this case I have used Bernes initial level populations and radial grid and effectively replicated it round  $\theta$  and  $\phi$ . The models agree to within 0.2% indicating that not only am I able to reproduce the 1D model with my 3D code but also that the effect of discretising the velocity is minimal. For simulations with many more grid cells and emitted photons than the original Bernes simulation the accuracy of the reproduction will only improve as the velocity distribution is sampled at more regular intervals. In my model I emitted ten times the number of photons from each cell as Bernes used in his 1D simulation, this causes a large increase in computing time but the actual run time is still very short. The original Bernes code, running 200 photons per shell, with 15 shells and converging after 40 iterations takes 0.37 seconds to complete on a modern

1.5GHz CPU. My 3D grid consisting of (15,5,5) cells, emitting 2000 photons per cell for the same 40 iterations completes after 5.36 seconds.

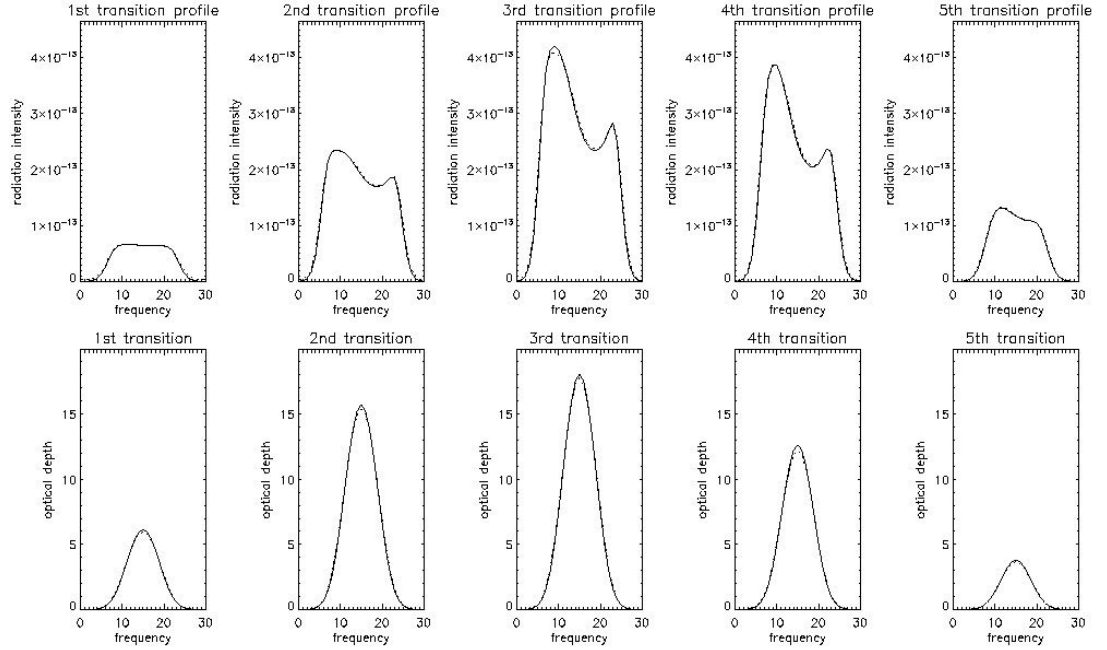


**Figure 4.3** Comparison of Bernes 1D results (dotted line) with my 3D code (solid line). Plot shows the line profiles and optical depths for the first five transitions of the CO molecule along a ray passing through the centre of the simulated region. My model uses Bernes radial grid and initial level populations.

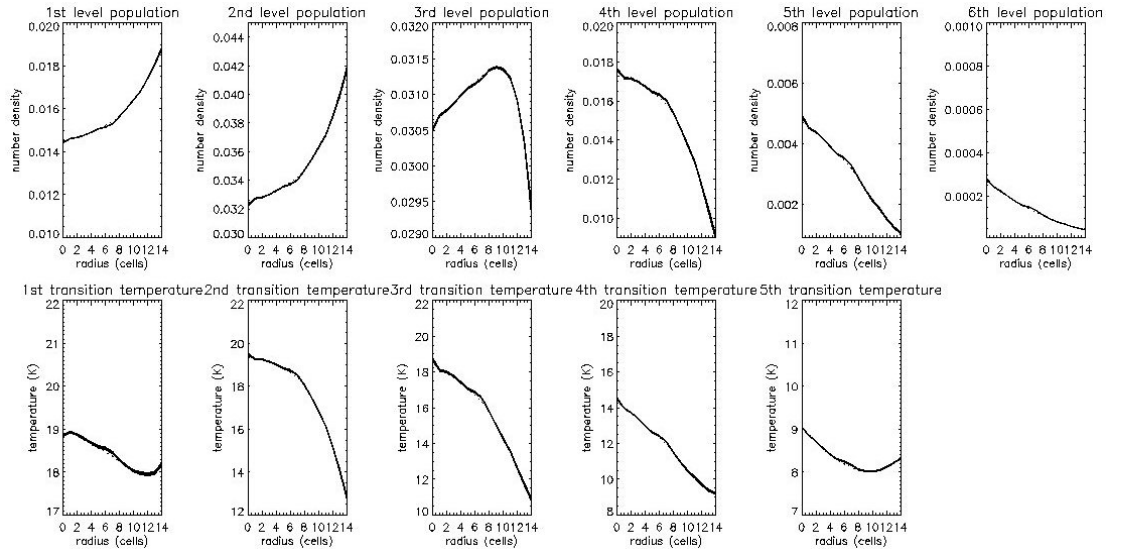


**Figure 4.4** Level populations and excitation temperature comparison between the original Bernes 1D model (dotted line) and my 3D model (solid lines). Plots show the radial variation of the level populations for each of the first six energy levels of the CO molecule and the excitation temperatures for the corresponding transitions. My model uses Bernes radial grid and initial level populations.

Applying the code to other environments than the spherical molecular cloud modelled by Bernes will mean that the predetermined, partly converged level populations that Bernes uses as his initial population values will be inaccurate. In order to provide a reasonable set of initial populations from which to begin the iterations I use equation (4.2) described in section 4.2. Using a set of values that are not partially converged requires my model to calculate several more iterations to reach convergence but with the faster computers available today this doesn't significantly increase the computation time.

The original Bernes model uses a radial grid specifically tailored to provide cells of the same volume and density with finer sampling in the outer regions to resolve the temperature there. These are set up from prior knowledge of the region. In order to apply my model to a range of environments and geometries I am able to set up my radial grid so that it can take any form. For the purposes of this example I have set up the radial grid using equation (4.9) and have distributed the radial cells uniformly throughout.

$$r(i) = r_{\min} + (r_{\max} - r_{\min}) \left( \frac{(i-2)}{(nrg-1)} \right) \quad (4.9)$$

where  $i$  denotes the cell number and  $nrg$  is the number of radial cells.

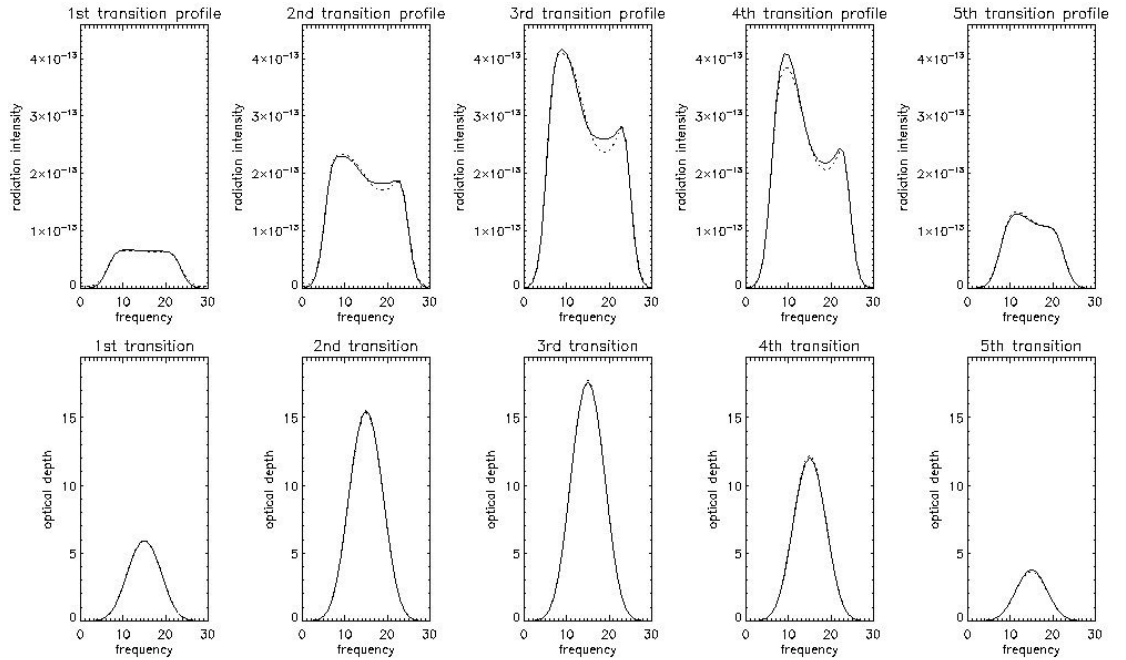


**Figure 4.5** Comparison of Bernes 1D results (dotted line) with my 3D code (solid line). Plot shows the line profiles and optical depths for the first five transitions of the CO molecule along a ray passing through the centre of the simulated region. My model uses my radial grid and initial level populations.

The resultant line profile generated from my independent 3D model with a general radial grid structure, discretised velocity and initial level populations is shown in Figure 4.5 and compared with Bernes' 1D result. Bernes' radial grid is finer in the outer regions of the cloud than my uniform grid and this is the reason for the slight difference between the two results.

#### **4.4 Conclusion**

In this section I have shown that my modified and extended version of Bernes Non-LTE Molecular Line Transition code reproduces the original line profiles and level populations in 1D. On expansion to a fully 3D spherical polar grid my model again reproduces the Bernes results using Bernes initial conditions and radial grid. When I apply a more general grid structure and initial level populations I can reproduce the Bernes results very accurately with only a minor departure due to the slightly altered grid structure throughout my grid. Having verified the accuracy and validity of my model it can now be applied to the more complex geometries found in the environments of YSOs which will be discussed in the next chapter.

## **5. Application of Non – LTE Molecular Line Transition code to Circumstellar Disks**

### **5.1 Introduction**

The development of a fully 3D Monte Carlo Radiation Transfer model of Non-LTE Molecular Line Transitions allows the investigation of the velocity and density structures of CTTS. With new observations of massive (self-gravitating) disks (Rodriguez et al. 2005 & Eisner et al 2005) and the Atacama Large Millimetre Array (ALMA) being constructed in Chile we have the opportunity to investigate the dynamical processes in CTTS and obtain much more detailed information about the internal structure of these disks than through conventional SEDs. At optical wavelengths the circumstellar disks interior is obscured and very little information on its temperature and density structure can be obtained (Qi et al. 2003). At millimetre wavelengths the thermal emission of the disk becomes optically thin allowing us to probe the density, temperature and velocity structure of these objects. Studies like those of Rice et al. (2004, 2005 & 2006) and Lodato & Rice (2005) are currently developing Smooth Particle Hydrodynamics (SPH) models of self gravitating massive disks and it is the observational signatures of these models that can be simulated with a 3D, Non-LTE Molecular Transition code making it a useful tool in bridging the gap between theory and observation.

Investigating the density and velocity structure of the disk allows better estimates of its mass and radial extent. Knowledge of the disks temperature structure can provide information on the size and chemical properties of the disks constituents and on the processes that may be ongoing at different stages of the disks evolution. All of this is of great interest for understanding how these disks make the transition from collapsing cloud core through the T Tauri phase to the planetary system stage like our own solar system.

### **5.2 CO Emission from LkCa15**

The T Tauri source LkCa15 is becoming one of the best studied sources at millimetre wavelengths and has a substantial IR excess (Strom et al. 1989, Simon et al. 2001 & Chiang et al. 2001). I have discussed this source previously in section 3.4.6 when I investigated the extent of dust settling and grain growth that was present in its circumstellar disk. The millimetre emission from this source has been probed by Simon

et al. (2001) who found that it may extend out to a radius of as much as 650 AU. This is much larger than the 430AU disk found by Qi et al. (2003) discussed below and larger again than the 200AU disk modelled in chapter 3.4.6. Much of the emission in the SED is produced by the warmer, surface material of the disk emitting at shorter wavelengths and it is no surprise that a study at longer wavelengths can detect observable emission at larger radii where the material is much cooler. There is obviously still some discrepancy between the millimetre studies of Simon et al. (2001) and Qi et al. (2003) and further observation is required to refine the estimate of the disk's radius. A recent paper by Hughes et al. (2008) investigates similar outer disk radii discrepancies found in HD163296, TW Hydrae, GM Aurigae and MWC 480 and describes a way to taper the exponential surface density distribution at the outer edge in order to reproduce the much larger radii observed in both gas and dust emission.

The investigation by Qi et al. (2003) concentrated on emission from abundant species, CO and  $\text{HCO}^+$ . They used the Owens Valley Radio Observatory (OVRO) Millimetre Array to observe the circumstellar disk of LkCa15 with a beam FWHM resolution of  $(4.4'' \pm 0.4'') \times (3.6'' \pm 0.3'')$ . They used a 2D Monte Carlo model (Hogerheijde & van der Tak, 2000) to examine the radiative transfer and molecular excitation in the disk, taking both collisional and radiative processes into account. They find that a disk stretching from 5 - 430AU with a mass of  $0.01M_{\odot}$  and at an inclination of  $58^{\circ}$  reproduces the observed line profile and channel maps well, figures 5.1 and 5.4 respectively.

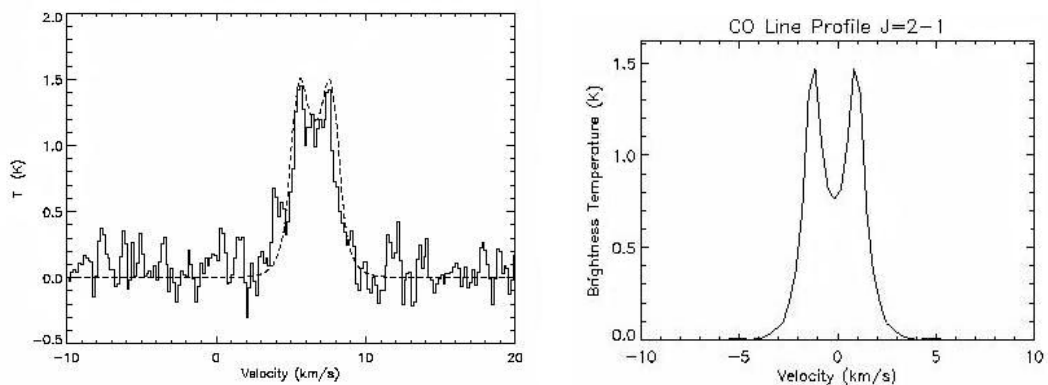


**Figure 5.1** Model fit to the observed LkCa15 line profile taken from Qi et al. (2003) on the left. Solid line is the disk averaged spectrum for the J=2-1 transition of the CO molecule and the dashed line is their models results. On the right is my result for the same disk parameters.

Application of my 3D Monte Carlo model to this system using the same disk parameters as Qi et al. (2003), the parameters are summarised in table 10, results in a reproduction of the Qi model (figure 5.1) with only a slight difference in the fractional abundance of CO compared to H<sub>2</sub>. Qi uses a fractional abundance of N<sub>2</sub> of  $4 \times 10^{-5}$  that of H<sub>2</sub> and estimates of the ratio of N<sub>2</sub>/CO from studies of comet tails and planetary nebulae (Bar-Nun, Kleinfeld & Kochavi, 1988; Wyckoff & Theobald, 1989; Lutz, Womack & Wagner, 1993; Owen & Bar-Nun, 1995) which give values of around 1 – 0.01, giving a fractional abundance for CO of around  $4 \times 10^{-7}$  that of H<sub>2</sub>. I use a fractional abundance for CO of  $2.5 \times 10^{-7}$  which is slightly less than that of Qi.

When we compare these disk parameters with the disk parameters I derived in section 3.4.6, a star of mass  $M_* = 0.5M_{\odot}$ , a disk of mass  $M_d = 0.0075M_{\odot}$  and outer radius of 200AU, we find they are considerably smaller than that of the Qi model. The warmer, surface material of the disk, emitting at shorter wavelengths is responsible for much of the emission in the SED so as previously stated it is unsurprising that a study at longer wavelengths can detect observable emission at larger radii where the material is much cooler. Another discrepancy is the inclination of the disk, I found an inclination of 35° provided the best fit to the SED and Qi et al. have used an inclination of 58°, but as discussed in section 3.3 there is very little effect on the SED once a star is revealed for  $i \leq 75^\circ$ .

Object	Spectral Type	T <sub>eff</sub> (k)	R <sub>*</sub> (R <sub>⊙</sub> )	M <sub>*</sub> (M <sub>⊙</sub> )	M <sub>d</sub> (M <sub>⊙</sub> )	R <sub>d</sub> (AU)	Inc.
LkCa15	K5	4000	1.85	0.9	0.01	5 - 430	58°

**Table 10.** Stellar and disk parameters of LkCa15 model used by Qi et al. (2003).

Figure 5.1 shows the line profiles generated by the Qi model and my model compared with the observed line profiles of LkCa15 for the J=2-1 transition of the CO molecule. My model not only replicates this transition but the transitions between the first five rotational energy levels of the CO molecule and these are plotted in figure 5.2 as a function of brightness temperature against velocity. The most notable departure from the Qi model is the more pronounced dip at velocities of around 0km s<sup>-1</sup>. This indicates that the material in my model moving most slowly (probably at the outer reaches of the disk) has a lower brightness temperature and this could be caused by the material in these regions being more diffuse or by a difference in the disk flaring so that the

material presents a smaller surface area to incident stellar radiation and so re-emits less brightly.

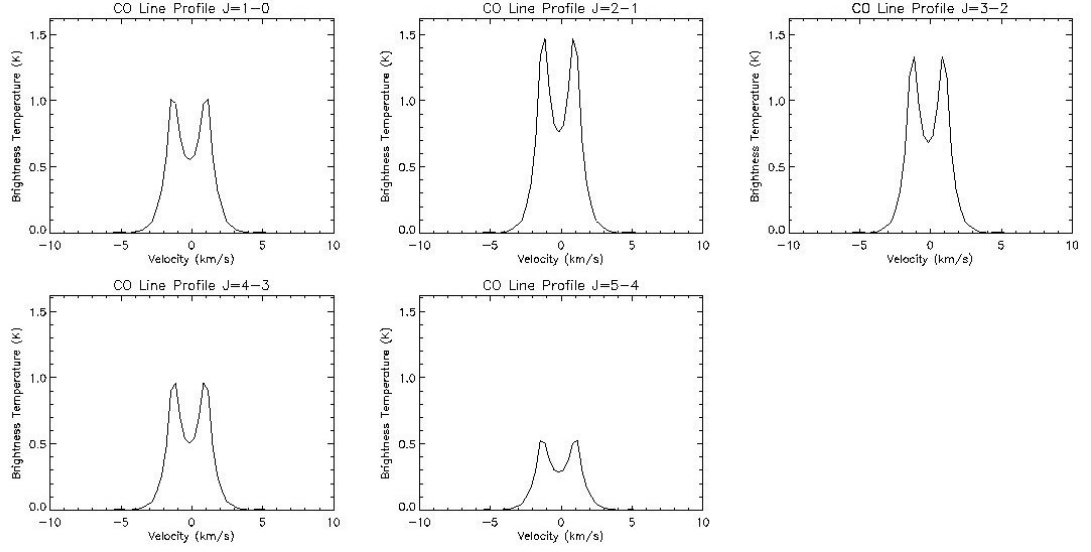


**Figure 5.2** Model line profiles of LkCa15 for transitions between the first six rotational energy levels of the CO molecule.

The circumstellar gas emission is an effective tracer of the line-of-sight velocity component of the disk via Doppler shifts. This can be used to determine the line-of-sight velocity of different parts of the disk and displayed as contour plots at a range of velocities, approaching and receding.

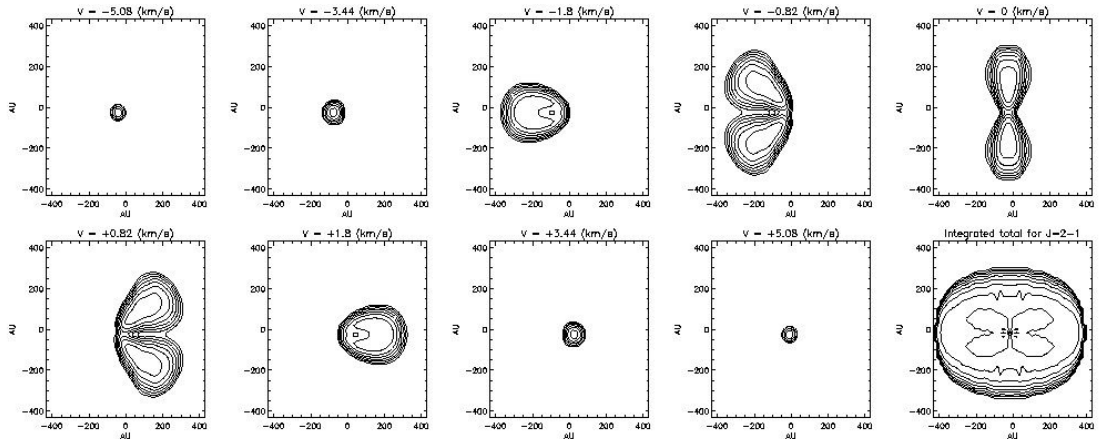


**Figure 5.3** Contour maps of the J=2-1 model CO emission from LkCa15 at a range of velocities plus the total integrated emission over the Doppler line-width, lower right panel. Images are 860AU on a side.

Figure 5.3 shows contour plots of channel maps at a range of velocities generated by my 3D model using the Qi parameters for the LkCa15 disk with a Keplerian rotation. Figure



5.4 shows a comparison between the observed spectral emission and that generated by Qi's 2D model. Both models generate similar images and shapes, although the Qi model is oriented like the source appears on the sky and has been convolved with a larger FWHM gaussian.

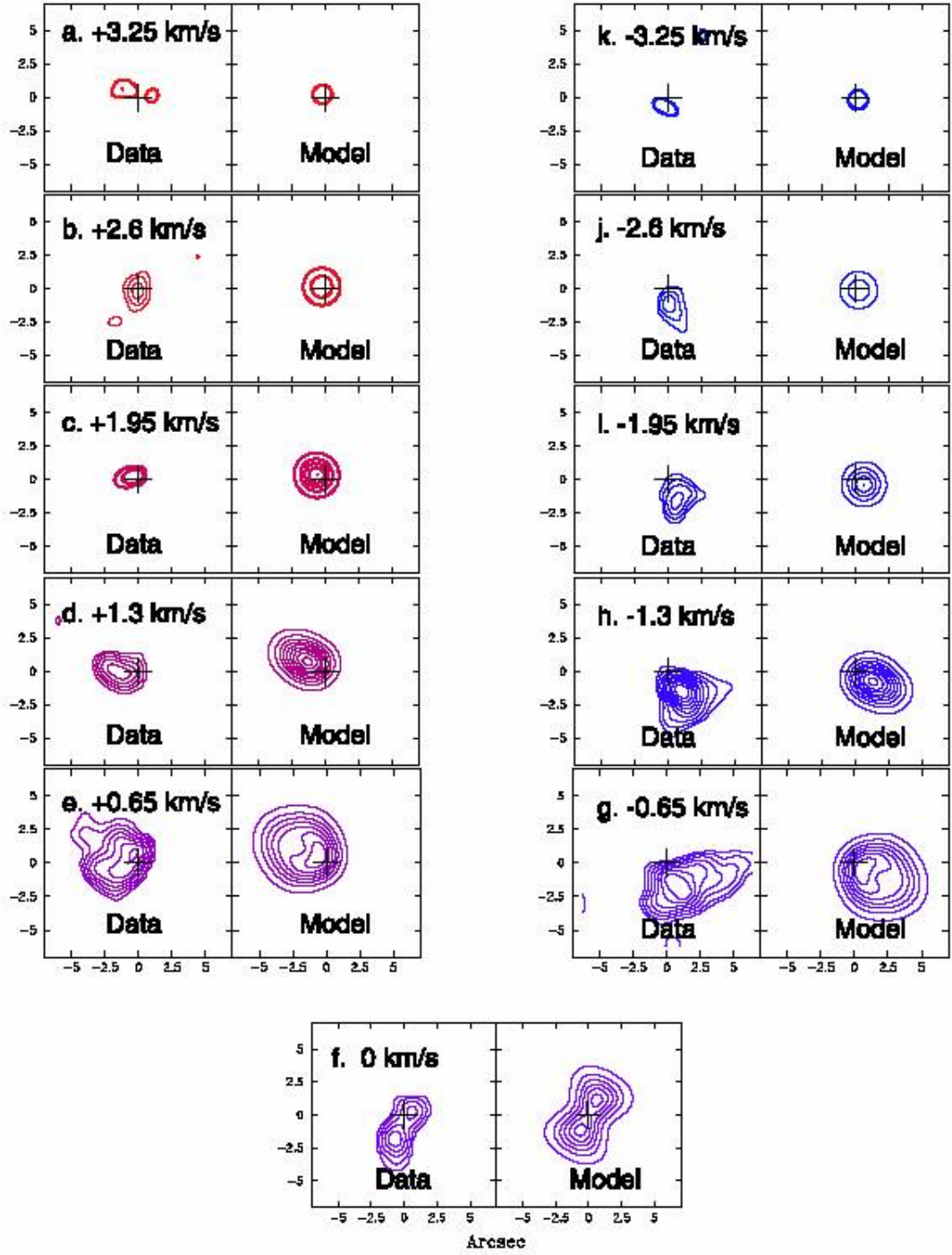


**Figure 5.4** Contour maps of LkCa15's J=2-1 CO emission in steps of  $0.65 \text{ km s}^{-1}$  shown adjacent to simulations of the emission predicted using a Keplerian rotation, taken from Qi et al. (2003). The colour coding matches the Doppler shift of the line-of-sight component of the disks velocity.

Reproducing Qi's 2D model and observational data of LkCa15 has tested the model's ability to handle the very different geometries of YSOs with circumstellar disks. It is not just able to reproduce 1D collapsing molecular clouds as shown in the previous chapter but it is able to operate with more complex density and temperature structures and a Keplerian rotational velocity distribution. Further 2D tests are desirable but there are currently no 2D tests presented in the literature. We are planning 2D test cases of disk models with Hogerheijde and Dullemond to test the convergence of our level populations, excitation temperatures and our predicted line profiles.

### 5.3 Investigating Dynamical Models of a Compact Massive Disk

The evolution of YSOs from class 0 to class III and the steady collapse of material towards the rotational midplane, described earlier in section 1.2, leads to the formation of circumstellar disks. In this scenario the disk would steadily grow in size as the material with progressively higher angular momentum falls in to the disk (Terebey et al. 1984; Ruden & Lin 1986; Lin & Pringle 1990). Until recently there has been very little known about the early stages of disk formation as the young disks are shrouded in the protostellar envelope of their parent star which is opaque to short and medium wavelengths. The 7mm systems developed on the VLA can observe right into the heart of these objects and with an angular resolution of  $0.07''$  are able to produce very detailed images of the circumstellar structure.

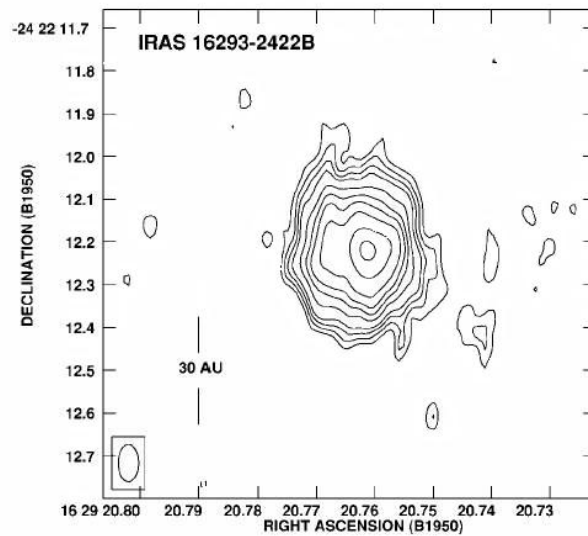


**Figure 5.5** VLA image at 7mm of IRAS 16293 – 2422B, the half – power contour of the synthesised beam ( $0.09'' \times 0.05''$ ) is shown in the bottom left. Image taken from Rodríguez et al. (2005).

A recent study by Rodríguez et al. (2005) reports the discovery of just such a compact circumstellar disk in the class 0 object IRAS 1693 – 2422B in the Ophiuchus molecular complex (shown in figure 5.5). They find that the disk has a maximum radius of only 26AU and estimate a mass in the range of  $0.3 - 0.4M_{\odot}$ . They find that the outer regions of this disk are gravitationally unstable and that the Toomre parameter,  $Q$ , lies in the range  $0.4 - 0.3$  which could be the origin of the disks non-axisymmetric structure (Rice et al. 2003b; Gammie 2001) and the hint of a spiral density structure that they detect. The Toomre parameter is a measure of gravitational stability with a disk being stable for values of  $Q \geq 1$ . The Toomre parameter is given by

$$Q = c_s \Omega_k / 2\pi G \Sigma \quad (5.1)$$

Where  $C_s$  is the sound speed in the disk midplane,  $\Omega_k$  is the angular momentum,  $\Sigma$  is the disk surface density and  $G$  is the gravitational constant.

Investigations into the density structure of massive circumstellar disks by Ken Rice using a SPH code have revealed instabilities that lead to the formation of a spiral density structure across the disk (Rice, Lodato & Armitage, 2004). The millimetre region of the spectrum is an ideal place to look for evidence of non-uniform density structures within circumstellar disks. The disks are optically thin at these wavelengths and variations on the velocity and density of material across the disk may be apparent here. With the next generation of millimetre telescopes set to come online in coming years bringing increased resolution, now is an excellent time to explore possible observational signatures of non-uniform structure in circumstellar disks.

To do this a disk with an initially smooth density and temperature distribution, given by equations 5.2 and 5.3 respectively, is allowed to evolve dynamically.

$$\Sigma(r) = \Sigma_0 \left( r/R_0 \right)^{-1} \quad (5.2)$$

$$T(r) = T_0 \left( r/R_0 \right)^{-1/2} \quad (5.3)$$

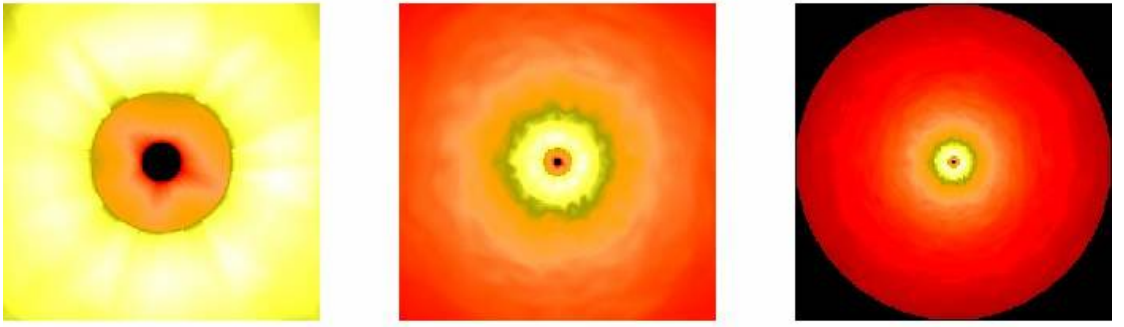
where  $\Sigma$  is the surface density,  $\Sigma_0$  and  $T_0$  are the surface density and temperature at  $R_0$  respectively.  $R_0$  is the radius of the inner edge of the circumstellar disk. The dynamical processes that the self gravitating disk undergoes over a number of orbits are simulated. The disk parameters required for equations 5.2 and 5.3 are chosen to ensure that the disk is gravitationally unstable, with a Toomre parameter of  $Q < 1$ , at its outer edge. Over

time a spiral density structure evolves in the disk and it is some signature of this that I aimed to identify with my 3D molecular line transition code. The parameters of the central source and disk used in the dynamical model are listed in table 11.

$M_*(M_\odot)$	$R_*(R_\odot)$	$T_{\text{eff}}(\text{K})$	$M_d(M_\odot)$	$R_{\text{min}}(\text{AU})$	$R_{\text{max}}(\text{AU})$
1	1.85	4000	0.25	0.25	25

**Table 11.** stellar and disk parameters for the dynamical disk model.

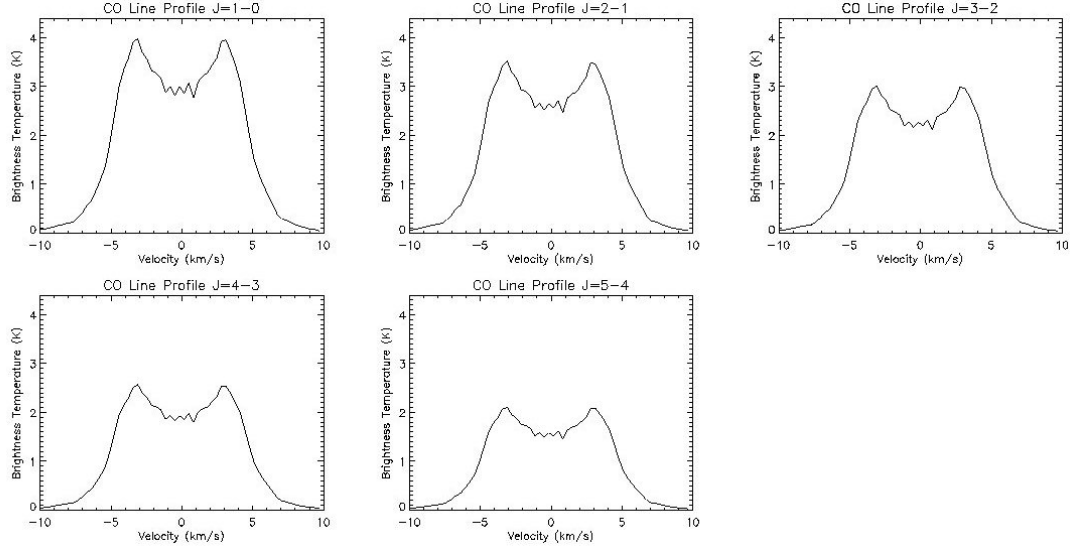
Figure 5.6 shows a face on view of the midplane of the smooth disk density distribution that was read into my molecular line transitions code. The model at this stage has a smoothly varying density similar to the flared disks with a power law density distribution I have modelled and described in previous chapters.



**Figure 5.6** Face on view showing midplane density of the smooth disk model, images are 4, 20 and 50AU on a side from left to right.

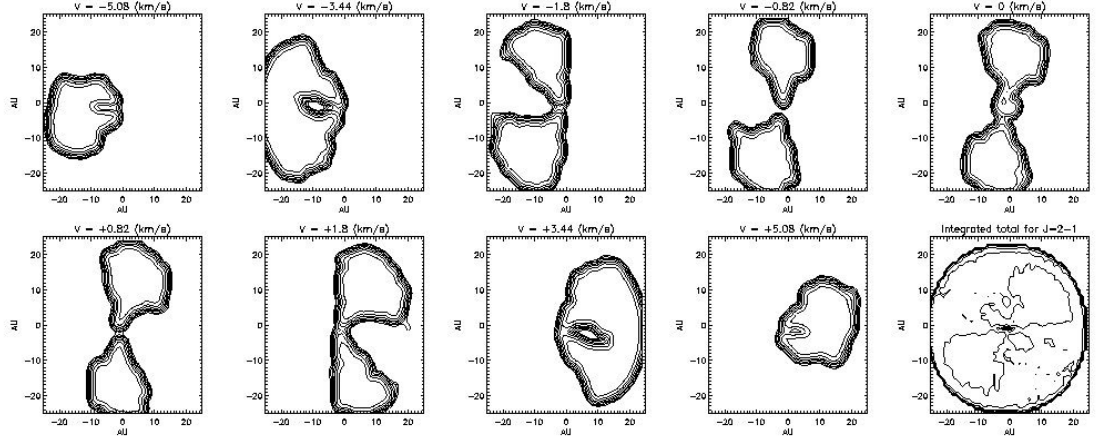
The velocity structure of the dynamical disk was also simulated by my molecular line transition code. A viewing angle of  $40^\circ$  was chosen so that there was no chance of the line-of-sight being obscured by the flared outer edge of the disk and that there would be a noticeable variation in the line-of-sight Doppler velocity of the rotating disk.

Figure 5.7 shows the resultant line profiles for the initial, smooth disk. They produce the familiar double peaked profile of a Keplerian disk with most of the emission concentrated across a wavelength range corresponding to velocities within  $6\text{-}7 \text{ km s}^{-1}$  of line centre.



**Figure 5.7** Line profiles of the initial, smooth dynamical disk, inclined at  $40^\circ$ , for transitions between the first six rotational energy levels of the CO molecule.

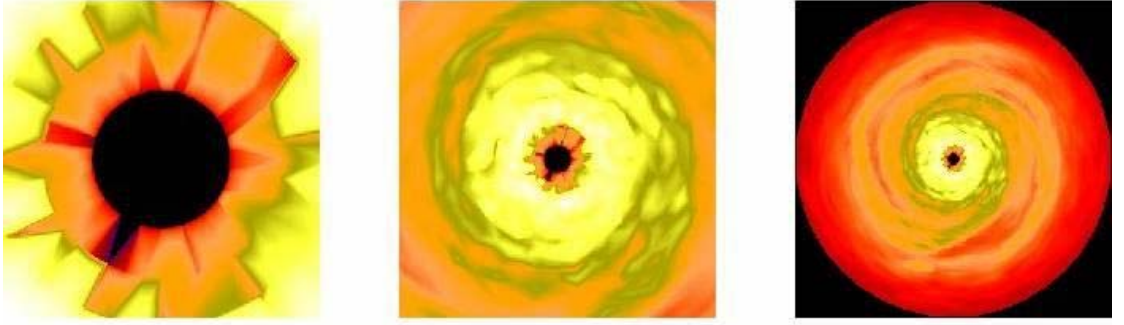
The corresponding contour maps of the  $J=2-1$  transition are shown in figure 5.8. They are fairly symmetrical about the disk midplane and about line centre as is to be expected in the case of a smoothly varying disk.



**Figure 5.8** Contour maps of the  $J=2-1$  CO emission for the smooth disk model across a range of velocities and at an inclination of  $40^\circ$ . Images are 100AU on a side and the lower right panel shows the total integrated emission over the Doppler line-width.

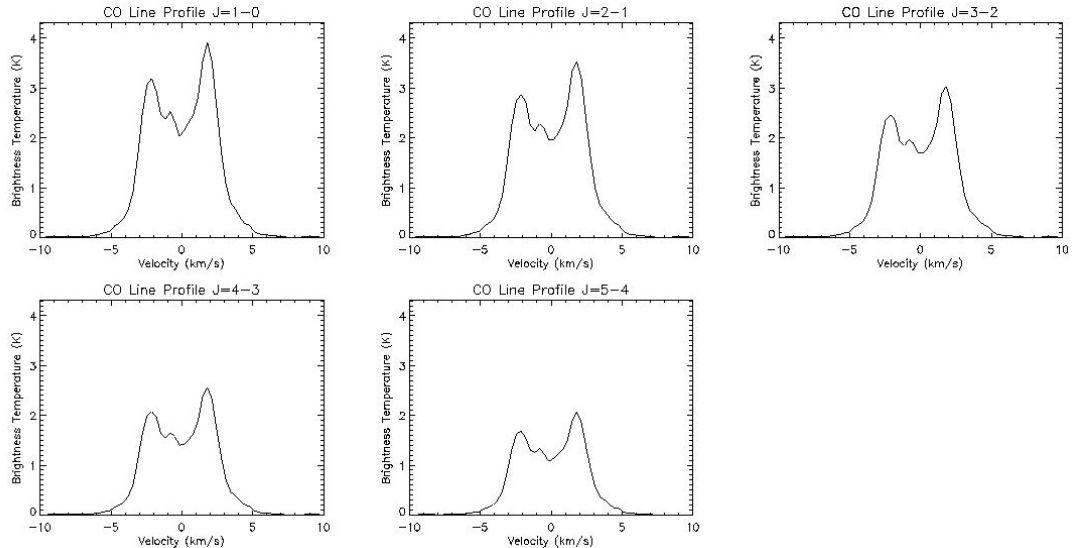
The time evolved spiral density distribution shown in figure 5.9 clearly shows a double armed spiral structure. This spiral structure produced an extra peak in the line profiles for the CO molecule transitions, shown in figure 5.10. This extra peak was most evident when the simulation was viewed from an inclination of  $20^\circ$  and an azimuth of  $60^\circ$  and

lies at only  $\pm 1 \text{ km s}^{-1}$  or so from line centre, indicating it is produced by a spiral arm in the outer regions of the disk.



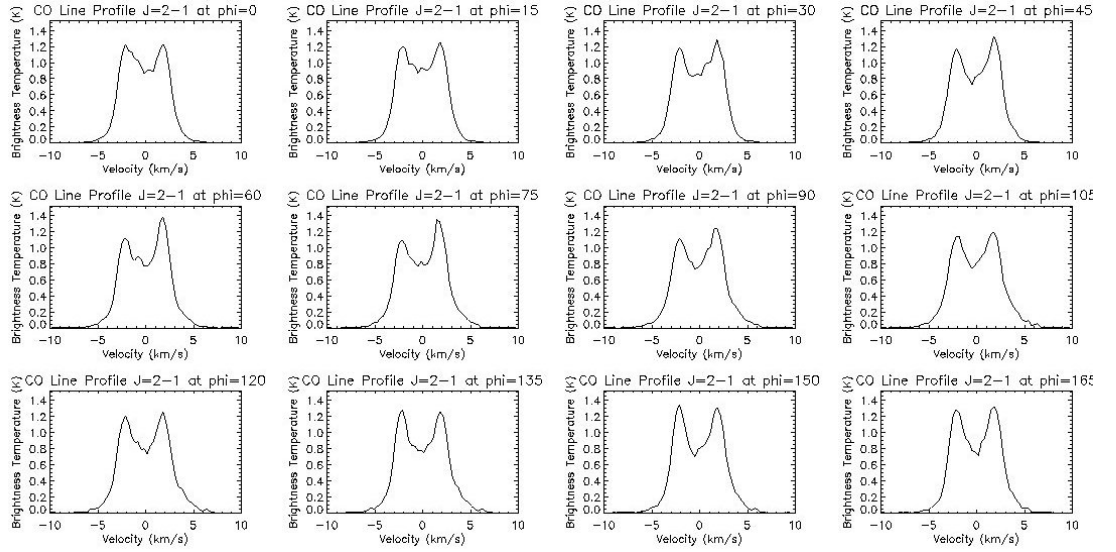
**Figure 5.9** Face on view showing midplane density of the spiral disk model, images are 4, 20 and 50AU on a side from left to right.

As there are two spiral arms in the disk, each circling the centre  $\sim 1.5$  times the geometry is rather complex. The spiral arms have a virtually symmetric density distribution about any viewing angle so material approaching on one side of the disk is effectively balanced by material receding on the opposite side of the disk. The fact that we are able to resolve the extra emission peak implies that the spiral arms are not symmetrically clumpy and it is one or more of these clumps that we see orbiting in the disk.



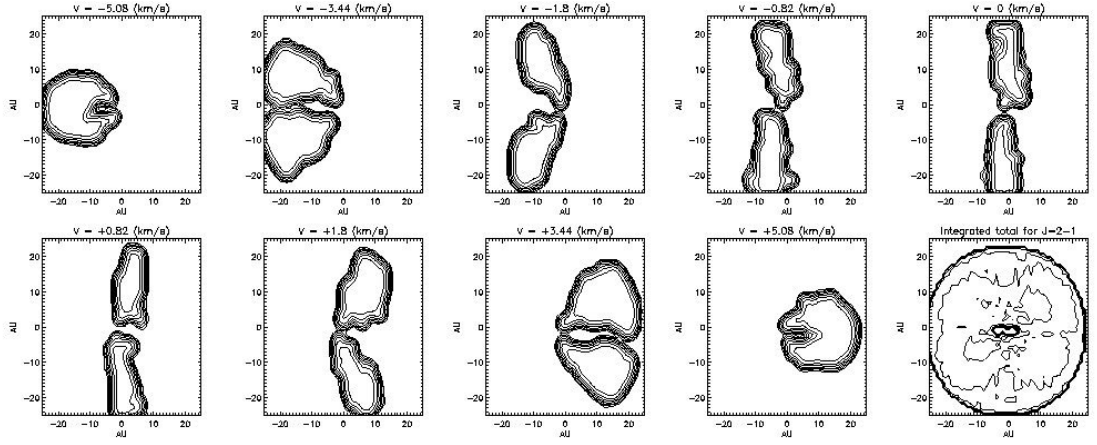
**Figure 5.10** Line profiles of the evolved, spiral dynamical disk, inclined at  $20^\circ$  and viewed at an azimuth of  $60^\circ$ , for transitions between the first six rotational energy levels of the CO molecule.

Figure 5.11 shows the line profile of the J=2-1 transition viewed at an inclination of  $20^\circ$  like figure 5.10 but at a number of steps between  $0^\circ$  and  $180^\circ$  in azimuth. It is possible to see the component producing the extra emission move across the line profile as the simulation rotates. In fact it appears that there are two “clumps” of material both producing excess emission. Possibly they are slightly asymmetric clumps located at similar positions in the two spiral arms.



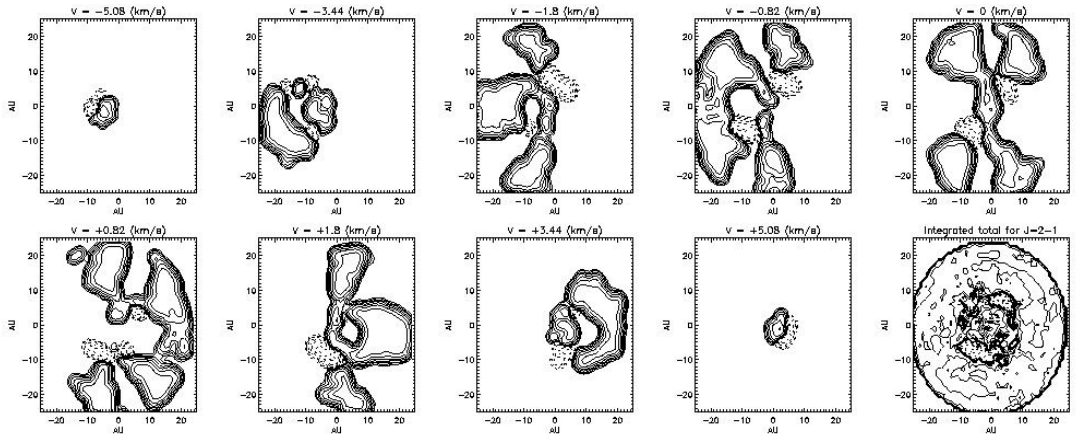
**Figure 5.11** Line profiles of the spiral disk viewed at an inclination of  $20^\circ$  and azimuth intervals of  $15^\circ$  round  $180^\circ$  of the disk. The extra peak in the emission caused by the spiral arms can be seen to move with viewing angle.

Figure 5.12 shows the contour maps of the J=2-1 transition in the spiral disk and the total integrated emission from the disk over the whole velocity bandwidth. While they are obviously different to those of the smooth disk the spiral density structure is not apparent.



**Figure 5.12** Contour maps of the J=2-1 CO emission for the spiral disk model across a range of velocities and at an inclination of  $40^\circ$ . Images are 100AU on a side and the lower right panel shows the total integrated emission over the Doppler line-width.

Figure 5.13 shows the difference in the contour maps of the smooth and spiral disks. The solid contour lines show the regions with a positive value after the spiral disks emission has been subtracted off of the smooth disks and the dashed contours show regions with a negative value after the subtraction. The integrated difference emission plot shows what appear to be two partly formed spiral arms in the outer parts of the disk. They are asymmetric and could well be responsible for the interesting excess emission near line centre in the spiral disks line profile.



**Figure 5.13** Contour maps of the J=2-1 CO emission for the difference in the smooth and spiral disks. The solid contours mark positive regions after subtraction and the dotted contours mark regions with negative values. The images are for a range of velocities and with the disk inclined at  $40^\circ$ . Images are 100AU on a side and the lower right panel shows the total integrated emission of the subtracted disk over the Doppler line-width.



Figure 5.14 shows the line profiles for the J=2-1 of both the smooth and spiral disks at several inclinations and, for the spiral disk, several azimuth angles. The obvious reduction in brightness temperature of the spiral disk's line profile is most likely due to optical depth effects from the fragmented, spiral, surface of the disk.

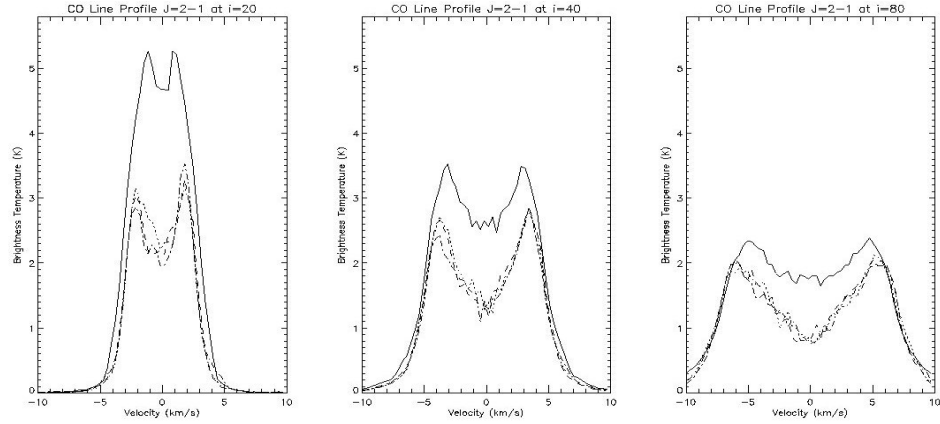


**Figure 5.14** Comparison of smooth disk line profile (solid line) with the spiral disk line profiles for an azimuth angle of  $0^\circ$  (dotted line),  $30^\circ$  (dot-dashed line) and  $60^\circ$  (dashed line). Shown for inclinations of  $20^\circ$ ,  $40^\circ$  and  $80^\circ$ .

#### 5.4 Conclusion and Future Applications of the Code

The 3D molecular line transition code has been applied to predict CO line profiles in the complex 3D density and velocity structure of a self gravitating, massive circumstellar disk. The multiple peaked signal of a non-smoothly varying density was observed but the SPH model investigated lacks the resolution to yield more evident results. A more detailed density and velocity grid would almost certainly improve the signature of the spiral arms, particularly if they were resolved to be more clumpy and asymmetric.

The investigations in this chapter have shown that my 3D molecular line transition code is able to calculate line profiles for a number of transitions between the rotational energy levels of the CO molecule. It does this in a fully 3D manner for the complex density and velocity structures and geometries found in the circumstellar environment of YSOs. The results detailed here compare well with the general predictions of the model described by Hogerheijde et al. (2000) with which we hope to run comparisons in the near future.

The success at resolving a feature attributed to the structure within the disk itself is of particular importance. With the much awaited Atacama Large Millimetre Array (ALMA) being constructed in Chile a whole range of opportunities is opening up.

Through observation in the millimetre part of the spectrum and its ability to detect spectral line emission from CO or CII, ALMA will reveal the dynamics and velocity structure of the dust-obscured protostellar accretion disks, the rate of accretion and infall from the molecular clouds and the mass distribution over the disk. Indirect evidence for planet formation may be provided by the presence of gaps cleared by large bodies condensing around the stars. Dynamical models of disks have been predicting interesting structures at a range of scales, varying over the evolutionary time of the disk. These predictions can be simulated using this code to produce line profiles and contour maps of the velocity of the emitting material. When ALMA comes online in 2012, the presence of these predicted observational signatures would be a significant verification of current dynamical theory.

A further application is the inclusion of other structures commonly found in the circumstellar environment, for example, jets and outflows. Pety et al. (2006) have observed the disk and jets of the HH30 system and this is a possible 2D test case. We can also return to the original application of this code, the molecular clouds and collapsing cores of star formation regions but undertake a much more thorough treatment than the traditional 1D ‘spherical’ treatment.

## **6. Future Investigations**

The research undertaken throughout this thesis has investigated several of the observational signatures of various aspects of the evolutionary processes present in the Young Stellar Objects known as T Tauri stars and their accompanying protoplanetary circumstellar disks. Rather than confining my investigation to an individual aspect of these processes I have used the versatility of the Monte Carlo technique, with several modifications and extensions described in the relevant chapters throughout this thesis to undertake a study of the disk structure and constitution of both the disk at large and the changeable and dynamic inner disk regions.

The variety of the environments and processes investigated here give an indication of the breadth and scope of investigations into YSOs that the codes developed here can be applied to in the future. I will briefly describe here some of the more immediate and interesting areas of investigation.

As more of the SPITZER data becomes publicly available it can be investigated in much the same way as described in chapter 3. The disk structure and the extent of dust settling and grain growth can be investigated for a larger number of CTTs possibly providing markers for the disks age and more information on the evolutionary processes disks mature through. Specific regions of the disk can be investigated in much greater detail, for example the rapidly settling, warm inner regions of the disk or the far cooler more flared outer regions. Changes in the dust constituents and chemical composition of the grains throughout the disk can be investigated and compared with observation as and when data of sufficient detail becomes available.

High resolution near – IR interferometry should shed more light on the nature of the structures that are predicted to form in the inner regions of the disk. The existence of inner holes or annuli virtually cleared of material by the formation of planets or by some other mechanism can be verified. The prediction of shadowed inner walls discussed in chapter 3 may be tested by higher resolution imaging and the effect this has on the disks structure can be investigated further.

The construction of ALMA (Atacama Large Millimetre Array) in Chile with it's planned resolution of 0.01" operating in the millimetre range of the spectrum from 350 $\mu$ m – 10mm promises to be a powerful tool and will open a new window of investigation on to the early stages and inner structure of young disks that have until now been mostly shrouded in the opaque envelopes of their parent stars. At the distance

of the Taurus star forming region,  $\sim 140\text{pc}$ , ALMA's resolution will allow structures down to  $1.4\text{AU}$  in size to be resolved and should easily detect the presence of compact self gravitating disks like those discussed in chapter 5 and inner disk gaps like those discussed in chapter 3.

The development of my 3D Non-LTE code makes it possible to investigate the velocity structures of disks generated by dynamical models where previously only the effects of their density distributions on the SED could be investigated. Structures such as jets and outflows can be incorporated and studied and the molecular clouds and collapsing cores of the early stages of star formation can be investigated in a dynamical sense for comparison with SPH collapse models. The combined investigation of the disk velocity and density structure will further constrain estimates of the disk properties and allow us to make predictions that can be verified with observations at high resolution.

## Bibliography

- Adams, F.C., Lada, C.J. & Shu, F.H., 1987, ApJ, 312, 788
- Adams, F.C., Emerson, J.P. & Fuller, G.A. 1990, ApJ, 357, 606
- Allers, K.N., Kessler-Silacci, J.E., Cieza, L.A. & Jaffe, D.T., 2006, ApJ, 556, 357
- Andre, P., Deeney, B.D., Phillips, R.B. & Lestrade, J.-F., 1992, ApJ, 401, 667
- Appenzeller, I. & Mundt, R., 1989, A&A Rev., 1, 291
- Bar-Nun, A., Kleinfeld, I. & Kochavi, E., 1988, Phys. Rev. B, 38, 7749
- Bash, F.M. & Peters, W.L., 1976, ApJ, 205, 786
- Bastian, U., Finkenzeller, U., Jaschek, C., & Jaschek, M., 1983, A&A, 126, 438
- Beckwith, S.V.W., Sargent, A.I., Chini, R.S. & Gueston, R., 1990, AJ, 99, 924
- Beckwith, S.V.W. & Sargent, A.I. 1991, 381, 250
- Bernes, C., 1979, A&A, 73, 67
- Bertout, C., 1989, AR A&A, 27, 351 Bertout, C., 1989, ARA&A, 27, 351
- Bjorkman, J.E. & Wood, K., 2001, ApJ, 554, 615
- Bjorkman, J.E., Whitney, B.A. & Wood, K., 2003, BAAS, 203, 4910
- Boekel, R. van, Waters, L.B.F.M., Dominik, C., Bouwman, J., de Koeter, A., Dullemond, C.P. & Paresce, F. 2003, A&A, 400, L21
- Bohren, C.F. & Huffman, D.R. 1983, *Absorption and Scattering of Light by Small Particles* (New York: Wiley)
- Bouvier, J., Cabrit, S., Fernández, M., Martin, E.L. & Matthews, J.M., 1993, A&A, 61, 737
- Bouvier, J., Chelli, A., Allain, S., Carrasco, L., Costero, R., Cruz-Gonzalez, I., Dougados, C., Fernández, M., Martín, E.L., Ménard, F., Mennessier, C., Mujica, R., Recillas, E., Salas, L., Schmidt, G. & Wichmann, R., 1999, A&A, 349, 619
- Bouvier, J., Grankin, K.N., Alencar, S.H.P., Dougados, C., Fernández, M., Basri, G., Batalha, C., Guenther, E., Ibrahimov, M.A., Magakian, T.Y. & 4 co-authors, 2003, A&A, 409, 169
- Bouvier, J., Alencar, S.H.P., /Harries, T.J., Johns-Krull, C.M. & Romanova, M.M., 2007, *Protostars and Planets V*, ed. B. Reipurth, D. Jewitt & K. Keil (Tucson: Univ. Arizona Press), 479
- Bouwman, J., Meeus, G., de Koter, A., Hony, S., Dominik, C. & Waters, L.B.F.M., 2001, A&A, 375, 950
- Bouwman, J., de Koter, A., Dominik, C. & Waters, L.B.F.M., 2003, A&A, 401, 577

- Brandner, W., Zinnecker, H., Alcalá, J.M., Allard, F., Covino, E., Frink, S., Köhler, R., Kunkel, M., Moneti, A. & Schweitzer, A., 2000, *AJ*, 120, 950
- Burrows, C. J., Stapelfeldt, K.R., Watson, A.M., Krist, J.E., Ballester, G.E., Clarke, J.T., Crisp, D., Gallagher, J.S., Griffiths, R.E., Hester, J.J. & 6 co-authors, 1996, *ApJ*, 473, 437
- Burton, M., 2005, *PASA*, 22, 199
- Calvet, N., D'Alessio, P., Hartmann, L., Wilner, D., Walsh, A. & Sitko, M., 2002, *ApJ*, 568, 1008
- Calvet, N., D'Alessio, P., Watson, D.M., Franco-Hernández, R., Furlan, E., Green, J., Sutter, P.M., Forrest, W.J., Hartmann, L., Uchida, K.I., Keller, L.D., Sargent, B., Najita, J., Herter, T.L., Barry, D.J. & Hall, P., 2005, *ApJ*, 630, L185
- Chiang, E.I. & Goldreich, P. 1997, *ApJ*, 490, 368
- Chiang, E.I. & Goldreich, P. 1999, *ApJ*, 519, 279
- Chiang, E.I., Joun, M.K., Creech-Eakman, M.J., Qi, C., Kessler, J.E., Blake, G.A. & van Dishoeck, E.F., 2001, *ApJ*, 547, 1077
- Chiang, E.I. & Murray-Clay, R. 2007, *Nature Physics*, 3, 604
- Choi, P.I. & Herbst, W., 1996, *AJ*, 111, 283
- Code, A.D. & Whitney, B.A., 1995, *ApJ*, 441, 400
- Cotera, A.S., Whitney, B.A., Young, E., Wolff, M.J., Wood, K., Povich, M., Schneider, G., Rieke, M. & Thompson, R., 2001, *ApJ*, 556, 958
- Crosas, M. & Menten, K.M., 1997, *ApJ*, 483, 913
- D'Alessio, P., Cantó, J., Calvet, N. & Lizano, S. 1998, *ApJ*, 500, 411
- D'Alessio, P., Calvet, N., Hartmann, L., Lizano, S. & Cantó, J. 1999a, *ApJ*, 527, 893
- D'Alessio, P., Cantó, J., Hartmann, L., Calvet, N. & Lizano, S. 1999b, *ApJ*, 511, 896
- D'Alessio, P., Calvet, N. & Hartmann, L. 2001, *ApJ*, 553, 321
- D'Alessio, P., Calvet, N. & Hartmann, L., Muzerolle, J. & Sitko, M. 2003, *Star Formation at High Angular Resolution*, ASP Conference Series, Vol. S-221
- D'Alessio, P., Hartmann, L., Calvet, N., Franco-Hernández, R., Forrest, W.J., Sargent, B., Furlan, E., Uchida, K.I., Green, J.D., Watson, D.M., Chen, C.H., Kemper, F., Sloan, G.C. & Najita, J., 2005, *ApJ*, 621, 461
- D'Alessio, P., Calvet, N., Hartmann, L., Franco-Hernández, R. & Servín, H. 2006, *ApJ*, 638, 314
- Draine, B.T. & Lee, H.M. 1984, *ApJ*, 285, 89
- Duchêne, G., Ménard, F., Stapelfeldt, K. & Duvert, G., 2003, *A&A*, 400, 559

- Dullemond, C.P., van Zadelhoff, G. J. & Natta, A. 2002, A&A, 389, 464
- Dullemond, C.P. & Natta, A. 2003a, A&A, 408
- Dullemond, C.P. & Dominik, C. 2004a, A&A, 417, 159
- Dullemond, C.P. & Dominik, C. 2004b, A&A, 421, 1075
- Dullemond, C.P. & Dominik, C. 2005, A&A, 434, 971
- Dullemond, C.P., Hollenback, D., Kamp, I. & D'Alessio, P., 2007, *Protostars and Planets V*, ed. B. Reipurth, D. Jewitt & K. Keil (Tucson: Univ. Arizona Press), 555
- Eaton, N.L., Herbst, W. & Hillenbrand, L.A., 1995, AJ, 110, 1735
- Eisner, J., Hillenbrand, L., Carpenter, J. & Wolf, S., 2005, ApJ, 635, 396
- Fukagawa, M., Hayashi, M., Tomura M., Itoh, Y., Hayashi, S.S & Oasa, Y.e.a., 2004, ApJ, 605, L53
- Furlan, E., Calvet, N., D'Alessio, P., Hartmann, L., Forrest, W.J., Watson, D.M., Uchida, K.I., Sargent, B., Green, J.D. & Herter, T.L. 2005, ApJ, 628, L65
- Furlan, E., Hartmann, L., Calvet, N., D'Alessio, P., Franco-Hernández, R., Forrest, W.J., Watson, D.M., Uchida, K.I., Sargent, B., Green, J.D., Keller, L.D. & Herter, T.L. 2006, ApJ Supp., 165, 568
- Gammie, C.F., 2001, ApJ, 553, 174
- Greene, T., 2001, American Scientist, 89, 316
- Hartigan, P., Edwards, S. & Ghandour, L., 1995, RMxAC, 3, 93H
- Hartmann, L., Ballesteros-Paredes, J. & Bergin, E., 2001, ApJ, 562, 852
- Hartmann, L., 2003, ApJ, 585, 398
- Hatzes, A.P., 1995, ApJ, 451, 784
- Herbig, G.H., 1962, Adv. Astron. Astrophys., 1, 47
- Herbig, G.H., 1977, ApJ, 214, 747
- Herbst, W., Holtzman, J.A., & Klasky, R.S., 1983, AJ, 88, 1648
- Herbst, W., Herbst, D.K., Grossman, E.J. & Weinstein, D., 1994, AJ, 108, 1906
- Hogerheijde, M.R. & van der Tak, F.F.S., 2000, A&A, 362, 697
- Hughes, A.M., Wilner, D.J. & Hogerheijde, M.R., *accepted for publication in ApJ: January 29 2008*
- Isella, A. & Natta, A., 2005, A&A, 438, 899
- Isella, A., Testi, L. & Natta, A., 2006, A&A, 451, 951
- Jayawardhana, R., Hartmann, L., Fazio, G., Fisher, S.F., Telesco, C.M. & Piña R.K., 1999, ApJ, 521, L129

- Jayawardhana, R., Coffey, J., Scholz, A., Brandecker A. & van Kerkwijk, M.H., 2006, ApJ, 648, 1206
- Jones, B.F. & Herbig, G.H., 1979, AJ, 84, 1872
- Joy A.H., 1945, ApJ, 102, 168
- Juvela, M., 1997, A&A, 322, 943
- Kenyon, S.J. & Hartman, L., 1987, ApJ, 323, 714
- Kenyon, S.J., Hartmann, L., Hewett, R., Carrasco, L., Cruz-Gonzalez, I., Recillas, E., Salas, L., Serrano, A., Strom, K.M., Strom, S.E. & Newton, G., 1994, AJ, 107, 2153
- Kenyon, S.J. & Hartman, L., 1995, ApJ, 101, 117
- Kim, S.-H., Martin, P.G. & Hendry, P.D. 1994, ApJ, 422, 164K
- Koerner, D.W., Sargent, A.I. & Bechwith, S.V.W., 1993, Icarus, 106, 2
- Kurucz, R.L., 1994, CD-ROM 19, *Solar Model Abundance Model Atmospheres* (Cambridge: SAO)
- Lada, C.J. & Adams, F.C., 1992, ApJ, 393, 278
- Lada, C.J. & Kylafis, N.D. 1999, *The Origin of Stars and Planetary Systems* (Kluwer Academic Publishers)
- Lada, C.J., Lada, E.A., Muench, A.A., Haisch, K. & Alves, J., 2002, *The Origin of Stars and Planets*, ESO Astrophysics Symposia, ed. Alves, J. & McCaughrean, M.J. (Springer-Verlag), 155
- Laor, A. & Draine, B.T., 1993, ApJ, 402, 441L
- Larson, R.B., 2003, Reports on Progress in Physics, 66, 1651
- Leung, C.-M. & Liszt, H.S., 1976, ApJ, 208, 732
- Lin, D.N.C. & Pringle, J.E., 1990, ApJ, 358, 515
- Lissauer, J.J. 1993, ARA&A, 31, 129
- Livio, M., Pringle, J.E & Wood, K., 2005, ApJ, 632, L37
- Lodato, G. & Rice, W.K.M., 2005, MNRAS, 358, 1489
- Lucy, L.B., 1987, *ESO Workshop on SN*, ed. Danziger, I.J., 417
- Lucy, L.B., 1999a, A&A, 344, 282
- Lucy, L.B., 1999b, A&A, 345, 211
- Lucy, L.B., 2005, A&A, 429, 19
- Lutz, B.L., Womack, M. & Wagner, R.M., 1993, ApJ, 407, 402
- Lynden-Bell, D. & Pringle, J.E., 1974, MNRAS, 168, 603
- Mahdavi, A. & Kenyon, S.J., 1998, ApJ, 497, 342
- Manning, V. & Emerson, J.P. 1994, MNRAS, 267, 361



- Mannings, V. & Sargent, A.I., 1997, *ApJ*, 490, 792
- Mannings, V. & Sargent, A.I., 2000, *ApJ*, 529, 391
- Mathis, J.S., Rumpl, W. & Nordsieck, K.H. 1977, *ApJ*, 217, 425
- Marsh, K.A. & Mahoney, M.J., 1992, *A&A*, 395, L115
- Ménard, F., 1989, PhD thesis, Université de Montréal
- Ménard, F., Bouvier, J., Dougados, C., Mel'nikov, S.Y. & Grankin, K.N., 2003, *A&A*, 409, 163
- Mihalas, D., 1978, *Stellar Atmospheres* (San Francisco: Freeman)
- Miyake, K. & Nakagawa, Y. 1993, *Icarus*, 106, 20
- Miyake, T. & Nakagawa, Y. 1995, *ApJ*, 441, 361
- Monaghan, J.J., 1992, *ARA&A*, 30, 543
- Mundt, R., Brugel, E.W. & Bührke, T. 1987, *ApJ*, 319, 275
- Murray, J.R., 1996, *MNRAS*, 279, 402
- Murray, J.R., Chakrabarty, D., Wynn, G.A. & Kramer, L., 2002, *MNRAS*, 335, 247
- Myers, P.C., Fuller, G.A., Mathieu, R.D., Beichman, C.A., Benson, P.J., Schild, R.E. & Emerson, J.P., 1987, *ApJ*, 319, 340
- Nagasawa, M., Thommes, E.W., Kenyon, S.J., Bromely, B.C. & Lin, D.N.C., 2007, *Protostars and Planets V*, ed. B. Reipurth, D. Jewitt & K. Keil (Tucson: Univ. Arizona Press), 277
- Owen, T. & Bar-Nun, A., 1995, *Icarus*, 116, 215
- Palla, F. & Stahler, S., 2002, *ApJ*, 581, 1194
- Park, Y.-S. & Hong, S.S., 1995, *A&A*, 300, 890
- Pearson, K.J., Wynn, G.A. & King, A.R., 1997, *MNRAS*, 288, 421
- Petit, P. & Donati, J.-F., 2004, The ESPaDOnS project team, *EAS Publication Series*, 9, 97
- Pety, J., Gueth, F., Guilloteau, S. & Dutrey, A., 2006, accepted for publication in *A&A*
- Pfeiffer, H.P. & Lai, D., 2004, *ApJ*, 604, 766
- Pinte, C., Ménard, F., Duchêne, G. & Bastien, P., 2006, *A&A*, 459, 797
- Pollack, J.B., Hollenbach, D., Beckwith, S., Simonelli, D.P., Roush, T. & Fong, W. 1994, *ApJ*, 421, 615
- Pollack, J.B., Hollenbach, D., Beckwith, S., Simonelli, D.P., Roush, T. & Burrows, C.J. 1998, *ApJ*, 502, L65
- Pudritz, R.E., Ouyed, R., Fendt, C. & Brandenburg, A., 2007, *Protostars and Planets V*, ed. B. Reipurth, D. Jewitt & K. Keil (Tucson: Univ. Arizona Press), 277

- Qi, C., Kessler, J.E., Koerner, D.W., Sargent, A.I. & Blake, G.A., 2003, ApJ, 597, 986
- Qi, C., Wilner, D.J., Calvet, N., Bourke, T.L., Blake, G.A., Hogerheijde, M.R., Ho, P.T.P. & Bergin, E., 2006, ApJ, 636, L157
- Quillen, A.C., Blackman, E.G., Frank, A. & Varnière P., 2004, ApJ, 612, L137
- Raman, A., Lisanti, M., Wilner, D.J., Qi, C. & Hogerheijde, M., 2006, ApJ, 131, 2290
- Rice, W.K.M., Armitage, P.J., Bate, M.R. & Bonnell, I.A., 2003a, MNRAS, 339, 1025
- Rice, W.K.M., Wood, K., Armitage, P.J., Whitney, B.A. & Bjorkman, J.E., 2003b, MNRAS, 342, 79
- Rice, W.K.M., Lodato, G., Pringle, L.E., Armitage, P.J. & Bonnell, I.A., 2004, MNRAS, 351, 630
- Rice, W.K.M., Lodato, G. & Armitage, P.J., 2005, MNRAS, 364, L56
- Rice, W.K.M., Lodato, G., Pringle, J.E., Armitage, P.J. & Bonnell, I.A., 2006, MNRAS, 372, L9
- Rice, W.K.M., Armitage, P.J., Wood, K. & Lodato, G., 2006, in press
- Robitaille, T.P., Whitney, B.A., Indebetouw, R. & Wood, K., 2007, ApJS, 169, 328
- Rodríguez, L.F., Loinard, L., D'Alessio, P., Wilner, D.J. & Ho, P.T.P., 2005, ApJ, 621, L133
- Romanova, M.M., Ustyugova, G.V., Koldoba, A.V. & Lovelace, R.V.E., 2002, ApJ, 578, 420
- Romanova, M.M., Ustyugova, G.V., Koldoba, A.V., Wick, J.V. & Lovelace, R.V.E., 2003, ApJ, 595, 1009
- Ruden, S.P. & Lin, D.N.C., 1986, ApJ, 308, 883
- Scholz, A., Jayawardhana, R. & Wood, K., 2006, ApJ, 645, 1498
- Schneider, G., Wood, K., Silverstone, M., Hines, D.C., Korner, D.W., Whitney, B., Bjorkman, J.E. & Lowrance, P.J., 2003, AJ, 125, 1467
- Schneider, G., Silverstone, M.D., Hines, M.D., Cotera, A.S., Grady, C.A., Stapelfeldt, K.R., Padgett, D.L., Menard, F., Wolf, S. & Stecklum, B., 2007, *Protostars and Planets V*, ed. B. Reipurth, D. Jewitt & K. Keil (Tucson: Univ. Arizona Press), 277
- Shakura, N. I. & Sunyaev, R. A., 1973, A&A, 24, 337
- Shu, F.H., 1977, ApJ, 214, 488
- Shu, F.H., Adams, F.C. & Lizano, S., 1987, Ann. Rev. A&A, 25, 23
- Simon, M., Dutrey, A. & Guilloteau, S., 2001, ApJ, 545, 1034
- Sitko, M.L., Lynch, D.K. & Russell, R.W., 2000, ApJ, 120, 2609

- Stahler, S.W. & Palla, F., 2005, *The Formation of Stars* (Wiley-vch)
- Stapelfeldt, K.R., Watson, A.M., Krist, J.E. & Burrows, C.J., 1999, AAS, 195.020
- Stassun, K. & Wood, K., 1999, ApJ, 510, 892
- Strom, K.M., Strom, S.E., Edwards, S., Cabrit, S. & Skrutskie, M.F., 1989, AJ, 97, 1451
- Tanaka, H., Himeno, Y. & Ida, S. 2005, ApJ, 625, 414
- Terebey, S., Shu, F.H. & Cassen, P., 1984, ApJ, 286, 529
- Terquem, C. & Papaloizou, J.C.B., 2000, A&A, 360, 1031
- Truss, M.R., Murray, J.R., Wynn, G.A. & Edgar, R.G., 2000, MNRAS, 319, 467
- Truss, M.R. & Wynn, G.A., 2004, MNRAS, 353, 1048
- Van de Hulst, H.C., 1981, *Light Scattering by Small Particles* (New York: Dover)
- Vogel, S.S. & Kuhi, L.V., 1981 ApJ, 245, 960
- Vrba, F.J., Chugainov, P.F., Weaver, W. B. & Stauffer, J.S., 1993, AJ, 106, 1608
- Vrba, F.J., Rydgren, A.E., Chugainov, P.F., Shakovskaya, N.I. & Weaver, W.B., 1989, AJ, 97, 483
- Walker, C., Wood, K., Lada, C.J., Robitaille, T., Bjorkman, J.E. & Whitney, B.A., 2004, MNRAS, 351, 607
- Ward-Thompson, D., André, P., Crutcher, R., Johnstone, D., Onishi, T. & Wilson, C., 2007, *Protostars and Planets V*, ed. B. Reipurth, D. Jewitt & K. Keil (Tucson: Univ. Arizona Press), 33
- Webb, R.A., Zuckerman, B., Platais, I., Patience, J., White, R.J., Schwartz, M. J. & McCarthy, C., 1999, ApJ, 512, L63
- Weinberger, A., 2006, Carnegie Institute of Washington Department of Terrestrial Magnetism, <http://www.dtm.ciw.edu/alycia/picts/twhy.html>
- White, R.J., Greene, T.P., Doppmann, G.W., Covey, K.R. & Hillenbrand, L.A., 2007, *Protostars and Planets V*, ed. B. Reipurth, D. Jewitt & K. Keil (Tucson: Univ. Arizona Press), 277
- Whitney, B.A. & Hartmann, L., 1992, ApJ, 395, 529
- Whitney, B.A. & Hartmann, L., 1993, ApJ, 402, 605
- Whitney, B.A. & Wolff, M.J., 2002, ApJ, 574, 205
- Wilner, D.J., Ho, P.T.P., Kastner, J.H. & Rodríguez, L.F., 2000, ApJ, 534, L101
- Wiscombe, W.J. 1979, *Mie Scattering Calculations: Advances in Technique and Fast, Vector-Speed Computer Codes* (NCAR/TN-140 + STR; Boulder, National Centre for Atmospheric Research)
- Wolf, S., Henning, T. & Stecklum, B., 1999, A&A, 349, 839

- Wood, K., Bjorkman, J.E., Whitney, B.A. & Code, A.D., 1996, ApJ, 461, 828
- Wood, K. & Whitney, B.A., 1998, ApJ, 506, L43
- Wood, K., Stanek, K.Z., Wolk, S., Whitney, B. & Stassun, K., 2000, AAS, 32, 1414
- Wood, K., Wolff, M.J., Bjorkman, J.E. & Whitney, B. 2002a, ApJ, 564, 887
- Wood, K., Lada, C.J., Bjorkman, J.E., Kenyon, S.J., Whitney, B.A. & Wolff, M.J., 2002b, ApJ, 567, 1183
- Wuchterl, G., Guillot, T. & Lissauer, J.J., 2000, *Protostars and Planets IV*, ed. V. Mannings, A.P. Boss & S.S. Russell (Tucson: Univ. Arizona Press), 1081
- Wyckoff, S. & Theobald, J., 1989, Adv. Space Res., 9, 157
- Wynn, G.A., King, A.R. & Horne, K.D., 1997, MNRAS, 286, 436
- Zelik, M., Gregory, S.A. & Smith, E.v.P., 1992, *Introductory Astronomy & Astrophysics*, third edition (Saunders College Publishing)